# EFFECT OF PRESCRIBED BOUNDARY CONDITIONS ON THE CONDENSER BEHAVIOR OF GROOVED HEAT PIPES

A THESIS SUBMITTED TO
THE GRADUATE SCHOOL OF NATURAL AND APPLIED SCIENCES
OF
MIDDLE EAST TECHNICAL UNIVERSITY

BY

ALI POURABDOLLAH VARDIN

IN PARTIAL FULFILLMENT OF THE REQUIREMENTS
FOR
THE DEGREE OF MASTER OF SCIENCE
IN
MECHANICAL ENGINEERING

FEBRUARY 2022

Approval of the thesis:

**EFFECT OF PRESCRIBED BOUNDARY CONDITIONS ON THE CONDENSER BEHAVIOR OF GROOVED HEAT PIPES**

submitted by **ALI POURABDOLLAH VARDIN** in partial fulfillment of the requirements for the degree of **Master of Science in Mechanical Engineering Department, Middle East Technical University** by,

Prof. Dr. Halil Kalıpçılar
Dean, Graduate School of **Natural and Applied Sciences** _____

Prof. Dr. M. A. Sahir Arıkan
Head of Department, **Mechanical Engineering** _____

Prof. Dr. Zafer Dursunkaya
Supervisor, **Mechanical Engineering, METU** _____

**Examining Committee Members:**

Assoc. Prof. Dr. Özgür Bayer
Mechanical Engineering, METU _____

Prof. Dr. Zafer Dursunkaya
Mechanical Engineering, METU _____

Assoc. Prof. Dr. Onur Taylan
Mechanical Engineering, METU _____

Assist. Prof. Dr. Altuğ Özçelikkale
Mechanical Engineering, METU _____

Assoc. Prof. Dr. Barbaros Çetin
Mechanical Engineering, Bilkent University _____

Date: 10.02.2022

**I hereby declare that all information in this document has been obtained and presented in accordance with academic rules and ethical conduct. I also declare that, as required by these rules and conduct, I have fully cited and referenced all material and results that are not original to this work.**

Name, Surname: Ali Pourabdollah Vardin

Signature :

# ABSTRACT

## EFFECT OF PRESCRIBED BOUNDARY CONDITIONS ON THE CONDENSER BEHAVIOR OF GROOVED HEAT PIPES

Vardin, Ali Pourabdollah
M.S., Department of Mechanical Engineering
Supervisor: Prof. Dr. Zafer Dursunkaya

FEBRUARY 2022, 83 pages

Rapid enhancements in electronic microchips bring the need to design and manufacture advanced cooling devices which can operate effectively without external source. Passive heat exchangers like heat pipes can remove a remarkable amount of heat with the help of capillary action. The phase change process in heat pipes, which utilizes the latent heat energy, enables high heat transfer rate over small temperature differences. Although the physics of evaporation in grooved heat pipes is understood, and comparatively satisfactory models are present, the condensation, on the other hand, is more complex and still requires a better physical understanding to facilitate the development of realistic models. This study investigates the effect of two different sets of boundary conditions on forming liquid-vapor interface film on the fin top of grooved heat pipes. The validation results reveal that the boundary conditions at the fin edge can change depending on the edge angle and the temperature difference between the vapor and liquid. Also, the impact of disjoining pressure on the solution domain and film profile is explored, which shows that inclusion of the effect of disjoining pressure can limit the solution domain, and beyond a specific edge angle, a solution cannot be obtained. Moreover, the current study presents a novel numerical

approach based on a modified finite difference method to solve the governing non-linear fourth-order differential equation. This novel approach provides a chance to model the two-dimensional flow on the fin top, which has not been studied in the literature yet. The primary findings of the two-dimensional model suggest that the axial flow is negligible compared to the lateral flow on the fin top except for a small region near the centerline.

Keywords: Condensation, disjoining pressure, numerical simulation, Grooved heat pipes, two-dimensional flow

# ÖZ

## ÖNGÖRÜLEN SINIR ŞARTLARININ OLUKLU ISI BORULARININ YOĞUŞTURMA DAVRANIŞINA ETKİSİ

Vardin, Ali Pourabdollah
Yüksek Lisans, Makina Mühendisliği Bölümü
Tez Yöneticisi: Prof. Dr. Zafer Dursunkaya

Şubat 2022 , 83 sayfa

Elektronik mikroçiplerdeki hızlı gelişmeler, dış etmenler olmadan etkin bir şekilde çalışabilen gelişmiş soğutma cihazları tasarlama ve üretme ihtiyacını beraberinde getirmektedır. Isı boruları gibi pasif ısı eşanjörleri, kılcal kuvvet yardımıyla kayda değer miktarda ısıyı taşıyabilır. Gizli ısı enerjisini kullanan ısı borularında faz değişimi işlemi, küçük sıcaklık farkları ile yüksek ısı akıları sağlar. Oluklu ısı borularında buharlaşmanın fiziği anlaşılmış ve görece yeterli modeller var olsa da, yoğuşma işlemi daha karmaşıktır ve gerçekçi modellerin geliştirilmesi için hala daha iyi bir fiziksel anlayış gerektirir. Bu çalışma, oluklu ısı borularının kanatçıklarının üst kısmında sıvı-buhar arayüz filminin oluşturulmasında iki farklı sınır koşulunun etkisini araştırmaktadır. Doğrulama sonuçları, kanatçığın oluk tarafındaki sınır koşullarının temas açısına ve buhar ile sıvı arasındaki sıcaklık farkına bağlı olarak değişebileceğini göstermektedır. Ayrıca, ayırma basıncının çözüm alanı ve film profili üzerindeki etkisi de çalışılmış ve ayırma basıncının eklenmesinin çözüm alanını sınırlayabileceğini ve belirli temas açısının ötesinde bir çözümün elde edilemeyeceğini gösterimiştır. Ayrıca, mevcut çalışma, doğrusal olmayan dördüncü dereceden diferansiyel denklemin çözömü için

sonlu farklar yönteminı termal alan yeni bir sayısal yaklaşım sunmaktadır. Bu yeni yaklaşım, henüz literatürde çalışılmamış olan kanatçık tepesindeki iki boyutlu akışı modelleme amaçlıdır. İki boyutlu modelin ılk sonuçları, eksenel akışın, merkez çizgisine yakın küçük bir bölge dışında, kanatçık tepesindeki yanal akışa kıyasla ihmal edilebilir olduğunu göstermektedir.

Anahtar Kelimeler: Yoğuşma, ayırma basıncı, sayısal simülasyon, Yivli ısı boruları, iki boyutlu akış

*To my family and loved ones,*

## ACKNOWLEDGMENTS

First and foremost, I would like to express my deepest gratitude to my supervisor, Dr. Zafer Dursunkaya for his never-ending support and guidance. I benefit from his precious ideas which help me a lot during this long journey, and I am so lucky that I have the honor of being his student.

Special thanks to Dr. Osman Akdağ, who generously provided me required data to validate my results.

Finally, I would like to express my deepest appreciation to my parents and my beloved sister for their endless support and inspiration. Making them happy and proud is one of my goals, which I hope to accomplish one day.

## TABLE OF CONTENTS

ABSTRACT . . . . . v

ÖZ . . . . . vii

ACKNOWLEDGMENTS . . . . . x

TABLE OF CONTENTS . . . . . xi

LIST OF TABLES . . . . . xiv

LIST OF FIGURES . . . . . xv

LIST OF ABBREVIATIONS . . . . . xix

CHAPTERS

1 INTRODUCTION . . . . . 1

1.1 Heat Pipes . . . . . 1

1.1.1 Types of heat pipes . . . . . 2

1.2 Dimensions of grooved heat pipes . . . . . 5

1.3 Literature Review . . . . . 5

1.4 Description and Motivation of the Current Study . . . . . 13

2 MODELING AND SOLUTION METHODOLOGY . . . . . 15

2.1 Phase change . . . . . 15

2.2 Capillary pressure . . . . . 16

2.3 Disjoining pressure . . . . . 17

2.4 Lubrication assumption . . . . . 17
2.5 One dimensional model . . . . . 17
2.5.1 Solution domain . . . . . 17
2.5.2 Unidirectional flow . . . . . 18
2.5.3 Groove side boundary conditions . . . . . 20
2.5.4 Numerical approach . . . . . 22
2.5.5 Fourth-Order Runge-Kutta (RK4) Method . . . . . 22
3 SIMULATION RESULTS OF ONE-DIMENSIONAL MODEL . . . . . 25
3.1 Fourth-order Runge-Kutta (RK4) solver . . . . . 26
3.2 Comparison of predictions of different groove side boundary conditions with the exact formulation . . . . . 28
3.3 The effect of disjoining pressure on the predictions of groove side boundary conditions . . . . . 34
4 TWO DIMENSIONAL FLOW ON THE FIN TOP . . . . . 45
4.1 Governing equations for two-dimensional flow modeling . . . . . 45
4.2 Finite difference (FD) method for one-dimensional model . . . . . 48
4.3 Validation of one-dimensional FD formulation with RK4 method . . 54
4.3.1 Mesh sensitivity of one-dimensional FD formulation . . . . . 56
4.4 FD formulation of the two-dimensional flow/condensation problem . 57
4.4.1 Solution domain . . . . . 58
4.4.2 Boundary conditions . . . . . 59
4.4.3 Numerical formulation and solution . . . . . 59
4.5 Preliminary findings . . . . . 63
4.5.1 The comparison of axial and lateral flows . . . . . 64

4.5.2 The effect of mesh size . . . . . 65

5 CONCLUSION AND SUGGESTIONS FOR FUTURE WORK . . . . . 69

5.1 Conclusion . . . . . 69

5.2 Possible future work . . . . . 70

REFERENCES . . . . . 71

APPENDICES

A MODIFIED FINITE DIFFERENCE FORMULAE . . . . . 77

A.1 Modified finite difference formulae for the fourth derivative . . . . . 77

A.2 Modified finite difference formulae for the third derivative . . . . . 81

# LIST OF TABLES

TABLES

Table 3.1 Thermophysical properties and geometrical parameters used in the condensation modeling . . . . . 26

## LIST OF FIGURES

FIGURES


Figure 1.1 Heat pipes scheme and working cycle [1] . . . . . 2

Figure 1.2 Different wick structures [2] . . . . . 2

Figure 1.3 Capillary pumped loop heat pipes [3] . . . . . 3

Figure 1.4 Principal scheme of loop heat pipes [4] . . . . . 4

Figure 1.5 Various cross-sections of micro heat pipes [5] . . . . . 4

Figure 1.6 Geometry of grooved heat pipe [7] . . . . . 5

Figure 1.7 Boundary conditions used in [34] . . . . . 10

Figure 1.8 Comparison between numerical and experimental liquid-vapor interface shape [35] . . . . . 11

Figure 1.9 Boundary conditions used in [37] . . . . . 12

Figure 1.10 Solution domain at [38] . . . . . 12

Figure 2.1 Phase change regions in the grooved heat pipe . . . . . 15

Figure 2.2 One dimensional solution domain . . . . . 18

Figure 2.3 First set of boundary conditions . . . . . 21

Figure 2.4 Second set of boundary conditions . . . . . 21

Figure 2.5 Flowchart of Fourth-Order Runge-Kutta Method . . . . . 23

Figure 3.1 Comparison of Mass flow rate along $x$ direction for $5000$, $10000$ and $20000$ number of nodes with $\theta = 20°$, $\Delta T = -5℃$ . . . . . 27

Figure 3.2 Comparison of film profile variation of Akdağ [39] with the two current models for $\theta = 65°$ and $\Delta T = -1℃$ . . . . . 28

Figure 3.3 Comparison of film profile variation of Akdağ [39] with the two current models for $\theta = 75°$ and $\Delta T = -1℃$ . . . . . 29

Figure 3.4 Comparison of film profile variation of Akdağ [39] with the two current models for $\theta = 85°$ and $\Delta T = -1℃$ . . . . . 29

Figure 3.5 Comparison of film profile variation of Akdağ [39] with Model 3, for $\theta = 65°$ with $\Delta T = -1℃$ . . . . . 31

Figure 3.6 Comparison of film profile variation of Akdağ [39] with Model 3, for $\theta = 75°$ with $\Delta T = -1℃$ . . . . . 31

Figure 3.7 Comparison of film profile variation of Akdağ [39] with Model 3, for $\theta = 85°$ with $\Delta T = -1℃$ . . . . . 32

Figure 3.8 Difference of mass flow rate between (a) Akdağ [39] and the current models (b) Model 3 and the current models, for $\theta = 65°$ with $\Delta T = -0.1℃$, $\Delta T = -0.3℃$, $\Delta T = -1℃$ and $\Delta T = -5℃$ . . . . . 33

Figure 3.9 Difference of mass flow rate between (a) Akdağ [39] and the current models (b) Model 3 and the current models, for $\theta = 75°$ with $\Delta T = -0.1℃$, $\Delta T = -0.3℃$, $\Delta T = -1℃$ and $\Delta T = -5℃$ . . . . . 33

Figure 3.10 Difference of mass flow rate between (a) Akdağ [39] and the current models (b) Model 3 and the current models, for $\theta = 85°$ with $\Delta T = -0.1℃$, $\Delta T = -0.3℃$, $\Delta T = -1℃$ and $\Delta T = -5℃$ . . . . . 34

Figure 3.11 Film profiles for $\theta = 88°$ with $\Delta T = -1℃$ and $\Delta T = -0.1℃$, without disjoining pressure for Model 1 and Model 2 . . . . . 35

Figure 3.12 Mass flow rate exiting the fin top for various temperature differences for Model 1 and Model 2 without disjoining pressure . . . . . 35

Figure 3.13 Variation of Model 1 film profiles for $\Delta T = -1$℃ for $\theta = 80°$ , $\theta = 70°$, $\theta = 60°$, $\theta = 50°$ and $\theta = 40°$ edge angles, including the effect of disjoining pressure . . . . . 36

Figure 3.14 Comparison of film profiles of Model 1 and Model 2 for $\Delta T = -1$℃ for $\theta = 80°$ and $\theta = 40°$ edge angles, including the effect of disjoining pressure . . . . . 37

Figure 3.15 Variation of mass flow rate along $x$ direction with $\Delta T = -1$℃ and $\Delta T = -0.1$℃ and with $\theta = 70°$ edge angle for Model 1 and Model 2 38

Figure 3.16 Percentage mass flow rate difference between Model 1 and Model 2 for various edge angles $\theta$ and temperature differences $\Delta T$ . . . . . 38

Figure 3.17 Relative change of mass exiting the fin top and range of edge angle till the cut off point for different models with $\Delta T = -0.1$℃ and $\Delta T = -1$℃ and for different edge angles . . . . . 39

Figure 3.18 Contribution of capillary and disjoining pressure terms to the mass flow rate for Model 2, with $\Delta T = -1$℃, for $\theta = 70°$, $\theta = 45°$, $\theta = 34°$ (Cut-off point), and $\theta = 33°$ . . . . . 41

Figure 3.19 The third derivative of film thickness with respect to $x$ along the lateral direction for Model 2, with $\Delta T = -1$℃, for $\theta = 34°$ (Cut-off point) and $\theta = 33°$ . . . . . 42

Figure 3.20 Comparison of second derivative of film thickness with respect to $x$ along lateral direction at the edge angles of $\theta = 85°$ and $\theta = 65°$ with temperature difference $\Delta T = -0.1$℃ . . . . . 43

Figure 4.1 Nodes in the finite difference method . . . . . 49

Figure 4.2 Ghost-cells . . . . . 50

Figure 4.3 Flowchart of FD method . . . . . 53

Figure 4.4 Mass flow rate comparison between RK4 and FD method, for various edge angles $\theta$ and temperature differences $\Delta T$ . . . . . 54

Figure 4.5 Mass flow rate difference in percentage between RK4 and FD method, for various edge angles $\theta$ and temperature differences $\Delta T$ . . . 55

Figure 4.6 Mass flow rate along the fin solved by the FD method for $\theta = 77^\circ$, $\Delta T = -5℃$ and utilizing first set of boundary conditions . . . . . 56

Figure 4.7 Comparison of mass flow rate at the edge along axial direction for FD method with different mesh size . . . . . 57

Figure 4.8 Geometry of the two-dimensional fin top flow domain . . . . . 58

Figure 4.9 Two dimensional solution domain and the coordinate system used in the formulation . . . . . 58

Figure 4.10 Flowchart of two-dimensional flow model . . . . . 62

Figure 4.11 Variation of profile film between $\theta = 88^\circ$ to $\theta = 83^\circ$ edge angle and with a constant temperature difference of $\Delta T = -5℃$ . . . . . 63

Figure 4.12 Axial mass flow rate between $\theta = 88^\circ$ to $\theta = 83^\circ$ edge angle and with a constant temperature difference of $\Delta T = -5℃$ . . . . . 64

Figure 4.13 The ratio of axial mass flow rate over lateral mass flow rate for $\theta = 88^\circ$ to $\theta = 83^\circ$ range of edge angles and with the constant temperature difference of $\Delta T = -5℃$ . . . . . 65

Figure 4.14 Comparison of first derivative of liquid film thickness with respect to $y$ for different number of nodes in $y$-direction along $x$ for the cross sections of a) $j = 0$ and b) $j = M$ . . . . . 66

Figure 4.15 Comparison of net axial mass flow at each cross section in $y$-direction, for different number of node in $y$-direction . . . . . 67

Figure 5.1 A possible flow in transition region from the condensation to evaporation section . . . . . 70

## LIST OF ABBREVIATIONS

| | |
|---|---|
| $A_d$ | Dispersion coefficient, J |
| $c$ | Accommodation constant |
| $h_{lv}$ | Latent heat of evaporation, J kg$^{-1}$ |
| $k_l$ | Thermal conductivity, W m$^{-1}$ K$^{-1}$ |
| $L$ | Length of fin top, m |
| $\dot{m}'_x$ | Mass flow rate per unit depth in $x$-direction, kg m$^{-1}$ s$^{-1}$ |
| $\dot{m}'_y$ | Mass flow rate per unit depth in $y$-direction, kg m$^{-1}$ s$^{-1}$ |
| $\dot{m}''_c$ | Condensation mass flux, kg m$^{-2}$ s $^{-1}$ |
| $M$ | Molar mass of liquid, kg mol$^{-1}$ |
| $P_d$ | Disjoining pressure, Pa |
| $P_c$ | Capillary pressure, Pa |
| $P_l$ | Liquid pressure, Pa |
| $P_v$ | Vapour pressure, Pa |
| $R$ | Liquid-vapor interface radius, m |
| $R_u$ | Universal gas constant, J mol$^{-1}$ K $^{-1}$ |
| $t$ | Condenser length in axial direction, m |
| $T$ | Temperature, K |
| $T_{lv}$ | Temperature of liquid-vapor interface, K |
| $T_v$ | Temperature of vapor, K |
| $T_w$ | Temperature of wall, K |
| $u$ | Fluid velocity in lateral direction, m s$^{-1}$ |
| $v$ | Fluid velocity in axial direction, m s$^{-1}$ |
| $W$ | Groove width, m |
| $x$ | Coordinate along the width of heat pipe, m |

| | |
|---|---|
| $y$ | Coordinate along the heat pipe axis, m |
| | ***Greek Symbols*** |
| $\theta$ | Contact angle, $^\circ$ |
| $\delta$ | Film thickness, m |
| $\mu$ | Dynamic viscosity, Pa s |
| $\nu$ | Kinematic viscosity, $m^2\ s^{-1}$ |
| $\rho$ | Density, kg $m^{-3}$ |
| $\sigma$ | Surface tension, N $m^{-1}$ |
| | ***Subscripts*** |
| $c$ | Capillary |
| $d$ | Disjoining |
| $l$ | Liquid |
| $lv$ | Liquid-vapor |
| $v$ | Vapor |
| $w$ | Wall |
| $x$ | First derivative with respect to $x$ |
| $xx$ | Second derivative with respect to $x$ |
| $xxx$ | Third derivative with respect to $x$ |
| $xxxx$ | Fourth derivative with respect to $x$ |
| $y$ | First derivative with respect to $y$ |
| $yy$ | Second derivative with respect to $y$ |
| $yyy$ | Third derivative with respect to $y$ |
| $yyyy$ | Fourth derivative with respect to $y$ |
| | ***Superscripts*** |
| $'$ | First derivative with respect to $x$ |
| $''$ | Second derivative with respect to $x$ |
| $'''$ | Third derivative with respect to $x$ |
| $''''$ | Fourth derivative with respect to $x$ |

# CHAPTER 1

# INTRODUCTION

Nowadays, rapid enhancements in electronics and computer technology result in designing and manufacturing chips with high capacity and smaller sizes, which leads to a significant increase in heat dissipation and reduction in heat removal areas. The efficiency and performance of these microchips depend on some factors, which cooling process is one of them. Therefore, high heat fluxes generated by microchips have to be removed with a proper cooling system to prevent a reduction in the whole system's efficiency. A phase change mechanism is used in micro heat transfer devices to remove a large amount of heat with a small temperature difference between the heat sink and the heat source regions. One common type of these micro heat transfer device is heat pipes.

## 1.1 Heat Pipes

Heat pipes are passive devices that utilize phase-change process and seek to transfer large amounts of heat in small distances with small temperature differences. Heat removal in electronic devices plays a vital role in keeping the system's efficiency at a high level. Heat pipes consist of three sections: evaporator, adiabatic section, and condenser. Fig. 1.1 shows different regions of wicked heat pipes and their working cycle.

In the working cycle, heat is applied to the evaporator section, and it causes the working fluid to evaporate. Vapor travels to the condenser, where it condenses on the heat pipe walls due to the temperature difference between wall and vapor. Capillary action, which is supplied by a wick structure, creates a driving force for a liquid to flow back

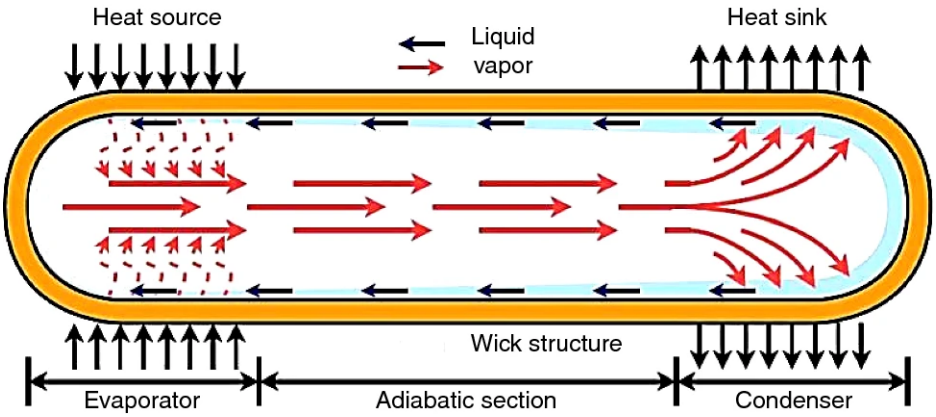


Figure 1.1: Heat pipes scheme and working cycle [1]

from the condenser to the evaporator section. As long as there is a wick structure and temperature difference exists in the system, the cycle continues to work, and there isn't any need for external flow supply devices like pumps. Wicks (Fig. 1.2) can be made using different physical structures such as grooves, screen mesh, and sintered.

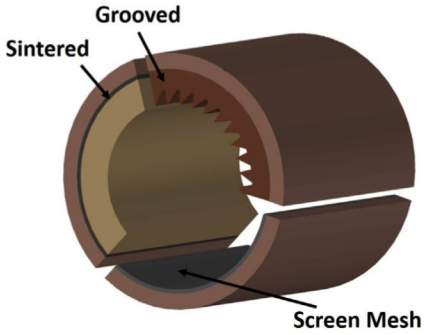


Figure 1.2: Different wick structures [2]

### 1.1.1 Types of heat pipes

There are different types of heat pipes used in various applications. The simplest and most common type is the cylindrical heat pipes, consisting of cylindrical cross-sections and different wick structures. The other kind of heat pipe is flat heat pipes, which due to their geometry, have wide applications in electronic devices. These heat pipes have a rectangular cross-section, and the working mechanism of both flat and cylindrical heat pipes are the same. Another heat pipe type is capillary pumped

loop heat pipes (CPL), which are widely used in spacecraft applications. A two-phase reservoir in these heat pipes enables them to control both the working fluid and the working temperature of the system. The basic schematic of these heat pipe's structures is presented in Fig. 1.3.

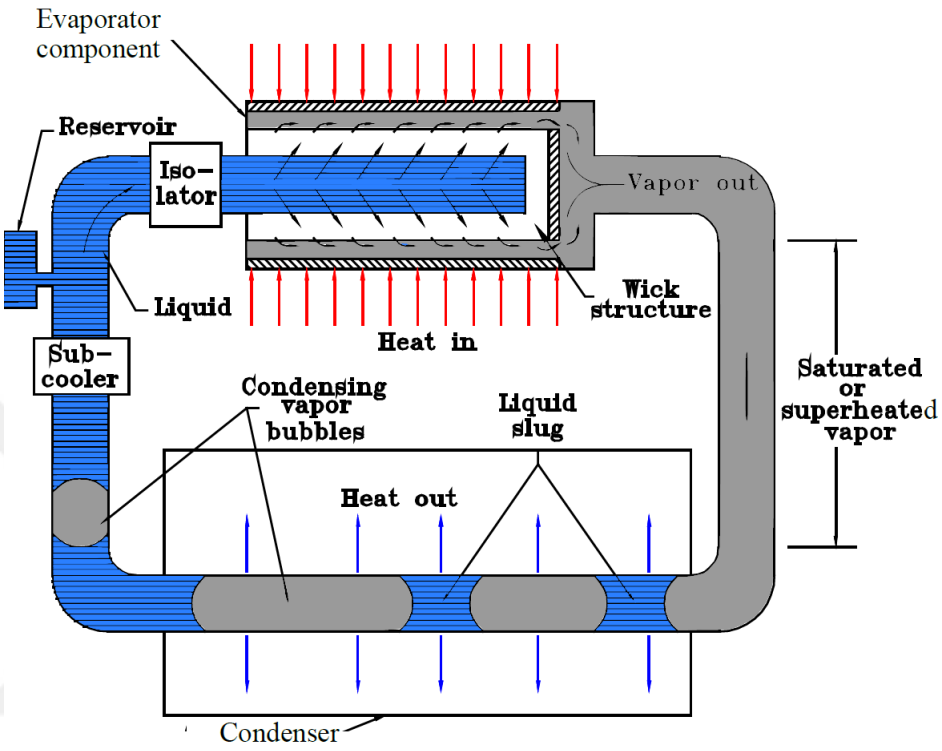


Figure 1.3: Capillary pumped loop heat pipes [3]

Loop heat pipe is another type of heat pipe that can provide reliable operation over long distances. Differing from conventional heat pipes, loop heat pipes have separate vapor and liquid lines and a compensation chamber. The ability to remove heat over long distances without being sensitive to gravity makes them an attractive choice for spacecraft applications. Fig. 1.4 shows the operating cycle of a loop heat pipe.

Micro heat pipes are the type of heat pipes that can have a noticeable heat removal for the cooling process in electronic devices. In the micro heat pipes, the mean curvature of the liquid-vapor interface is comparable in magnitude to the reciprocal of the hydraulic radius of the total flow channel. Micro heat pipes can have different cross-sectional shapes as shown in Fig. 1.5.

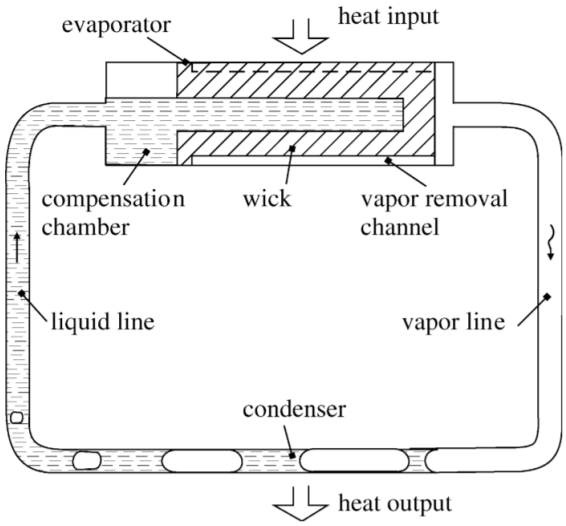


Figure 1.4: Principal scheme of loop heat pipes [4]

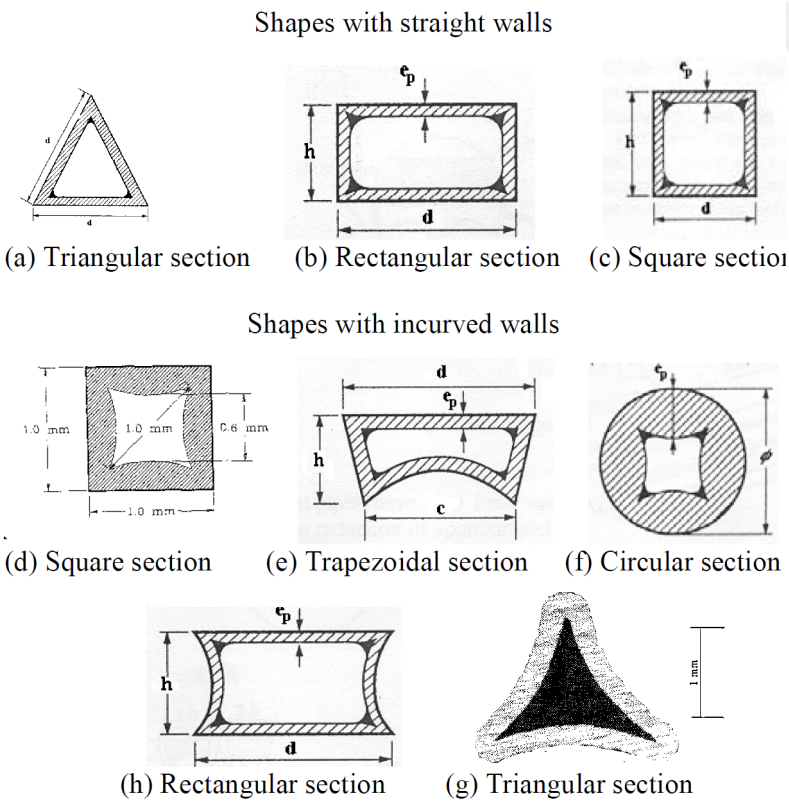


Figure 1.5: Various cross-sections of micro heat pipes [5]

## 1.2 Dimensions of grooved heat pipes

In order to model realistic grooved heat pipes, it's crucial to be familiar with the dimensions. Alijani et al. [6] fabricated four aluminum flat grooved heat pipes and experimentally investigated the effect of filling ratio on the thermal performance. In this study, the fin width and groove width vary in the range $200\ \mu m \sim 1600\ \mu m$. The geometry of grooved heat pipe is given in Fig. 1.6. In the current study, the fin and groove width are taken as $400\ \mu m$ and $400\ \mu m$, respectively.

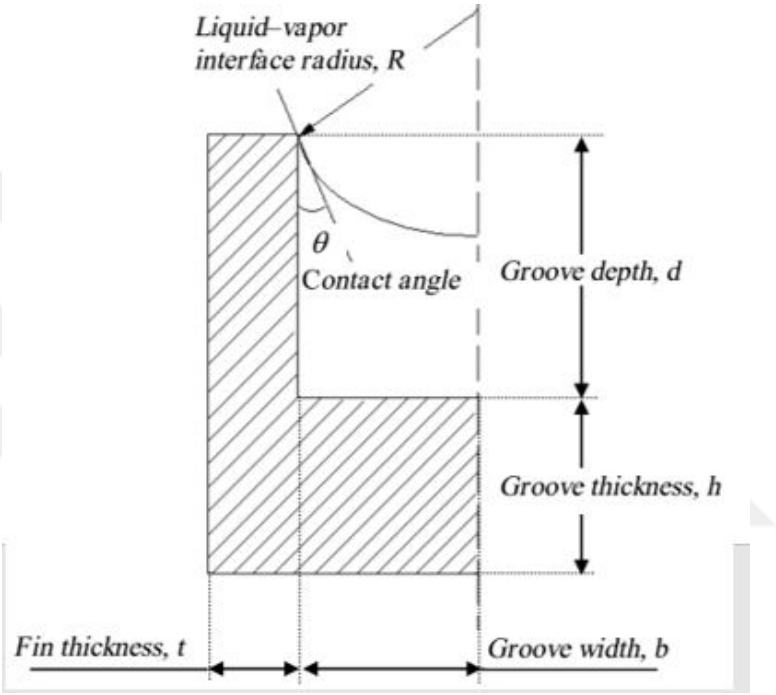


Figure 1.6: Geometry of grooved heat pipe [7]

## 1.3 Literature Review

The research of Potash and Wayner [8] was one of the earliest studies that presented a mathematical model for the evaporation section considering the disjoining pressure to calculate the heat flux variation and meniscus profile. They suggested that the pressure drop due to the change in the extended meniscus profile was adequate to provide the fluid flow required for evaporation. Moosman et al. [9] utilized perturbation theory to find the meniscus profile, and they noted that the major percentage of

evaporative flux occurs in the adsorbed and capillary meniscus. Moreover, they eliminated the interface temperature, replaced it with the wall temperature, and defined a new temperature jump between the wall and the vapor. Dasgupta et al. [10] solved the Young-Laplace equation to evaluate the experimental data for an extended meniscus, and they utilized the lubrication assumption for the fluid flow. Except for the slight deviation at the transition region, the experimental observation of film thickness and theoretically calculated film thickness matched well. Stephan et al. [11] presented a mathematical model which was based on combining the conservation of mass and momentum equations. The governing single differential equation was solved numerically with the fourth-order Runga-Kutta method. They noted that the assumption of an equality of the interface temperature and the saturation temperature of the vapor could result in over-prediction of the heat transfer coefficient. Mirzamoghadam et al. [12] developed an integral model to calculate the meniscus profile utilizing an approximate temperature distribution and liquid film velocity. The approach was similar to the analysis of the boundary layer, and it resulted in predicting heat transfer based on the inclination angle of the plate. Akkuş and Dursunkaya [13] introduced a novel approach to solve the governing equation of evaporation and the liquid flow in the extended meniscus region. The starting point for solving the governing equation was in the intrinsic meniscus, where disjoining pressure is negligible, and as a result, the modification for the boundary conditions was eliminated. The results were compared to the results of Stephan et al. [11], and it turned out that the heat flux distribution was similar near the intrinsic region. However, near the contact line, where disjoining pressure is dominant, the heat flux increased more rapidly and reached its maximum value, which was $6$ percent higher than the heat flux obtained by [11], and then suddenly dropped to zero.

Holm and Goplen [14] developed a model to explore the mass and heat transfer from a wetting surface through capillary grooves. The equations represent the mass and heat transfer solved simultaneously for the flow inside of the capillary grooves. A region with a high heat transfer rate was found, which accounted for about $80$ percent of heat dissipation from the wall. They called this area the thin film transition region located at the apex of the intrinsic meniscus. The most crucial contribution provided in this study was presenting an approximate method to detect the mass and heat trans-

fer effects that occur near the liquid-solid-vapor interface. Jiao et al. [15] presented a theoretical and experimental model to predict the heat transfer characteristics of the thin film evaporator and condenser in grooved heat pipes. The experimental results showed good agreement with the numerical results. They noted that the temperature drop in the evaporator is much bigger than the condenser with the same heat load. Also, the results showed that the reduction in contact angle decreases the meniscus radius, which directly improves capillary pumping and heat transfer capacity. Sosnowski et al. [16] introduced a numerical model for simulation of evaporation and condensation of thin water film with conjugated heat transfer. They reproduced the model of Laaroussi et al. [17], and included the thermal characteristics of the solid part, to demonstrate the importance of conjugate heat transfer. It was shown that the phase transition, which is strongly dependent on the thermal properties of the solid, determines the flow pattern. Xiao and Faghri [18] proposed a three-dimensional mathematical model to analyze thermal and hydrodynamic behaviors of flat heat pipes. It turned out that adding a vertical wick column in the vapor core improves thermal resistance and capillary limit. Moreover, the results showed that applying a higher heat input in the evaporation region leads to an increase in pressure drop, surface temperature, and fluid velocities in the wicks and vapor chamber, which improve the thermal performance of flat heat pipes. Ranjan et al. [19] also presented a three-dimensional numerical model for thermal transport in flat heat pipes considering the effect of wick micro-structure. In some studies in the literature [20–22], composite wick structures were utilized in heat pipes in order to obtain both high capillary pressure and high vapor permeability, which couldn't be achieved via a single type of wick structure. Li et al. [20] developed numerical and experimental models for the evaporation and condensation heat transfer in a copper-water wicked heat pipe with a sintered-grooved composite wick structure. The results showed that the thermal resistance of the condenser remains constant even when the heat pipe dries, and it was fairly predicted well by the numerical model. Also, it was seen that applying higher heat load leads to spending more time driving the heat pipes to reach equilibrium.

Condensation occurs in two distinct modes depending on the surface on which the vapor condenses, dropwise and filmwise [23, 24]. In dropwise condensation, the surface is non-wettable, and when the vapor condenses, droplets are formed. However,

in filmwise condensation, the surface is wettable, and as condensation occurs, a continuous film is formed. Dropwise condensation increases the heat transfer rate by ten times compared to filmwise condensation. Fil et al. [25] presented a review to focus on the underlying the physics and application of the dropwise condensation. Dropwise condensation can transfer a significant amount of heat with a small temperature difference compared to film condensation. However, industrial applications of dropwise condensation are limited because of the poor durability of the promoter coatings. Researchers promote wetted surfaces, which is more appropriate for filmwise condensation. In the literature, some studies were conducted to modify the surface to have an efficient and promoted dropwise condensation. Goswami et al. [26] presented a review study in surface modification to enhance dropwise condensation. There are two main approaches to achieve this purpose in the literature: utilizing low surface coatings such as organic mono-layers, noble metals, graphene, and polymers and producing micro-nano surface features to control droplet formation and removal. Lee et al. [27] fabricated micro-nano scaled porous on the plain surfaces of steam condenser tubes and measured the heat transfer rate. Results showed that adding porous surfaces increases heat transfer rates of dropwise condensation by limiting the growth of large condensate droplets. By utilizing an image analyzing technique, Zheng et al. [28] presented an experimental model to investigate the growth characteristics of a condensing sessile drop in dropwise condensation. They used interference microscopy in measuring the curvature to calculate the pressure field and the Kelvin-Clapeyron model of interfacial mass flux to obtain the interfacial temperature difference. The experimental observation revealed that with constant condensation heat flux, the apparent contact angle remained the same while the radius of curvature of the growing droplet increased linearly over time.

In grooved heat pipes, the surface is wettable, and filmwise condensation takes place on the fin top. A smaller number of models have been developed for the condensation section in grooved heat pipe compared to the evaporation section. Most of the evaporation takes place at the edge of the groove. However, due to thinner liquid film on the fin top than in the meniscus, most of the condensation occurs on the fin top. Zhang and Faghri et al. [29] used the volume of fluid (VOF) method to model the condensation on the fin top of a rectangular grooved heat pipe. They investigated the effect

of contact angle, film thickness, surface tension, and wall temperature on the condensation heat transfer. The results demonstrated that the liquid film became flatter on the fin top as the contact angle increased. They concluded that increasing the surface tension lowered the liquid film thickness. This happened because the surface energy must be minimized, which can be reached by an increase in the radius of curvature. As a result, the thickness of the film decreases. Kamotani [30] presented a model for predicting the film thickness variation on the fin top of a grooved heat pipe condenser. In modeling the liquid flow, it was assumed that the force balance was between viscous and pressure terms. The liquid film motion on the fin top is studied separately in two regions; flat area and round corner region. Approximate fourth-order polynomial profiles were fitted to the liquid film for both areas. He concluded that the condensation rate in axially grooved heat pipes depends on the working fluid, radius of the curvature of the liquid meniscus in the groove, and the groove dimensions. Also, he noted that the condensation rate for given groove geometry and working fluid remained constant if the pipe wall temperature was kept constant. Do et al. [31] developed a mathematical model to predict the thermal performance of rectangular micro-grooved heat pipes. In the condensation region, he also fitted an approximate fourth-order polynomial profile for the liquid film at the fin top. The governing equation was derived from the augmented Young-Laplace equation, conservation of mass, and linear momentum in the lateral direction. The effect of disjoining pressure had been neglected. Odabasi [7] used the same method as Do et al. [32] to model the condensation region. Launay et al. [33] developed a mathematical model for predicting the thermal performance of a micro heat pipe array filled with water. This model was the combination of hydrodynamic flow and heat transfer equations for film profile at both the condensation and evaporation regions.

The boundary conditions used at the condensation region for both studies of Do et al. [31] and Launay et al. [33] were the same, which can be written as:

$$\frac{d\delta}{ds}|_{s=0} = \frac{d^3\delta}{ds^3}|_{s=0} = 0, \frac{d^2\delta}{ds^2}|_{s=\frac{T}{2}} = \frac{1}{r_c}, \frac{d\delta}{ds}|_{s=\frac{T}{2}} = -\tan\left(\frac{\pi}{2} - \Upsilon\right) \tag{1.1}$$

Where $\Upsilon$ is the edge angle of film. For flat plate micro-grooved heat pipes, Lefevre et al. [34] presented a hydrodynamic model for the liquid and the vapor flow coupled

with the thermal model. In the condensation zone, the result of the two thermal models demonstrated that due to the lower thermal resistance of the fin compared to the liquid in the groove, most of the condensation occurred on the fin top. This model was developed to calculate the film thickness, pressure, and velocity of the liquid in the fin top. The governing equation was based on the conservation of mass, linear momentum and Young-Laplace equation.

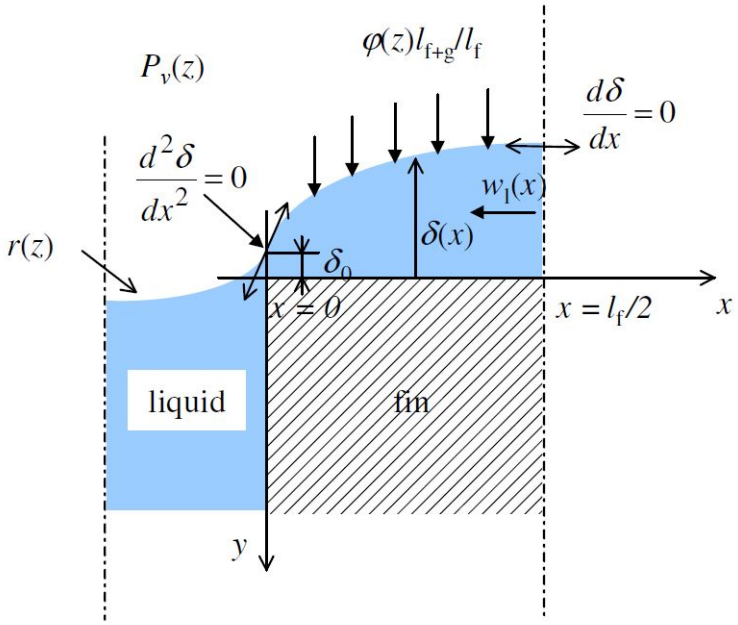


Figure 1.7: Boundary conditions used in [34]

The four boundary conditions are shown in Fig. 1.7: due to symmetry, the first and third derivatives of delta are zero at the beginning, and at the edge of the fin because of the vapor and liquid pressure equality, the second derivative of delta was assumed to be zero. The final boundary condition at the edge satisfied the contact angle. In this research, the Runge-Kutta method was used to solve the fourth-order differential equation, and also they neglected the effect of disjoining pressure and possible axial flow on the fin top. Lips et al. [35] presented a comparison between the interface shape measurements from experimental observation and the theoretical data which was obtained in the previous study [34], hydrodynamic modeling of flat plate micro-grooved heat pipes. There was a satisfactory agreement in the evaporation region, and the theoretical results matched the experimental results. However, the condensation

model overestimated the liquid-vapor interface shape on the fin top.

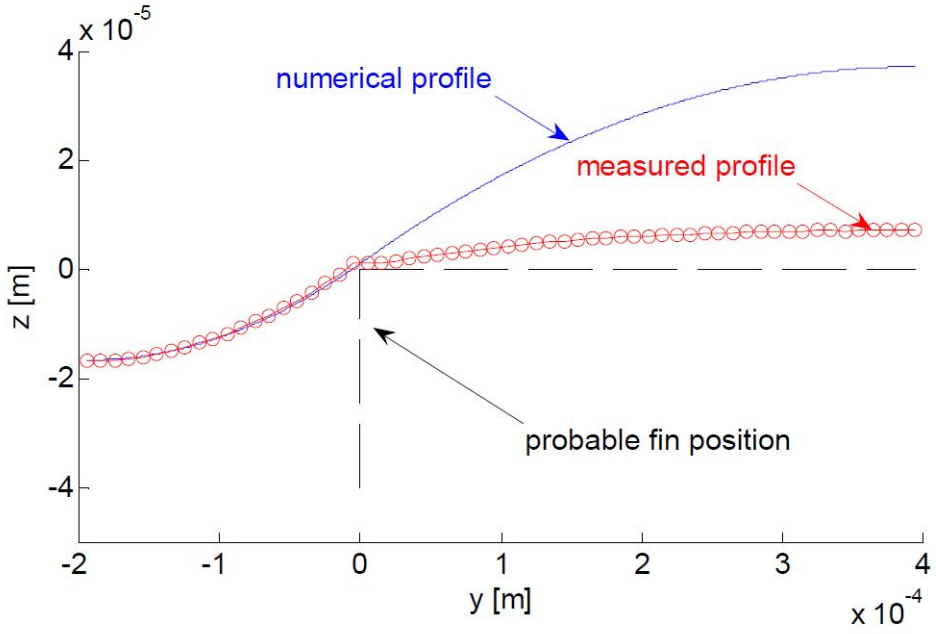


Figure 1.8: Comparison between numerical and experimental liquid-vapor interface shape [35]

In Fig. 1.8, a change in the slope of the liquid profile before the fin edge can be observed, and the authors called this a "slope break". In the literature, there wasn't any slope break in the numerical modeling before, and [35] was the first study that captured this change experimentally. The authors provided two possibilities for this slope break: first, possibilities of a flow in the y-direction( parallel direction to the groove), and the second is that van der Waals forces for small film thickness can be added, which was neglected in this study. Alipour and Dursunkaya [36] developed a model of condensation film profile on the fin top of micro-grooved heat pip considering the effect of disjoining pressure. Although for thicker films disjoining pressure effect is negligible, it becomes dominant in comparison with the capillary pressure term for thinner profiles. This study demonstrated that disjoining pressure affects the solution domain and brings a limit for the contact angle for a given temperature difference. In this study, the same set of boundary conditions and numerical approach was used as before in [34].

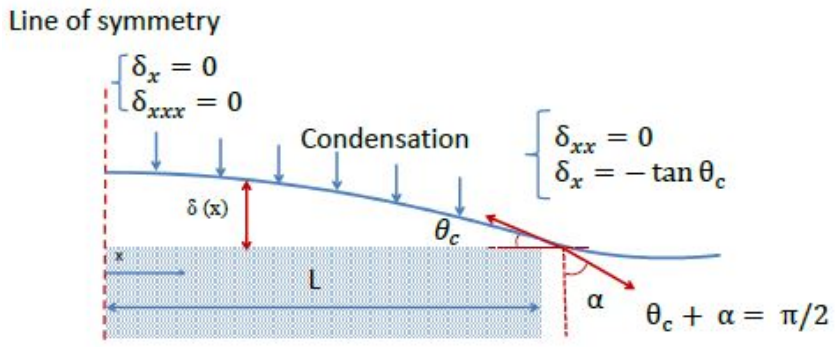


Figure 1.9: Boundary conditions used in [37]

Akdağ et al. [38] presented a novel approach in the modeling of condensation region. Unlike the other studies in the literature, they started the solution domain from a point on the vertical wall of the groove, which keeps the edge of the fin top inside the solution domain. There isn't a need to set boundary conditions at the corner. The effect of disjoining pressure was taken into account which gives a comprehensive understating of molecular forces for thinner films.

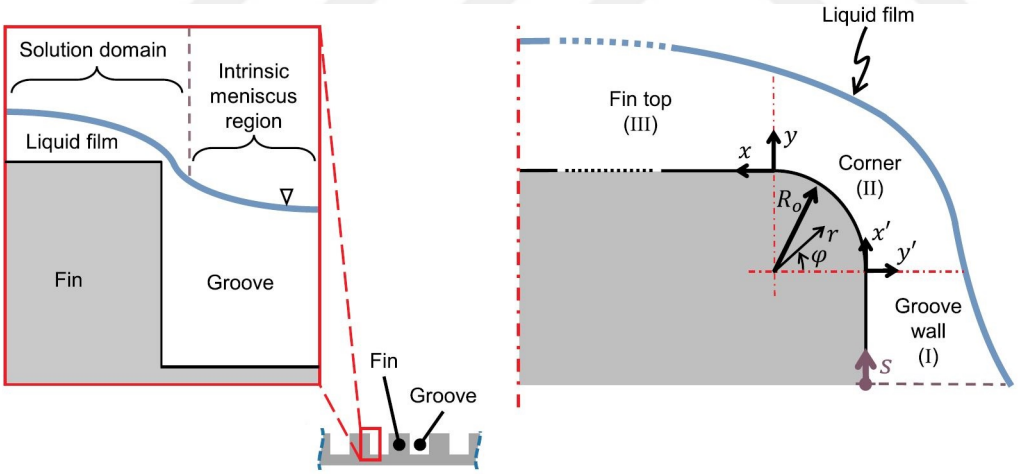


Figure 1.10: Solution domain at [38]

The governing equation consisted of the conservation of mass and momentum equation, Kucherov-Rikenglaz equation, and Young-Laplace equation which were solved simultaneously to calculate the liquid-vapor interface shape. Moreover, the effect of subcooling, dispersion constant, and fin-groove corner radius was investigated. In this

study, it was stated that for the $10^{-3}$K subcooling and 30 nm corner radius, an abrupt change in the slope had been observed, the same slope break was experimentally reported by the previous work [35].

## 1.4 Description and Motivation of the Current Study

The fundamental purpose of this study is to explore the effect of prescribed boundary conditions on the formation of the film profile on the fin top in the condensation section. In this study, at first the condensation film is modeled numerically by solving the governing equations, which consist of conservation of mass and linear momentum, augmented Young-Laplace equation, and the condensation mass flux equation based on the kinetic theory of gases, and then the effect of different sets of boundary conditions are discussed. In the literature, different boundary conditions used at the edge of the fin top. For understanding that which boundary conditions are proper for different edge angles and temperature differences, the numerical results are compered with the exact formulation of Akdağ et al. [38]. This model is most reliable condensation model in the literature, but it can't be implemented in the entire simulation of grooved heat pipes because it can merely solve specified cross-section of film profile on the fin top at a time. However the current condensation model can solve different cross-sections of film profile in a short time, which is desirable for a complete simulation of flow in grooved heat pipes. Also it has to be mentioned that a comprehensive modeling of condensation section is crucial for optimizing grooved heat pipe design.

Furthermore, as it can be understood from the literature review, there is a significant difference between the numerical results and experimental observation. Possible parallel flow in the axial direction on the fin can be responsible for this difference. In the current study a two-dimensional flow model on the fin top is proposed, which has not been investigated and discussed in literature before. A novel numerical approach based on finite difference method is developed to solve the governing $4^{th}$ order nonlinear differential equation.

Chapter 2 refers to the numerical modeling of liquid film on the fin top, and the numerical approach is discussed in detail. Numerical Results and discussions can be

found in Chapter 3. Two-dimensional flow on the fin top is modeled, and preliminary findings are discussed in Chapter 4. In the end, in Chapter 5, conclusion and possible future work is presented.

# CHAPTER 2

# MODELING AND SOLUTION METHODOLOGY

In this chapter, the condensation model on the fin top is mathematically investigated. Conservation of mass, linear momentum, Young-Laplace, and condensation mass flux equation based on the kinetic theory of gases are solved simultaneously to calculate the film thickness and pressure field on the fin top.

## 2.1 Phase change

The phase change is a reversible mechanism of transformation that takes place when a substance's state changes from one to another.

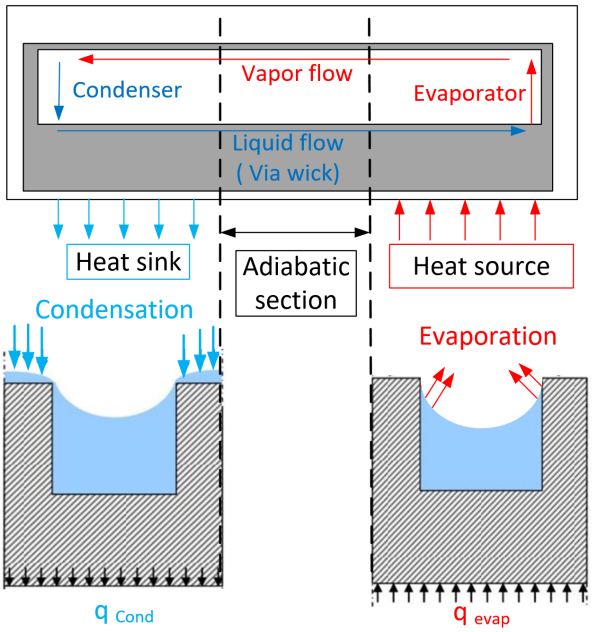


Figure 2.1: Phase change regions in the grooved heat pipe

This mechanism occurs in both the evaporation and condensation regions in heat pipes. By utilizing the phase change process, heat pipes can spread and remove large amounts of heat in shorter distances with small temperature differences.

## 2.2 Capillary pressure

Surface tension forces between two immiscible fluids generated from the interface curvature's deformation create capillary pressure. Capillary pressure is the function of the surface tension and radius of curvature. Capillary pressure generated by two menisci of the various radius of curvature can be represented by the Young-Laplace equation:

$$P_c = \sigma \left( \frac{1}{R_1} + \frac{1}{R_2} \right) \tag{2.1}$$

On the fin top, the radius of the curvature in the axial direction is noticeably large compared to the radius of the curvature in the lateral direction. As a result, its contribution in the Eq. (2.1) can be neglected:

$$P_c = \frac{\sigma}{R} \tag{2.2}$$

The radius of the curvature is the function of the first and second derivatives of liquid-vapor interface film with respect to lateral direction:

$$R = \left| \frac{\left(1 + (\delta')^2\right)^{\frac{3}{2}}}{\delta''} \right| \tag{2.3}$$

Thus, capillary pressure can be written as a function of the first and second derivatives:

$$P_c = \frac{\sigma\, \delta''}{\left[1 + (\delta')^2\right]^{\frac{3}{2}}} \tag{2.4}$$

## 2.3 Disjoining pressure

There is another term in the Young-Laplace equation in addition to capillary pressure, which shows its effect in the case that film thickness is less than 100 nm. This term is called disjoining pressure, and it is caused by the inter-molecular force between solid and liquid. Disjoining pressure can written as a function of film thickness for non-polar fluids:

$$P_d = \frac{A_d}{\delta^3} \tag{2.5}$$

where $A_d$ is the dispersion coefficient.

## 2.4 Lubrication assumption

For the flow of liquid on a thin fin, lubrication approximation is assumed to be valid in the current study. Generally, this theory is used in the journal bearings or thin-film flows, where viscosity becomes dominant in the calculations. This assumption is applicable when the magnitude of film thickness over flow length or the local Reynolds number has to be small enough to apply lubrication theory. In the current study, both terms are adequately small. A detailed justification of lubrication assumption is given in [38].

## 2.5 One dimensional model

### 2.5.1 Solution domain

The solution domain of condensation section can be seen in Fig. 2.2, which shows that it starts from the symmetry line on the fin top, and ends at edge of the groove. All the models will be solved in this region.

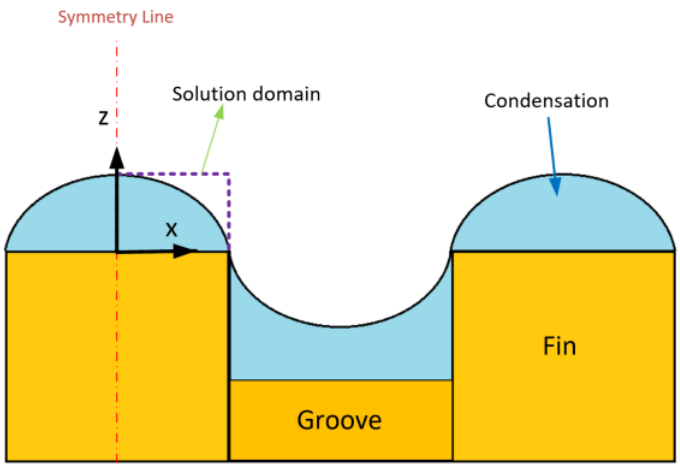


Figure 2.2: One dimensional solution domain

### 2.5.2 Unidirectional flow

By utilizing the lubrication theory, assuming fully developed unidirectional flow and neglecting the effect of gravity, the $x$-momentum equation is reduced to:

$$\frac{dP_l}{dx} = \mu \frac{d^2u}{dz^2} \tag{2.6}$$

In this equation, $\mu$ is the fluid's dynamic viscosity, $P_l$ is the liquid pressure, and $u$ is the fluid velocity in the $x$-direction. The boundary conditions are given as:

$$z = 0 \; ; \; u = 0 \tag{2.7a}$$

$$z = \delta \; ; \; \frac{du}{dz} = 0 \tag{2.7b}$$

Using Eq. (2.7b), zero shear stress at free surface and no-slip boundary condition at wall, Eq. (2.6) can in integrated, which gives the velocity distribution as follows:

$$u\left(z\right) = \frac{1}{2\mu} \frac{dP_l}{dx} \, z \left(z - 2\delta\right) \tag{2.8}$$

By integrating the velocity profile, the mass flow rates per unit depth can be calculated:

$$\dot{m}' = \rho \int_0^{\delta} u \, dz = -\frac{1}{3\nu} \frac{dP_l}{dx} \delta^3 \tag{2.9}$$

The condensation mass flux on the fin top, which was presented by Moosman et al. [9], is a function of film thickness, temperature difference between the vapor and the wall, pressure difference between the liquid and vapor.

$$\dot{m}'_c = \frac{a\,(T_w - T_v) - b\,(P_v - P_l)}{1 + a\delta h_{lv}/k_l} \tag{2.10}$$

Where the factors $a$ and $b$ are defined as:

$$a = \frac{2c}{2-c} \left( \frac{M}{2\pi R_u T_{lv}} \right)^{\frac{1}{2}} \left( \frac{M P_v h_{lv}}{R_u T_{lv} T_v} \right) \tag{2.11}$$

$$b = \frac{2c}{2-c} \left( \frac{M}{2\pi R_u T_{lv}} \right)^{\frac{1}{2}} \left( \frac{V_l P_v}{R_u T_{lv}} \right) \tag{2.12}$$

Mass balance on the fin top can be written as a function of the condensing mass and the change in the mass flow rate as:

$$\frac{d\dot{m}'}{dx} = -\dot{m}'_c \tag{2.13}$$

By substituting the Young-Laplace equation in Eq. (2.9), and assuming a constant vapor pressure :

$$\frac{dP_l}{dx} = -\frac{dP_c}{dx} - \frac{dP_d}{dx} \tag{2.14}$$

$$\dot{m}' = -\frac{1}{3\nu}\,\delta^3\,\frac{dP_l}{dx} = \frac{1}{3\nu}\,\delta^3 \left( \frac{\sigma\,\delta'''}{\left(1+(\delta')^2\right)^{\frac{3}{2}}} - \frac{3\,\sigma\,\delta'\,(\delta'')^2}{\left(1+(\delta')^2\right)^{\frac{5}{2}}} - \frac{3\,A_d\,\delta'}{\delta^4} \right) \tag{2.15}$$

Substituting Eq. (2.15) into Eq. (2.13) :

$$\frac{1}{3\nu}\frac{d}{dx}\left(\frac{\sigma\,\delta'''\,\delta^3}{\left(1+(\delta')^2\right)^{\frac{3}{2}}}-\frac{3\,\sigma\,\delta'\,(\delta'')^2\,\delta^3}{\left(1+(\delta')^2\right)^{\frac{5}{2}}}-\frac{3\,A_d\,\delta'\,\delta^3}{\delta^4}\right) \tag{2.16}$$

$$=-\frac{a\,(T_w-T_v)-b\,(P_c+P_d)}{1+a\delta h_{lv}/k_l}$$

By taking the derivatives and simplifying Eq. (2.16), the governing equation can be obtained as follows:

$$\begin{aligned}\delta'''' =& -\frac{3\,\delta'\delta'''}{\delta}+\frac{3\,(\delta'')^3}{\left(1+(\delta')^2\right)}+\frac{9\,(\delta')^2\,(\delta'')^2}{\left(1+(\delta')^2\right)\delta}-\frac{15\,(\delta')^2\,(\delta'')^3}{\left(1+(\delta')^2\right)^2}\\ &+\frac{9\,\delta'\,\delta''\,\delta'''}{\left(1+(\delta')^2\right)}-\frac{3\nu\left(1+(\delta')^2\right)^{\frac{3}{2}}}{\sigma\,\delta^3}\left[\frac{a\,(T_w-T_v)-b\,(P_c+P_d)}{1+a\delta h_{lv}/k_l}\right]\\ &+\frac{3\,A_d}{\sigma}\left(1+(\delta')^2\right)^{\frac{3}{2}}\left[\frac{\delta''}{\delta^4}-\frac{(\delta')^2}{\delta^5}\right]\end{aligned} \tag{2.17}$$

### 2.5.3 Groove side boundary conditions

Two sets of boundary conditions are defined for our modeling. Each set has four boundary conditions, which are required to solve the $4^{th}$ order differential equation. First, due to the symmetry of film thickness at the centerline, the first derivative of $\delta$ with respect to $x$ should be zero. The mass flow rate should be zero at the centerline due to the symmetry condition. As a result, in order to satisfy Eq. (2.15), the third derivative of $\delta$ with respect to $x$ should be zero as well. The first derivative of film thickness with respect to $x$ at the edge is given by the edge angle. The two sets of boundary conditions are different from each other merely at the second derivative of film thickness with respect to $x$ at the edge. The first set of boundary conditions, the second derivative of $\delta$ is assumed to be zero at the edge, which is commonly used in the literature. It means there is an inflection point of the film profile at the edge of the groove. The first set of boundary conditions is shown in Fig. 2.3. The second set assumes the film to reach the value of the liquid pressure at the edge of the fin.

Therefore, for the second set of boundary conditions, the concavity change of film profile takes place before the edge, which means the inflection point is located before the corner. For this set, the second derivative of film thickness is defined as a function of groove width and edge angle at the edge, which can be seen in Fig. 2.4.

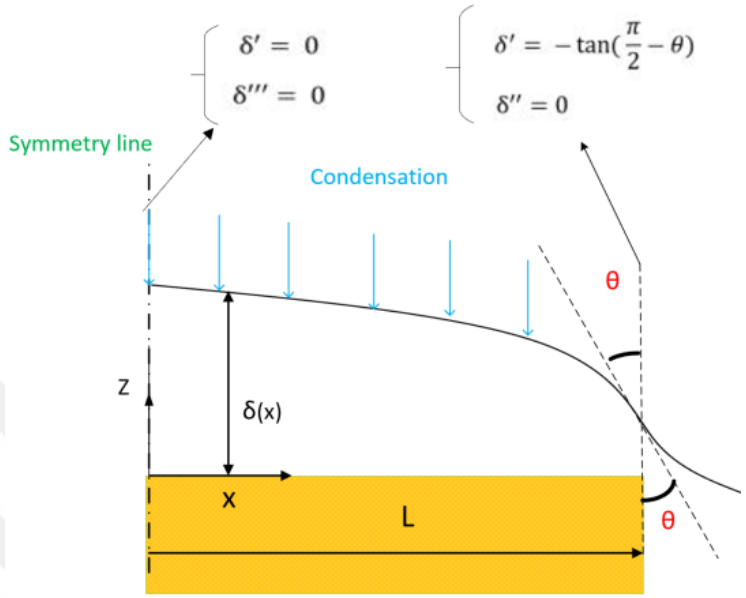


Figure 2.3: First set of boundary conditions

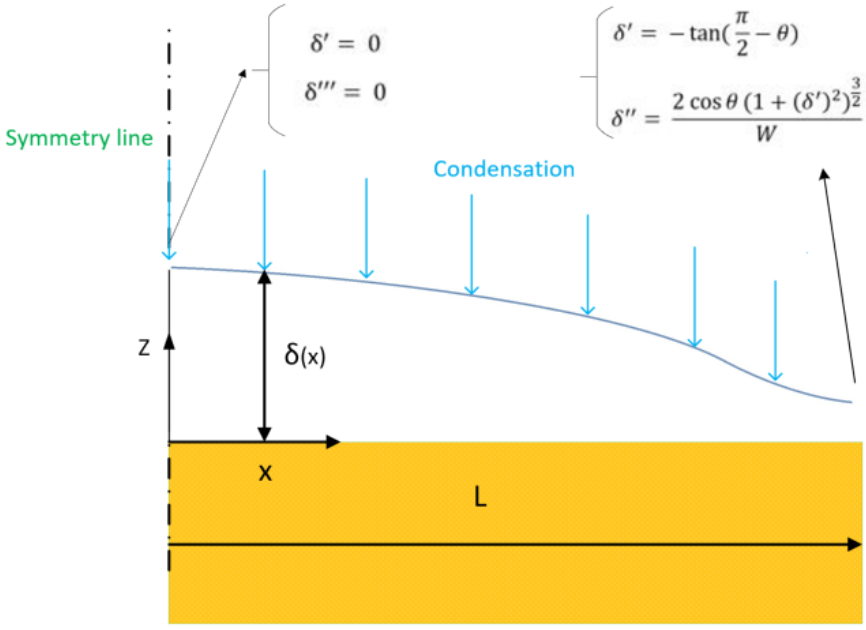


Figure 2.4: Second set of boundary conditions

### 2.5.4 Numerical approach

The governing equation Eq. (2.17) is solved numerically with two different methods. The first one is the fourth-order Runge-Kutta method which has $\mathcal{O}(h^4)$ accuracy. The second approach is based on the finite difference method with $\mathcal{O}(h^2)$ accuracy, which allows investigating the possible axial flow on the fin top. This method is discussed in details in Chapter 4, where it will be used in the formulation and solution of the two-dimensional flow on the fin top. In this section, the numerical process is presented for the Runge-Kutta method.

### 2.5.5 Fourth-Order Runge-Kutta (RK4) Method

Since the governing equation Eq. (2.17) is a $4^{th}$ order ODE, a system of four coupled first-order ODEs can be simultaneously solved to find the solution. Such systems can be presented as follows:

$$\begin{aligned} \frac{d\delta}{dx} &= y_1 \\ \frac{d^2\delta}{dx^2} &= \frac{dy_1}{dx} = y_2 \\ \frac{d^3\delta}{dx^3} &= \frac{dy_2}{dx} = y_3 \\ \frac{d^4\delta}{dx^4} &= f\left(\delta, y_1, y_2, y_3\right) \end{aligned} \tag{2.18}$$

The original problem is a $4^{th}$ order boundary value problem (BVP). To solve this, the problem is formulated as an initial value problem (IVP), and all conditions are assigned at one boundary. A shooting method in conjunction with a multi dimensional Newton-Raphson root finder is used to match the two boundary conditions on the other boundary at the edge of the groove. Therefore, four initial conditions at the centerline are needed to solve this system of equations. $\delta'$ and $\delta'''$ are known, and the value of $\delta$ and $\delta''$ should be guessed in a way that the boundary condition at the edge of the fin must be satisfied. In other words, the guessed values have to be updated continuously until the boundary conditions at $x = L$ are satisfied. The governing equation is nonlinear and stiff, the solver is more sensitive to the initial guesses and, the initial guesses have to be chosen wisely. The solution algorithm is given in Fig. 2.5 in a flowchart.

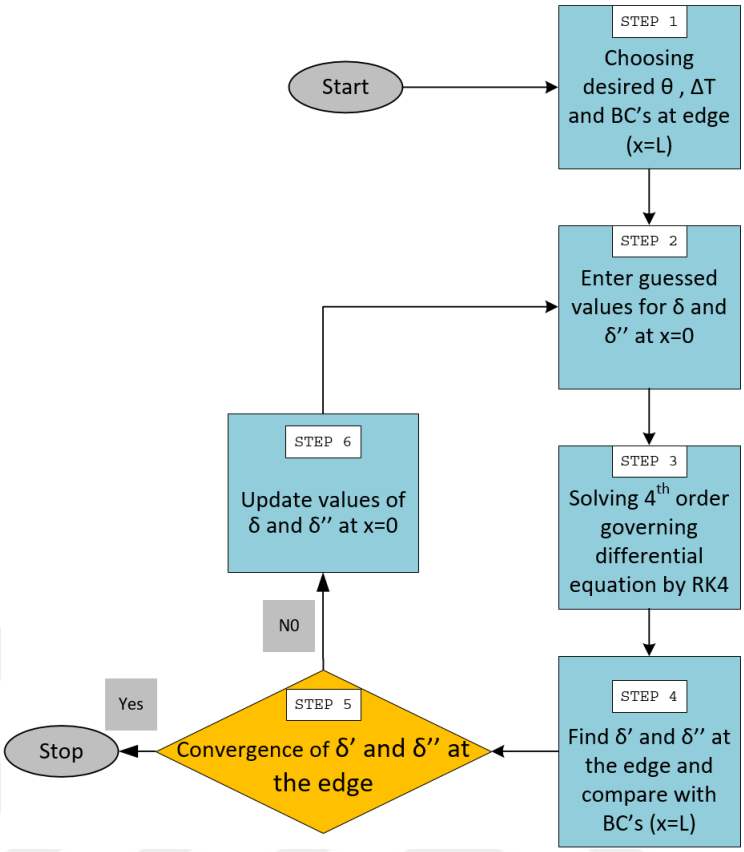


Figure 2.5: Flowchart of Fourth-Order Runge-Kutta Method

# CHAPTER 3

## SIMULATION RESULTS OF ONE-DIMENSIONAL MODEL

Results obtained by the numerical solution are presented in this chapter. There will be two models based on two sets of boundary conditions as described in Chapter 2:

- Model 1: In this case, the inflection point of the film thickness profile is assumed to be at the edge of the fin top, which means that the second derivative of film thickness with respect to $x$ should be zero at the edge. Physically, it means that the liquid and the vapor pressure are equal at this point. In the literature, [7, 36] studies used the same set of boundary conditions to calculate the film thickness in the condenser section, which can be expressed as follows:

$$\begin{aligned} &\text{At} \quad x = 0 \quad ; \quad \frac{d\delta}{dx} = 0 \qquad\qquad \text{and} \quad \frac{d^3\delta}{dx^3} = 0 \\ &\text{At} \quad x = L \quad ; \quad \frac{d\delta}{dx} = -\tan\left(\frac{\pi}{2} - \theta\right) \quad \text{and} \quad \frac{d^2\delta}{dx^2} = 0 \end{aligned} \tag{3.1}$$

- Model 2: In this case, the inflection point is located before the edge of the fin top. Before the inflection point, the liquid pressure is higher than the vapor pressure, and from the inflection point until the edge, the vapor pressure is greater than the liquid pressure. In this case the liquid pressure in the film approaches the liquid pressure inside the groove at the edge of the fin. In the literature, [31, 33] studies used the same boundary conditions which can be written as:

$$\begin{aligned} &\text{At } x \quad = 0; \quad \frac{d\delta}{dx} = 0 \qquad\qquad \text{and} \qquad\qquad \frac{d^3\delta}{dx^3} = 0 \\ &\text{At } x \quad = L; \quad \frac{d\delta}{dx} = -\tan\left(\frac{\pi}{2} - \theta\right) \quad \text{and} \quad \frac{d^2\delta}{dx^2} = \frac{2\cos\theta\left(1 + (\delta')^2\right)^{\frac{3}{2}}}{W} \end{aligned} \tag{3.2}$$

where $W$ is the width of the groove, and $\theta$ is the edge angle. As it can be seen from Eq. (3.1) and Eq. (3.2), except for the second derivative of film thickness at the edge,

Model 1 and Model 2 have the same boundary conditions. In this study, the operating fluid is water, and the length of the fin top and the width of the groove are considered to be $400\ \mu\mathrm{m}$ and $400\ \mu\mathrm{m}$, respectively. The physical properties for the modeling are listed as below:

Table 3.1: Thermophysical properties and geometrical parameters used in the condensation modeling

| Parameter | Magnitude | Unit |
|---|---|---|
| Fin top length, $2L$ | $400 \times 10^{-6}$ | m |
| Groove width, $W$ | $400 \times 10^{-6}$ | m |
| Vapor pressure, $P_v$ | $1.033 \times 10^{5}$ | Pa |
| Vapor temperature, $T_v$ | 343 | K |
| Latent heat of evaporation, $h_{lv}$ | $2.3 \times 10^{6}$ | J/kg |
| Density of liquid, $\rho$ | 1000 | kg/m$^3$ |
| Surface tension, $\sigma$ | $5.89 \times 10^{-2}$ | N/m |
| Dynamic viscosity, $\mu$ | $2.79 \times 10^{-4}$ | Pa.s |
| Thermal conductivity, $k_l$ | 0.6 | W/m$\cdot$ K |
| Molar mass of liquid, $M$ | $18 \times 10^{-3}$ | kg/Mol |
| Molar volume of liquid, $V_l$ | $18 \times 10^{-6}$ | m$^3$/Mol |
| Accommodation coefficient, $c$ | 1 | - |
| Dispersion constant, $A_{disj}$ | $5 \times 10^{-21}$ | - |

## 3.1 Fourth-order Runge-Kutta (RK4) solver

In this section, the governing equation for film thickness is solved using $4^{th}$ order Runge-Kutta method. Generally, models vary based on the solving method and used boundary conditions. The number of nodes along the fin top is $20000$, which brings higher accuracy and allows to find a solution for lower edge angles with small temperature differences.

Although the Runge-Kutta method has a high accuracy of $\mathcal{O}(h^4)$, the number of nodes is vital for the solutions with the lower edge angles. The problem should be solved for a sharp slope with different nodes to find the proper mesh size. Assuming $\theta = 20°$ and $\Delta T = -5℃$, including the effect of disjoining pressure and utilizing Model 1 set of boundary conditions, the mass flow rate is calculated.

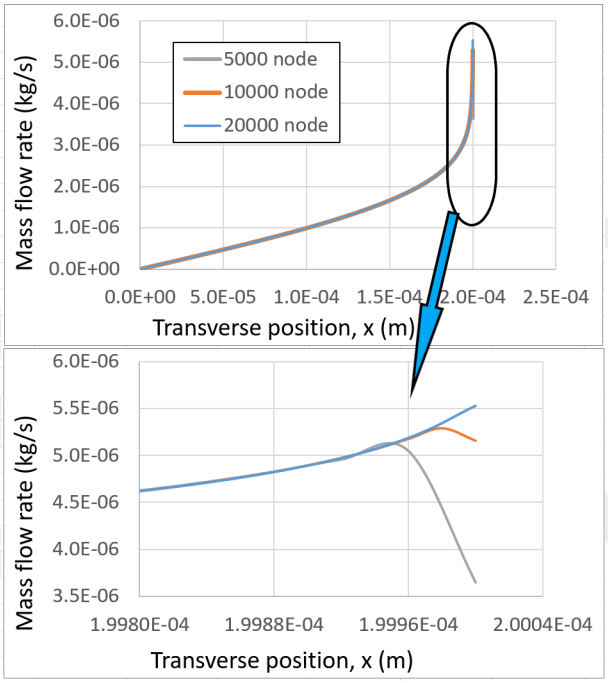


Figure 3.1: Comparison of Mass flow rate along $x$ direction for $5000$, $10000$ and $20000$ number of nodes with $\theta = 20°$, $\Delta T = -5℃$

Since there is a constant condensation mass flux on the fin top, the mass flow rate has to be increased along the $x$ direction due to the conservation of mass. From Fig. 3.1, it can be seen that the mass flow rate for the models with $5000$ and $10000$ nodes is decreased near the edge zone, and because of that, the solution can not be valid. However, the model with $20000$ nodes can be solved without such error. It's crystal clear that the derivatives will be calculated more precisely with more nodes, and as a result, the correct solution can be captured.

## 3.2 Comparison of predictions of different groove side boundary conditions with the exact formulation

In this section, the results are validated with the most reliable condensation model in the literature. Akdağ et al. [38] developed a novel approach to model the flow on the fin top in the condensation section; unlike the other studies in the literature, they start the solution of the problem from inside of the groove, which eliminates the need to set assumed boundary conditions at the groove edge. Working fluid is water, and the fin top length and groove width are $400\ \mu\mathrm{m}$ and $400\ \mu\mathrm{m}$, respectively. The film profiles variation for the edge angles of $\theta = 65°$, $\theta = 75°$ and $\theta = 85°$ with the temperature difference of $\Delta T = -1℃$ are compered between models. Film profiles variation for Model 1, Model 2 and the reference exact formulation model are plotted in Fig. 3.2, Fig. 3.3 and Fig. 3.4.

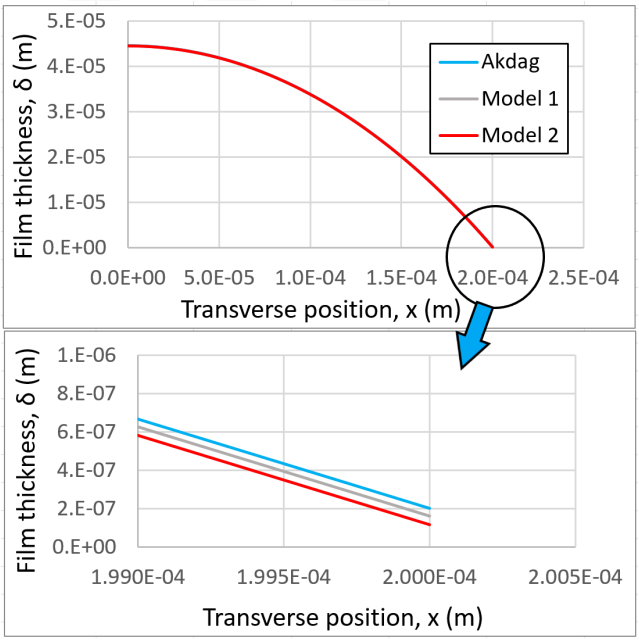


Figure 3.2: Comparison of film profile variation of Akdağ [39] with the two current models for $\theta = 65°$ and $\Delta T = -1℃$

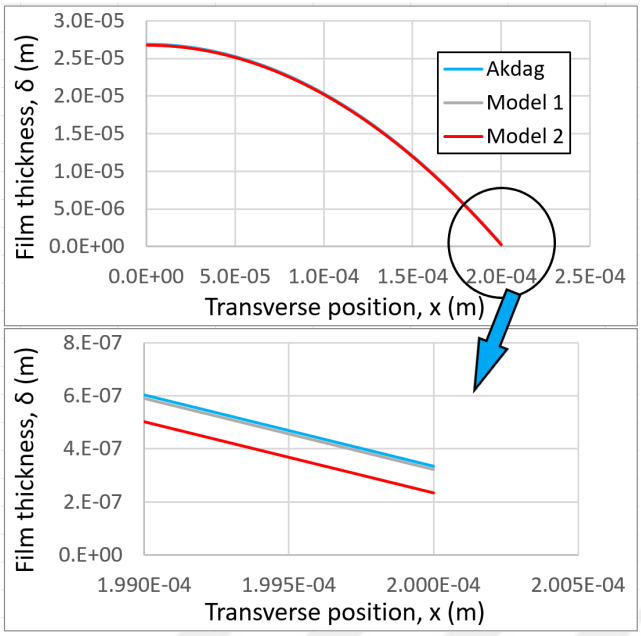


Figure 3.3: Comparison of film profile variation of Akdağ [39] with the two current models for $\theta = 75°$ and $\Delta T = \ -1℃$

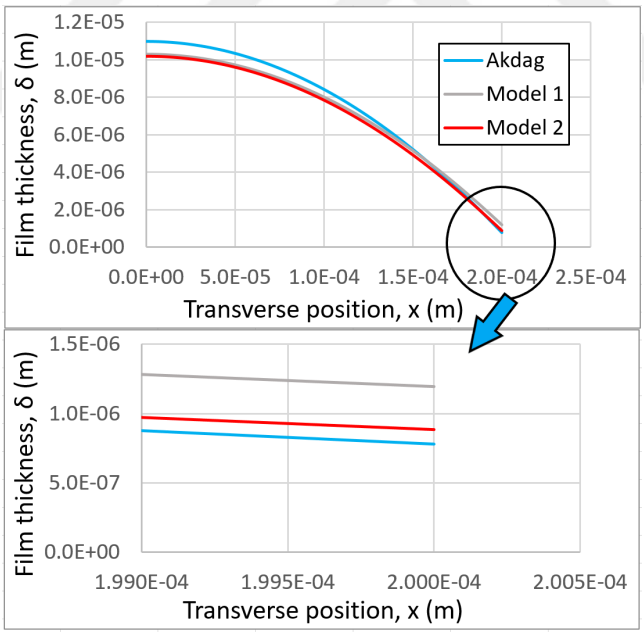


Figure 3.4: Comparison of film profile variation of Akdağ [39] with the two current models for $\theta = 85°$ and $\Delta T = \ -1℃$

Since there is a small deviation between the film profiles of the models, it's better to

compare and plot the mass flow rate at the edge of the fin for the two models.

It can be seen from Fig. 3.2, Fig. 3.3 and Fig. 3.4 that with a specified temperature difference, for higher edge angles, Model 2 and for the lower edge angles Model 1 matches the reference model [38] well.

From [39], it is found out that the second derivative of film profile at the fin edge for the reference model is not constant, and it changes for different edge angles and temperature differences. Since the solution approach of the current model and the model given in [38] are different from each other, for the proper validation, a new model, Model 3, is introduced. Model 1, Model 2 and Model 3 have the same boundary conditions except for the second derivative of film thickness at the edge. As mentioned before, for Model 1, the second derivative of film thickness at the edge is assumed to be zero. For Model 2, the second derivative of film thickness is defined as a function of edge angle and groove width. In Model 3, the second derivative of the film profile at the edge comes from the model given in [39]. By comparing the numerical results of Model 1, Model 2 and Model 3 with the model of [39], it can be understood which sets of boundary conditions are proper as a function of edge angles and temperature differences. Boundary conditions used in Model 3 are:

$$\begin{aligned} &\text{At} \quad x = 0 \quad ; \quad \frac{d\delta}{dx} = 0 \qquad\qquad \text{and} \qquad \frac{d^3\delta}{dx^3} = 0 \\ &\text{At} \quad x = L \quad ; \quad \frac{d\delta}{dx} = -\tan\left(\frac{\pi}{2} - \theta\right) \quad \text{and} \quad \frac{d^2\delta}{dx^2} \text{ from [39]} \end{aligned} \tag{3.3}$$

The variation of film thickness for the models with edge angles of $\theta = 65°$, $\theta = 75°$ and $\theta = 85°$ with the temperature difference of $\Delta T = -1℃$ are plotted in Fig. 3.5, Fig. 3.6, and Fig. 3.7.

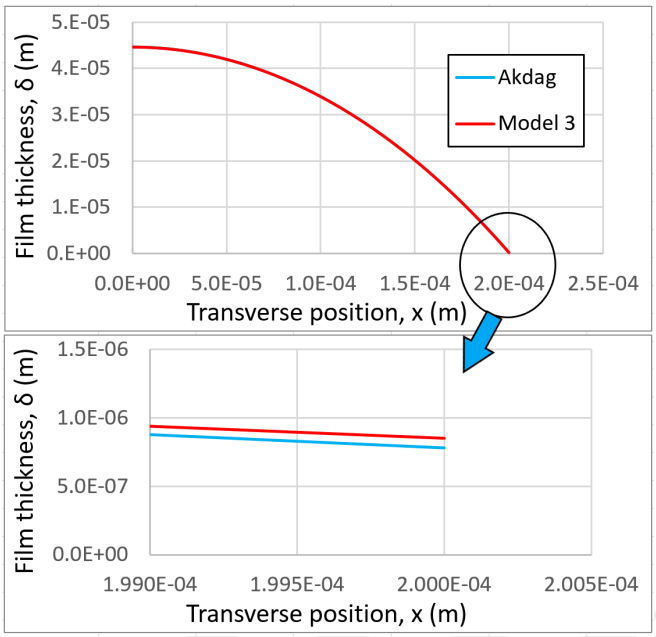


Figure 3.5: Comparison of film profile variation of Akdağ [39] with Model 3, for $\theta = 65°$ with $\Delta T = -1℃$

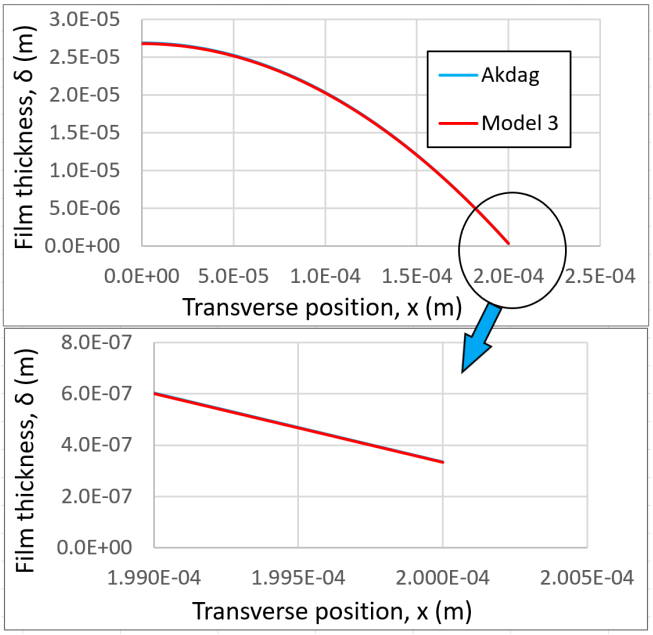


Figure 3.6: Comparison of film profile variation of Akdağ [39] with Model 3, for $\theta = 75°$ with $\Delta T = -1℃$

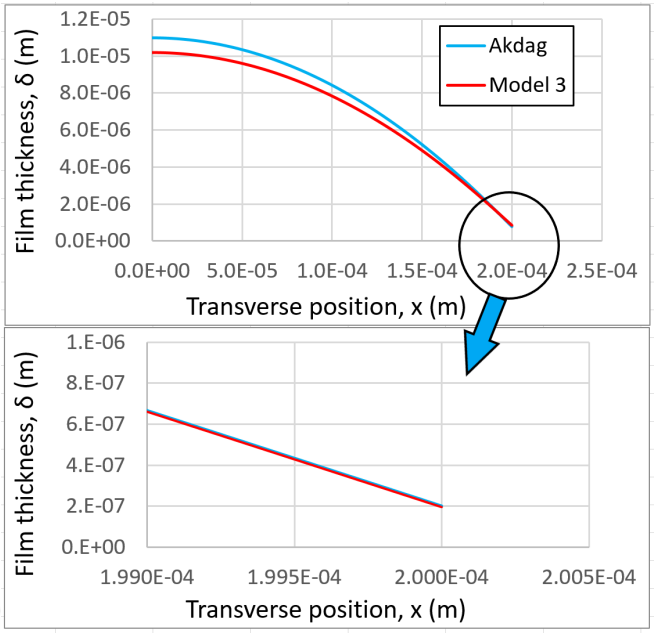


Figure 3.7: Comparison of film profile variation of Akdağ [39] with Model 3, for $\theta = 85°$ with $\Delta T = -1℃$

It can be seen that there is good agreement between the film thickness predictions of the models, but for better validation, the difference of exiting mass flow at the edge between [39] and the current models and also the difference of the exiting mass flow rate at the edge between Model 3 and other models are plotted in Fig. 3.8, Fig. 3.9 and Fig. 3.10. In Fig. 3.8, the models are solved for the edge angle of $\theta = 65°$ for the temperature differences of $\Delta T = -0.1℃$, $\Delta T = -0.3℃$, $\Delta T = -1℃$ and $\Delta T = -5℃$. Also, in Fig. 3.9 and Fig. 3.10 the same models with the same temperature differences are solved for a edge angles of $\theta = 75°$ and $\theta = 85°$. Because Model 3 have the same boundary conditions as the reference model [39], it is expected that the Model 3 has the same mass flow rate at the edge as the reference model [39]. However, it can be seen from Fig. 3.8, Fig. 3.9 and Fig. 3.10 that there is a difference between the predictions of Model 3 and the reference model [39], remain approximately constant with temperature difference. Since the solving approach is different from the reference model [39] and the current models, it's better to compare the predictions of Model 1 and Model 2 with Model 3.

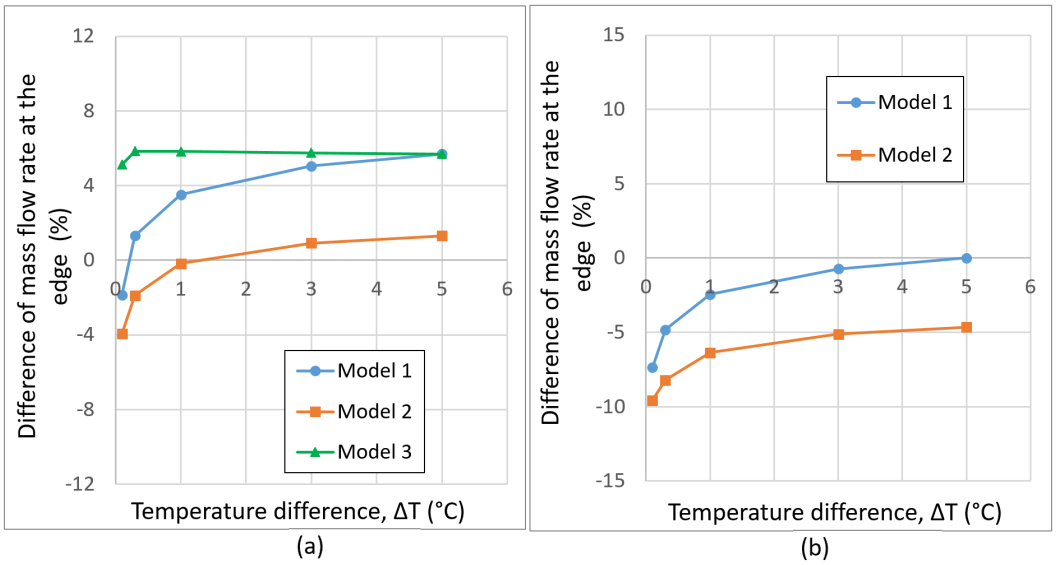


Figure 3.8: Difference of mass flow rate between (a) Akdağ [39] and the current models (b) Model 3 and the current models, for $\theta = 65°$ with $\Delta T = -0.1$℃, $\Delta T = -0.3$℃, $\Delta T = -1$℃ and $\Delta T = -5$℃

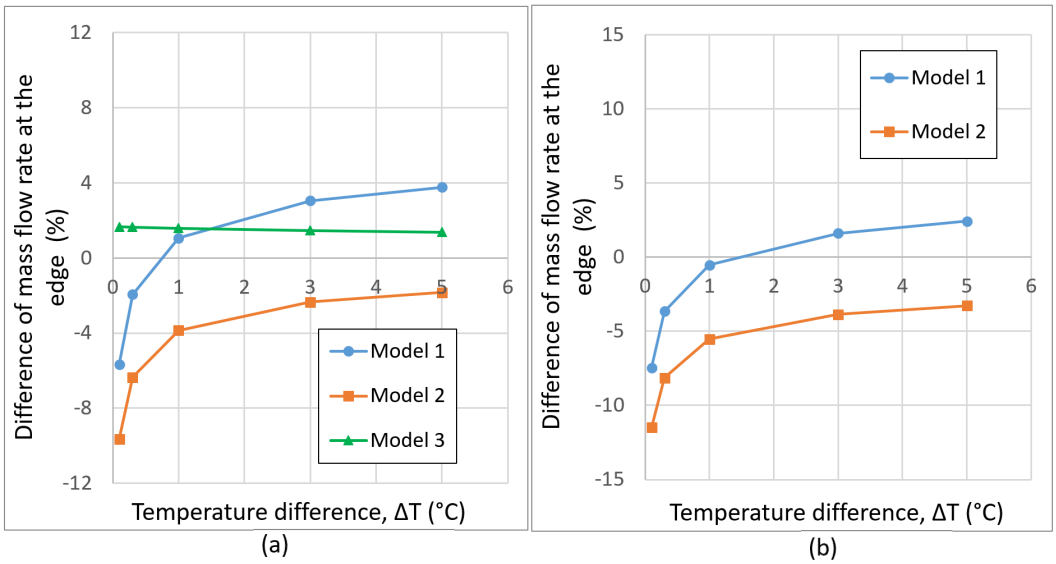


Figure 3.9: Difference of mass flow rate between (a) Akdağ [39] and the current models (b) Model 3 and the current models, for $\theta = 75°$ with $\Delta T = -0.1$℃, $\Delta T = -0.3$℃, $\Delta T = -1$℃ and $\Delta T = -5$℃

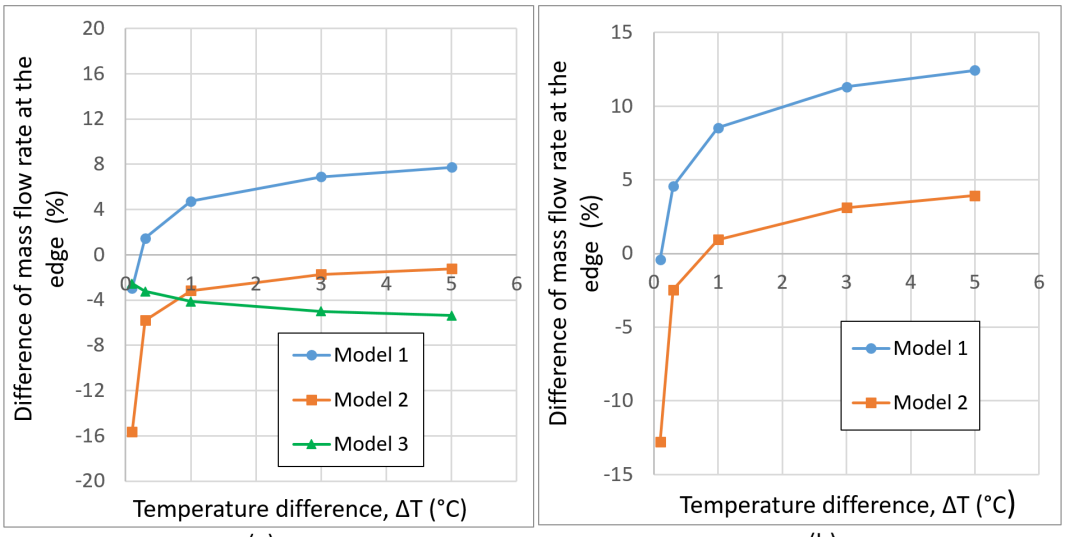


Figure 3.10: Difference of mass flow rate between (a) Akdağ [39] and the current models (b) Model 3 and the current models, for $\theta = 85°$ with $\Delta T = -0.1$℃, $\Delta T = -0.3$℃, $\Delta T = -1$℃ and $\Delta T = -5$℃

It can be seen from Fig. 3.9 and Fig. 3.10 that Model 3 matches Model 1 for the smaller edge angles and small temperature differences. However, for higher edge angles and high temperature differences, there is a good agreement between the results of Model 3 and Model 2, and it can be concluded that utilizing the second set of boundary conditions is proper. Of course, there should be more comparison between the models with different edge angles and temperature differences for a more general conclusion.

## 3.3 The effect of disjoining pressure on the predictions of groove side boundary conditions

In the models without disjoining pressure, the pressure is assumed to be generated due to the capillary effect only. The primary purpose of constructing these models is to compare and analyze the effect of disjoining pressure on the film thickness on the fin top. In addition, the effect of boundary conditions at the edge is investigated for these models. Film thickness profiles for various temperature differences between the wall and vapor at an edge angle of $\theta = 88°$ is plotted in Fig. 3.11

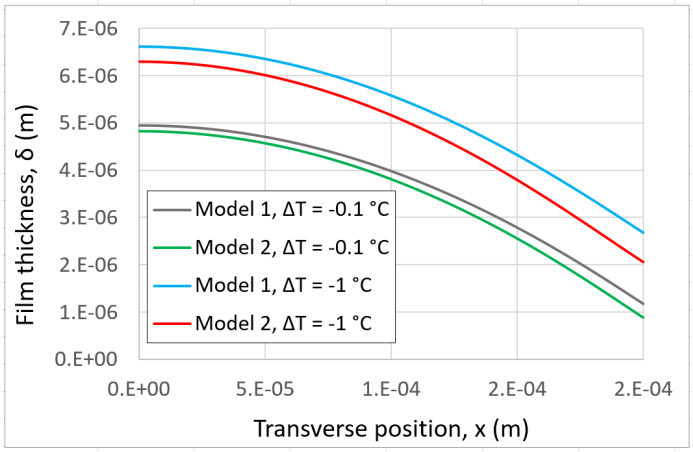


Figure 3.11: Film profiles for $\theta = 88°$ with $\Delta T = -1$℃ and $\Delta T = -0.1$℃, without disjoining pressure for Model 1 and Model 2

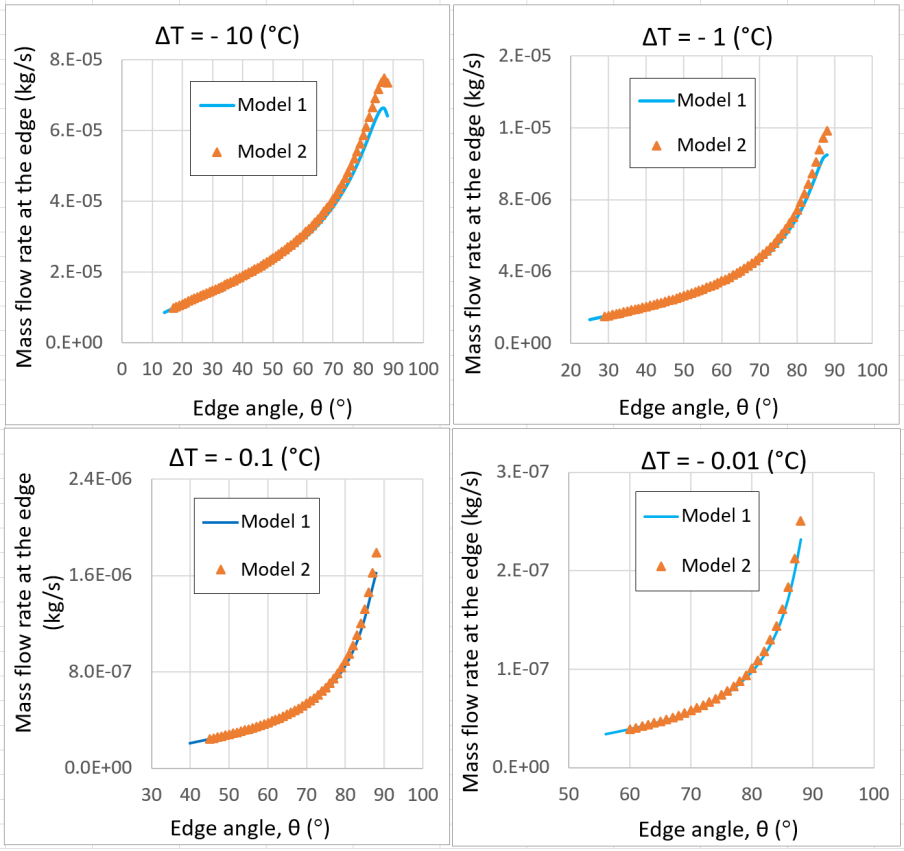


Figure 3.12: Mass flow rate exiting the fin top for various temperature differences for Model 1 and Model 2 without disjoining pressure

As the temperature difference between the wall and vapor increases, the condensation mass flux also increases, and as a result, the films become thicker. In addition, it can be seen from Fig. 3.11 that utilizing different boundary conditions changes the liquid-vapor interface profile, especially in the close proximity of groove's edge, which affects the mass flow rate leaving the fin top at the edge of the groove. Mass flow at the edge for different edge angles and various temperature differences is plotted in Fig. 3.12. By comparing Model 1 and Model 2 in Fig. 3.12, it can be concluded that the predicted mass flow rate will increase if second set of boundary conditions are used. This increase is due to reduction in the profile thickness. The effect of disjoining pressure is negligible for thicker and flatter film profiles observed in higher temperature differences and higher edge angles. Still, the impact of disjoining pressure is dominant in the small zone near the edge for the thinner and more curvy film shapes. Generally, the most realistic models are the ones that have been solved including the effect of disjoining pressure.

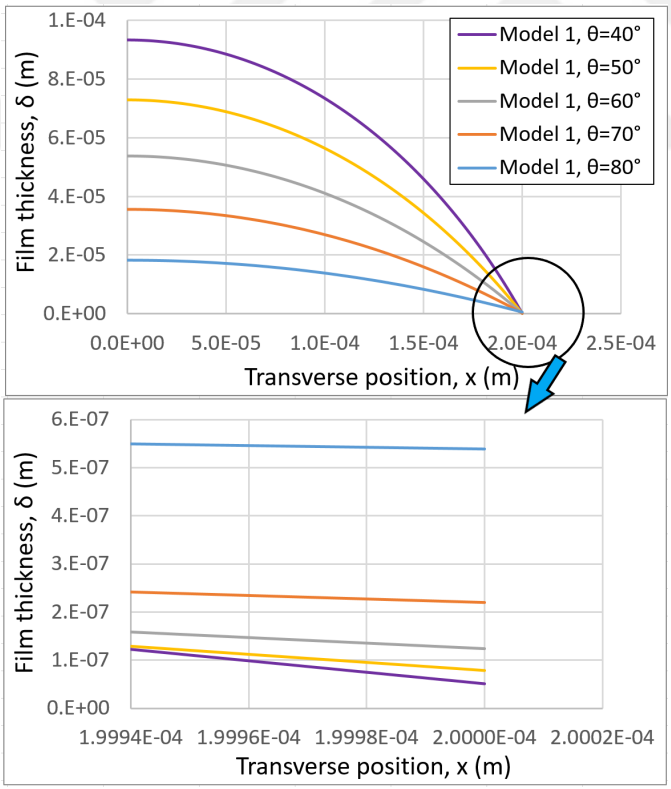


Figure 3.13: Variation of Model 1 film profiles for $\Delta T = -1$℃ for $\theta = 80°$ , $\theta = 70°$, $\theta = 60°$, $\theta = 50°$ and $\theta = 40°$ edge angles, including the effect of disjoining pressure

Variation of film thickness for different edge angles with $\Delta T = -1$℃ are plotted in Fig. 3.13. As it can be seen from Fig. 3.13, film profile flattens by increasing the edge angle.

Also, film profiles for the edge angles of $\theta = 40°$ and $\theta = 80°$ with temperature difference of $\Delta T = -1$℃ are plotted using different sets of boundary conditions at the edge of fin in Fig. 3.14. From Fig. 3.14, it can be understood that utilizing the second set of boundary conditions results in thinner films, and this effect gets more prominent as the edge angle increases.

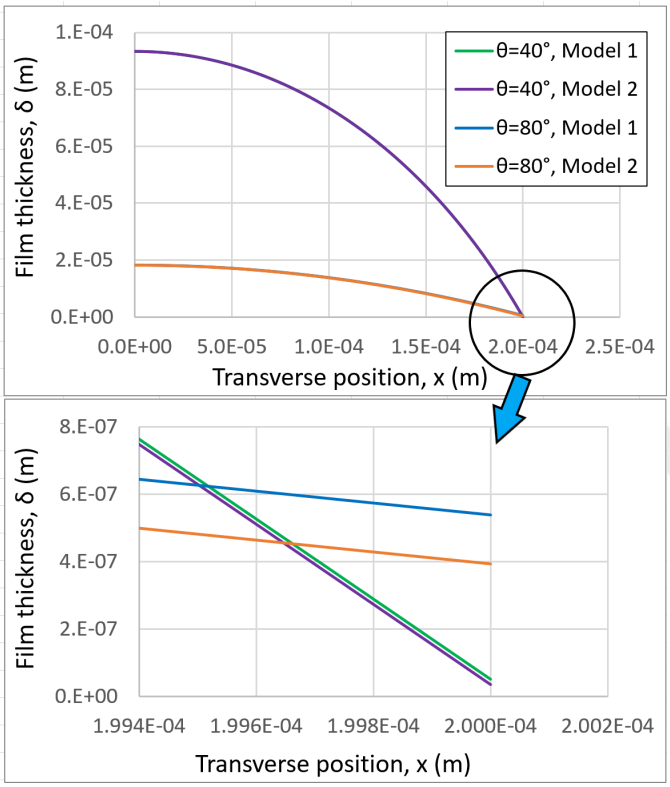


Figure 3.14: Comparison of film profiles of Model 1 and Model 2 for $\Delta T = -1$℃ for $\theta = 80°$ and $\theta = 40°$ edge angles, including the effect of disjoining pressure

Variation of mass flow rate along the lateral $(x)$ direction at $\theta = 70°$ are plotted for various temperature differences and sets of boundary conditions in Fig. 3.15. it can be seen that utilizing higher temperature differences and the second set of boundary conditions at the edge of the groove results in an increased mass flow rate exiting the fin edge.

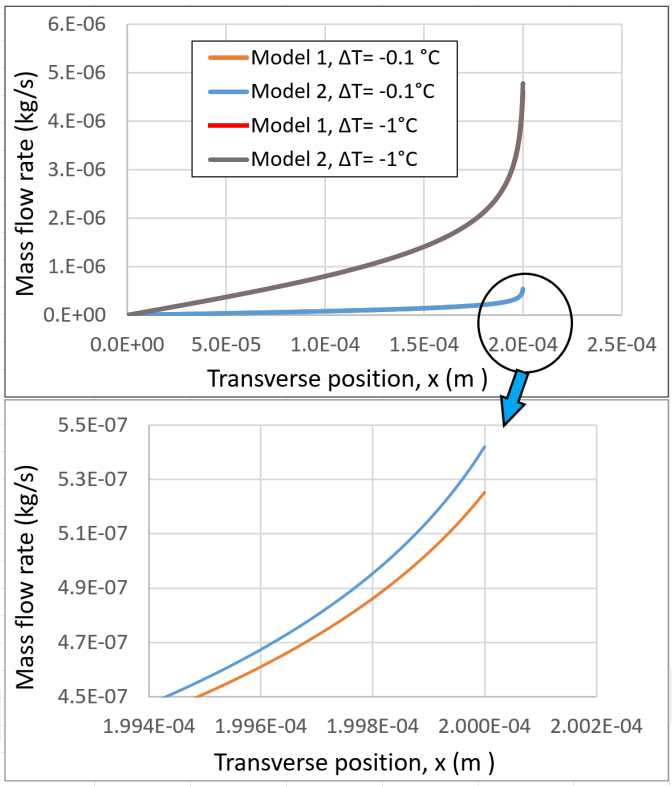


Figure 3.15: Variation of mass flow rate along $x$ direction with $\Delta T = -1$℃ and $\Delta T = -0.1$℃ and with $\theta = 70°$ edge angle for Model 1 and Model 2

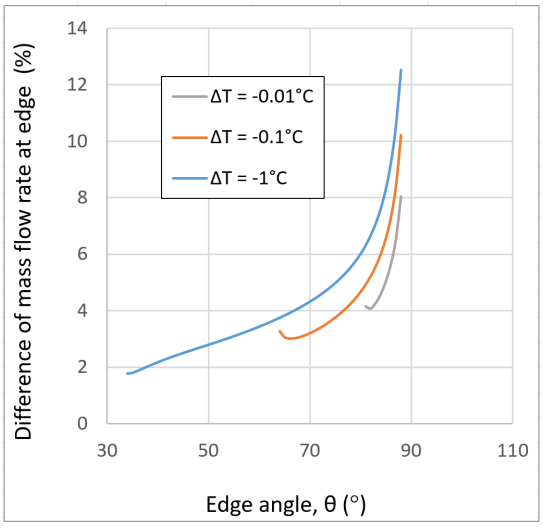


Figure 3.16: Percentage mass flow rate difference between Model 1 and Model 2 for various edge angles $\theta$ and temperature differences $\Delta T$

The second set of boundary conditions predict an increased mass flow rate entering the groove. To investigate it in detail, the difference in percentage of mass flow rate at the fin edge between models can give a better understating of this change. For this purpose, the difference of mass flow rate exiting the fin between Model 1 and Model 2 is plotted in Fig. 3.16 for different edge angles and temperature differences. It can be seen from Fig. 3.16 that the maximum difference of mass flow rate entering the groove between Model 1 and Model 2 occurs at the edge angle of $\theta = 88°$ with temperature difference of $\Delta T = -1$. Therefore, it can be concluded that this difference is significant for flatter film profiles with high temperature differences.

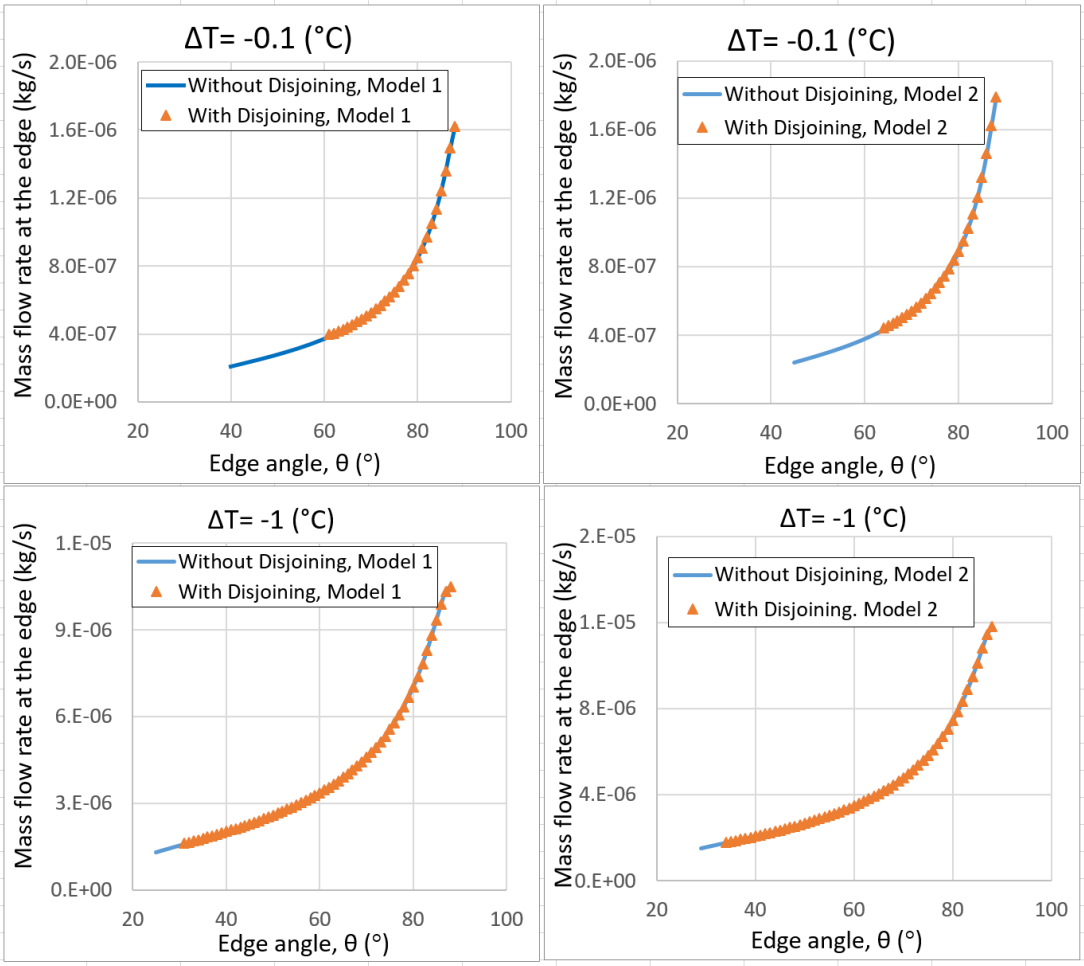


Figure 3.17: Relative change of mass exiting the fin top and range of edge angle till the cut off point for different models with $\Delta T = -0.1$℃ and $\Delta T = -1$℃ and for different edge angles

The magnitude of disjoining pressure is inversely proportional to $\delta^3$, and as the film gets thinner, the effect of disjoining pressure becomes non-negligible and even dominant. The dominant effect which disjoining pressure has on modeling is that results can be calculated until a specific value of edge angle and temperature difference. Beyond that particular point, due to the physical limitation which will be investigated in the following, the solver cannot converge to a solution. This specified point will be called the "cut-off point".

It turns out that utilizing the second set of boundary conditions alters the location of the cut-off point. In Fig. 3.17, the mass flow rate at the edge is found for different edge angles and temperature differences. As it is seen from the figure, there is a limited solution range for a specified temperature difference, and beyond the special edge angle, the solution cannot be found. For instance, by assuming $\Delta T = -1℃$, in Model 2 without disjoining pressure, results can be obtained from $\theta = 88°$ to $\theta = 29°$. However, when the disjoining pressure is taken into account, the solution range for the same model changes to $\theta = 88°$ until $\theta = 34°$. By using the first set of boundary conditions (Model 1), this solution range alters to $\theta = 88°$ until $\theta = 31°$. After this edge angle, the physical limitation appears. The film gets extremely thin, and the contribution of the disjoining pressure term on the mass flow rate becomes orders of magnitude larger. On the other hand, the contribution of capillary pressure term on the mass flow rate changes sign and becomes negative.

The contribution of capillary and disjoining pressure on the mass flow rate for Model 2 with $\Delta T = -1℃$ for different edge angles is plotted in Fig. 3.18, where $\theta = 34°$ is the cut-off point, and below that a solution does not exist. To remind the capillary and disjoining pressure terms in the mass flow rate, Eq. (3.4) is presented as follows:

$$\dot{m}' = \frac{1}{3\nu}\,\delta^3 \left[ \underbrace{\frac{\sigma\,\delta'''}{\left(1+(\delta')^2\right)^{\frac{3}{2}}} - \frac{3\,\sigma\,\delta'\,(\delta'')^2}{\left(1+(\delta')^2\right)^{\frac{5}{2}}}}_{\text{Capillary term}} - \underbrace{\frac{3\,A_d\,\delta'}{\delta^4}}_{\text{Disjoining term}} \right] \tag{3.4}$$

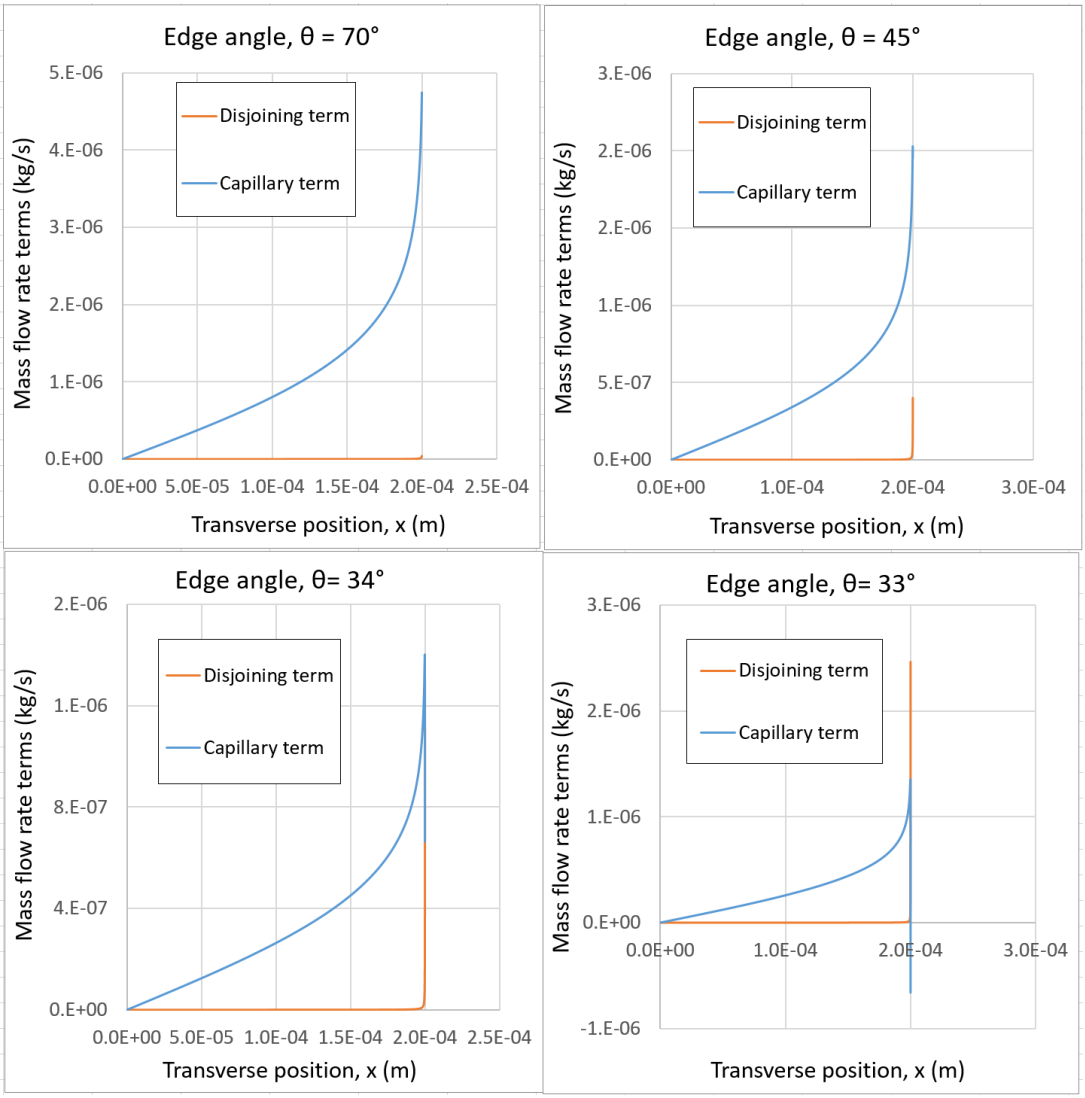


Figure 3.18: Contribution of capillary and disjoining pressure terms to the mass flow rate for Model 2, with $\Delta T = -1$℃, for $\theta = 70°$, $\theta = 45°$, $\theta = 34°$ (Cut-off point), and $\theta = 33°$

It can be seen from Fig. 3.18 for higher edge angles, the contribution of capillary pressure term to the mass flow rate is more dominant and significant in comparison with the contribution of disjoining pressure. However, by approaching the cut-off point, the contribution of disjoining pressure term to the mass flow rate substantially increases, and the contribution of the capillary pressure term suddenly drops and even becomes negative. After the cut-off point, due to the physical limitation, a solution cannot be obtained. The main reason for this limitation is that the third derivative of $\delta$

with respect to $x$ is discontinuous and approaches infinity at the edge, which is shown in Fig. 3.19.

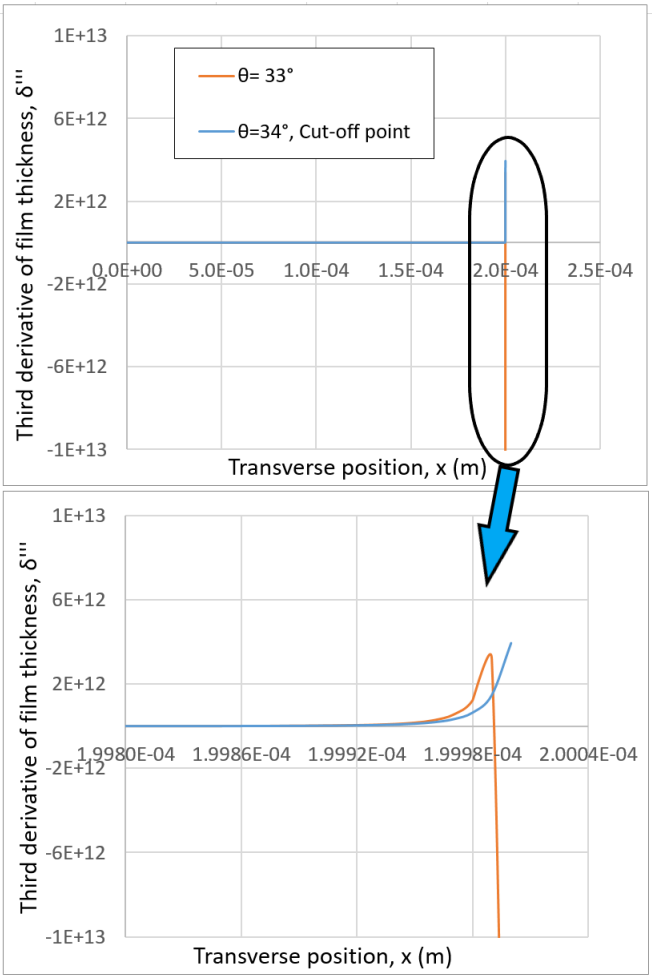


Figure 3.19: The third derivative of film thickness with respect to $x$ along the lateral direction for Model 2, with $\Delta T = -1$℃, for $\theta = 34°$ (Cut-off point) and $\theta = 33°$

The second derivative of film thickness along the lateral direction $(x)$ is calculated for Model 1 and Model 2 for edge angles of $\theta = 85°$ and $\theta = 65°$ with the temperature difference of $\Delta T = -0.1$℃. As shown in Fig. 3.20, the inflection point of the film profile for Model 2 comes closer to the fin edge by decreasing the edge angle and an abrupt change in the second derivative of film thickness can be observed near the edge.

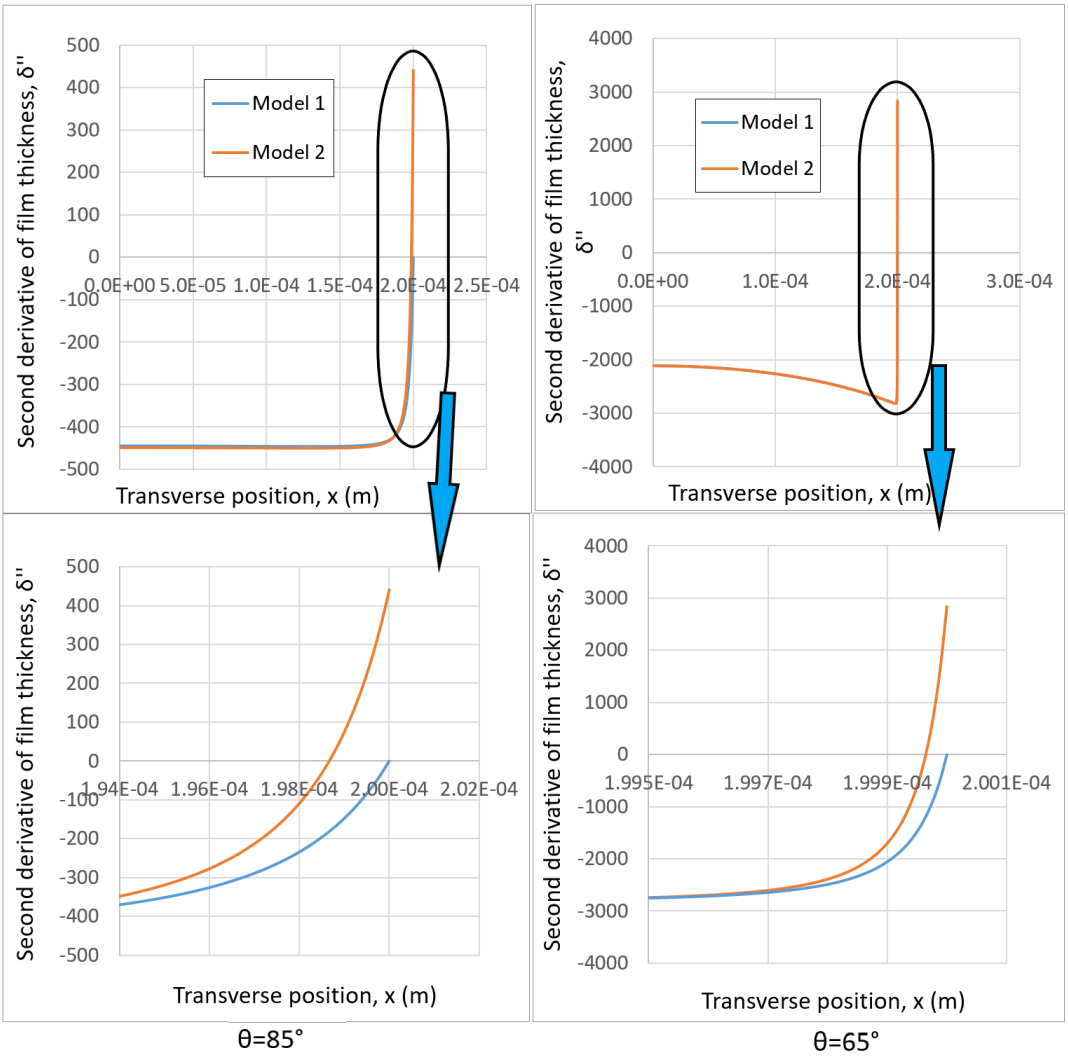


Figure 3.20: Comparison of second derivative of film thickness with respect to $x$ along lateral direction at the edge angles of $\theta = 85°$ and $\theta = 65°$ with temperature difference $\Delta T = -0.1℃$

# CHAPTER 4

# TWO DIMENSIONAL FLOW ON THE FIN TOP

In all of the models in the literature, the flow on the fin top of the condensation region is assumed to be one-dimensional in the lateral direction. Although the change of radius of curvature of film profile in the axial direction is not significant compared to the lateral direction, the axial flow can still affect the film profile. In this chapter, a novel numerical approach based on finite difference method is developed to explore the axial flow. At first the mentioned numerical process is applied to one-dimensional flow on the fin top to ensure that it works properly. Then a two-dimensional flow model on the fin top is proposed, and, preliminary findings are discussed.

## 4.1 Governing equations for two-dimensional flow modeling

The governing equations is obtained by writing a balance between pressure and shear effects in both directions in conjunction with conservation of mass. As mentioned in Chapter 2, by assuming lubrication theory, the $x$-momentum and $y$-momentum equations can be simplified as follows:

$$\frac{\partial P_l}{\partial x} = \mu \frac{d^2 u}{dz^2} \tag{4.1a}$$

$$\frac{\partial P_l}{\partial y} = \mu \frac{d^2 v}{dz^2} \tag{4.1b}$$

In Eq. (4.1), $u$,$v$ are the fluid velocities in the lateral and axial directions respectively.

$$\text{At} \qquad z = 0: \qquad u = 0 \qquad \text{and} \qquad v = 0 \tag{4.2a}$$

$$\text{At} \qquad z = \delta: \qquad \frac{du}{dz} = 0 \qquad \text{and} \qquad \frac{dv}{dz} = 0 \tag{4.2b}$$

Assuming the zero shear stress at the free surface and no-slip boundary conditions that given in Eq. (4.2), Eq. (4.1) can be integrated, which gives the velocity distribution.

$$u(z) = \frac{1}{2\mu} \frac{\partial P_l}{\partial x} z(z - 2\delta) \tag{4.3a}$$

$$v(z) = \frac{1}{2\mu} \frac{\partial P_l}{\partial y} z(z - 2\delta) \tag{4.3b}$$

By integrating the velocity profiles, the mass flow rate per unit depth in both $x$-direction and $y$-direction can be calculated:

$$\dot{m}'_x = \rho \int_0^\delta u \, dz = -\frac{1}{3\nu} \frac{\partial P_l}{\partial x} \delta^3 \tag{4.4a}$$

$$\dot{m}'_y = \rho \int_0^\delta v \, dz = -\frac{1}{3\nu} \frac{\partial P_l}{\partial y} \delta^3 \tag{4.4b}$$

By utilizing the Young-Laplace equation, and the definition of capillary pressure and disjoining pressure, explained in Chapter 3, the liquid pressure can be written as follows:

$$P_v - P_l = P_c + P_d = \left[ \frac{\sigma \, \delta_{xx}}{\left(1 + (\delta_x)^2\right)^{\frac{3}{2}}} + \frac{\sigma \, \delta_{yy}}{\left(1 + (\delta_y)^2\right)^{\frac{3}{2}}} \right] + \frac{A_d}{\delta^3} \tag{4.5}$$

Since the two-dimensional model will be solved for high edge angles, the denominator part of capillary pressure can be neglected for simplicity. Moreover, because the effect of disjoining pressure appears for low edge angles, the disjoining pressure term

can be eliminated for two-dimensional model. By assuming a constant vapor pressure, the partial derivatives of liquid pressure with respect to $x$ and $y$ can be obtained:

$$\frac{\partial P_l}{\partial x} = -\frac{\partial P_c}{\partial x} = -\sigma\Big(\delta_{xxx} + \delta_{xyy}\Big) \tag{4.6a}$$

$$\frac{\partial P_l}{\partial y} = -\frac{\partial P_c}{\partial y} = -\sigma\Big(\delta_{yyy} + \delta_{yxx}\Big) \tag{4.6b}$$

By substituting Eq. (4.6) in Eq. (4.4), mass flow rate in both directions can be calculated:

$$\dot{m}'_x = \frac{\sigma\,\delta^3}{3\nu}\,\Big(\delta_{xxx} + \delta_{xyy}\Big) \tag{4.7a}$$

$$\dot{m}'_y = \frac{\sigma\,\delta^3}{3\nu}\,\Big(\delta_{yyy} + \delta_{yxx}\Big) \tag{4.7b}$$

Mass balance on the fin top is affected by condensation which gives:

$$\frac{\partial \dot{m}'_x}{\partial x} + \frac{\partial \dot{m}'_y}{\partial y} = -\dot{m}'_c \tag{4.8}$$

Using Eq. (2.10) and Eq. (4.7), the above equation arranged to give:

$$\begin{aligned}\frac{\sigma}{3\nu}\left\{\frac{\partial}{\partial x}\left[\delta^3\left(\delta_{xxx} + \delta_{xyy}\right)\right] + \frac{\partial}{\partial y}\left[\delta^3\left(\delta_{yyy} + \delta_{yxx}\right)\right]\right\} \\ = -\frac{a\,(T_w - T_v) - b\,(P_c + P_d)}{1 + a\,\delta\,h_{lv}/k_l}\end{aligned} \tag{4.9}$$

By taking the derivatives in Eq. (4.9), the governing equation can be found as follows:

$$\begin{aligned}\delta_{xxxx} = &-\delta_{yyyy} - \frac{3\,\delta_x\,\delta_{xxx}}{\delta} - \frac{3\,\delta_y\,\delta_{yyy}}{\delta} - \frac{3\,\delta_x\,\delta_{xyy}}{\delta} - \frac{3\,\delta_y\,\delta_{yxx}}{\delta} \\ &- 2\,\delta_{xxyy} - \frac{3\,\nu}{\sigma\,\delta^3}\left[\frac{a\,(T_w - T_v) - b\,(P_c + P_d)}{1 + a\,\delta\,h_{lv}/k_l}\right]\end{aligned} \tag{4.10}$$

This is a $4^{th}$ order PDE in both transverse $(x)$ and axial $(y)$ directions.

## 4.2 Finite difference (FD) method for one-dimensional model

The governing equation for one dimensional flow model was obtained in Chapter 2 as follows:

$$\begin{aligned}\delta'''' = &-\frac{3\,\delta'\delta'''}{\delta} + \frac{3\,(\delta'')^3}{\left(1+(\delta')^2\right)} + \frac{9\,(\delta')^2\,(\delta'')^2}{\left(1+(\delta')^2\right)\delta} - \frac{15\,(\delta')^2\,(\delta'')^3}{\left(1+(\delta')^2\right)^2} \\ &+ \frac{9\,\delta'\,\delta''\,\delta'''}{\left(1+(\delta')^2\right)} - \frac{3\nu\left(1+(\delta')^2\right)^{\frac{3}{2}}}{\sigma\,\delta^3}\left[\frac{a\,(T_w-T_v)-b\,(P_c+P_d)}{1+a\delta h_{lv}/k_l}\right] \\ &+ \frac{3\,A_d}{\sigma}\left(1+(\delta')^2\right)^{\frac{3}{2}}\left[\frac{\delta''}{\delta^4} - \frac{(\delta')^2}{\delta^5}\right]\end{aligned} \tag{4.11}$$

This is also the same equation as Eq. (4.10) when the axial variation is omitted. Another way to solve this one-dimensional governing $4^{th}$ order nonlinear differential equation is to utilize the finite difference method along with an iterative method based on successive substitution. This approach will be further applied to the two-dimensional problem presented in this chapter. In the solution domain, the interval of $[0, L]$ is divided into $N$ equal sub-intervals $(0 \leq i \leq N)$, and the derivatives in each node will be written using finite difference formulae. Central difference formulae of the order $\mathcal{O}(h^2)$ are used, which can be written as:

$$\delta'_i = \frac{\delta_{i+1} - \delta_{i-1}}{2\,\Delta x}$$

$$\delta''_i = \frac{\delta_{i+1} - 2\,\delta_i + \delta_{i-1}}{\Delta x^2}$$

$$\delta'''_i = \frac{\delta_{i+2} - 2\,\delta_{i+1} + 2\,\delta_{i-1} - \delta_{i-2}}{2\,\Delta x^3} \tag{4.12}$$

$$\delta''''_i = \frac{\delta_{i+2} - 4\,\delta_{i+1} + 6\,\delta_i - 4\,\delta_{i-1} + \delta_{i-2}}{\Delta x^4}$$

For the internal nodes, all the above formulae are applied, but in the boundary nodes, the effect of boundary conditions should be reflected on the finite different formulae, therefore, formulae appropriate for the specified boundary conditions should be derived.

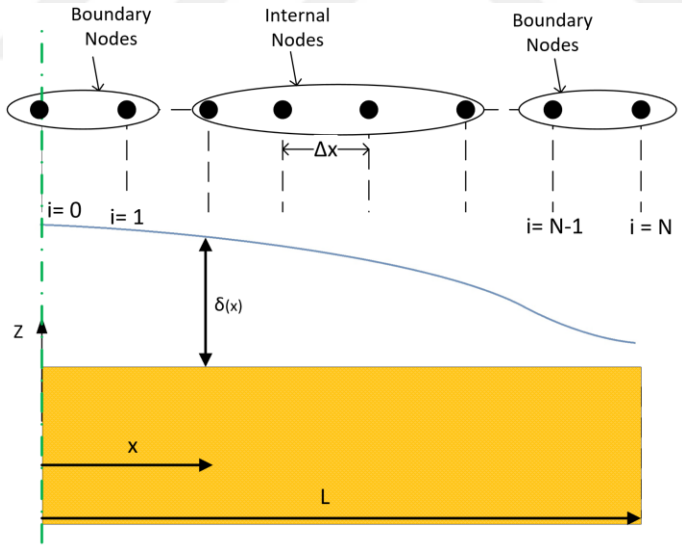


Figure 4.1: Nodes in the finite difference method

On the line of symmetry $\delta'$ and $\delta'''$ are equal to zero and by assuming ghost-cells, central difference formulae for $\delta''''$ and $\delta'''$ in the boundary nodes can be present as:

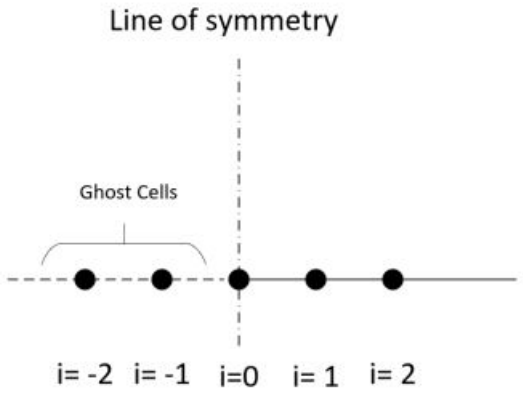


Figure 4.2: Ghost-cells

$$\begin{aligned} &\text{At} \quad i = 0 \quad ; \quad \frac{d\delta}{dx} = 0 \quad \rightarrow \quad \delta_{-1} = \delta_1 \\ &\text{At} \quad i = 0 \quad ; \quad \frac{d^3\delta}{dx^3} = 0 \quad \rightarrow \quad \delta_{-2} = \delta_2 \end{aligned} \tag{4.13}$$

$$\begin{aligned} \delta_0'''' &= \frac{2\,\delta_2 - 8\,\delta_1 + 6\,\delta_0}{\Delta x^4} \\ \delta_1'''' &= \frac{\delta_3 - 4\,\delta_2 + 7\,\delta_1 - 4\,\delta_0}{\Delta x^4} \\ \delta_1''' &= \frac{\delta_3 - 2\,\delta_2 + 2\,\delta_0 - \delta_1}{2\,\Delta x^3} \end{aligned} \tag{4.14}$$

The derivatives cannot be precisely calculated using backward or forward difference formulae for $\delta'''$ and $\delta''''$ at the boundary nodes. For getting accurate derivatives at the fin edge, the effect of boundary conditions should be implemented in the formulae, and for this purpose, a novel approach is developed. New formulae in the boundary nodes are developed from a series of Taylor series expansions, which are derived and discussed in details in Appendix A. The resulting finite different formulae are:

$$
\begin{aligned}
\delta''''_{N-1} &= \frac{-113\,\delta_N + 192\,\delta_{N-1} - 108\,\delta_{N-2} + 32\,\delta_{N-3} - 4\,\delta_{N-4} + 60\,\delta'_N\,\Delta x}{12\,\Delta x^4} \\
\delta'''_{N-1} &= \frac{-39\,\delta_N + 48\,\delta_{N-1} - 9\delta_{N-2} + 30\,\delta'_N\,\Delta x - 6\,\delta''_N\,\Delta x^2}{4\,\Delta x^3} \\
\delta''''_N &= \frac{148\,\delta_N - 180\,\delta_{N-1} + 36\,\delta_{N-2} - 4\,\delta_{N-3} - 120\,\delta'_N\,\Delta x + 36\,\delta''_N\,\Delta x^2}{3\,\Delta x^4} \\
\delta'''_N &= \frac{45\,\delta_N - 48\,\delta_{N-1} + 3\,\delta_{N-2} - 42\,\delta'_N\,\Delta x + 18\,\delta''_N\,\Delta x^2}{4\,\Delta x^3}
\end{aligned}
\tag{4.15}
$$

Since the governing differential equation is nonlinear, an iterative method based on successive substitution is used to handle this issue. After taking care of nonlinearity, the finite difference method can be applied. To do this, the nonlinear terms are iteratively lagged and appear in the forcing function. Eq. (4.11) takes the following form:

$$
\begin{aligned}
{}_{k+1}\delta'''' = &- \frac{3\ {}_k\delta'\ {}_k\delta'''}{{}_k\delta} + \frac{3\ {}_k(\delta'')^3}{(1+{}_k(\delta')^2)} + \frac{9\ {}_k(\delta')^2\ {}_k(\delta'')^2}{(1+{}_k(\delta')^2)\ {}_k\delta} - \frac{15\ {}_k(\delta')^2\ {}_k(\delta'')^3}{(1+{}_k(\delta')^2)^2} \\
&+ \frac{9\ {}_k\delta'\ {}_k\delta''\ {}_k\delta'''}{(1+{}_k(\delta')^2)} - \frac{3\nu\,(1+{}_k(\delta')^2)^{\frac{3}{2}}}{\sigma\ {}_k\delta^3}\left[\frac{a\,(T_w - T_v) - b\,(P_c + P_d)}{1 + a\ {}_k\delta\,h_{lv}/k_l}\right] \\
&+ \frac{3\,A_d}{\sigma}\left(1+{}_k(\delta')^2\right)^{\frac{3}{2}}\left[\frac{{}_k\delta''}{{}_k\delta^4} - \frac{{}_k(\delta')^2}{{}_k\delta^5}\right]
\end{aligned}
\tag{4.16}
$$

where the subscript "k" denotes the iterative step.

An approximation for the initial film profile has to be used to initiate the iterative process, and based on that, derivatives and forcing functions on the right-hand side of the equation can be calculated. The resulting equation is linear and can be solved with

a proper linear equation solver. In the current modeling, Gauss elimination method is used to solve the resulting set of linear equations. The form of the linearized equation is:

$$\mathbf{A} \cdot \delta = \mathbf{b} \tag{4.17}$$

where **A** and **b** are the coefficient matrix and the forcing vector, respectively. The coefficient matrix is a sparse matrix, and it increases the CPU time to solve the system.

In the interval of $(0 \leq i \leq N)$, the coefficient matrix becomes ill-conditioned, resulting in an unprecise solution. Generally, a matrix is ill-conditioned when the calculation of its inverse or solution of the linear system has potential significant numerical errors. In other words, a slight change in the coefficient matrix can lead to a considerable change in the value of the inverse matrix or solution. One way of distinguishing the ill-conditioning for a matrix is given by Hornbeck [40]. A matrix is considered as ill-conditioned if :

$$\frac{\det C}{\sqrt{\sum_{i=0}^{n}\sum_{j=0}^{n} C_{i,j}^2}} \ll 1 \tag{4.18}$$

where $\sqrt{\sum_{i=0}^{n}\sum_{j=0}^{n} C_{i,j}^2}$ is the Euclidean norm. To solve this problem and turn the coefficient matrix into a well-conditioned matrix, we assume the solution domain in the interval of $(1 \leq i \leq N)$. Then for solving the film thickness profile at $i = 0$ (symmetry line), $\delta_0$ should be found in a way that it satisfies the boundary condition in the symmetry line $\delta_0''' = 0$. This shooting procedure is implemented in conjunction with secant method.

After solving the linear set of equations, the new values of $\delta$ will be compared with the old values. Until the satisfaction of relative convergence criteria, the new values $(k+1)$ should be replaced with the old ones $(k)$. The initial guesses come from the solution of the RK4 method for the one-dimensional problem, which is described in Section 2.5.5. Due to the presence of highly nonlinear terms in current problem, to stabilize the model, damping (under-relaxation) should be applied. In other words, $\delta$ should be updated in this form:

$$\delta_{new} = (1 - \lambda)\,\delta_{old} + \lambda\delta_{new} \tag{4.19}$$

where $\lambda$ is the damping value and can vary in the range of $[0, 1]$, depending on the stiffness of the problem.

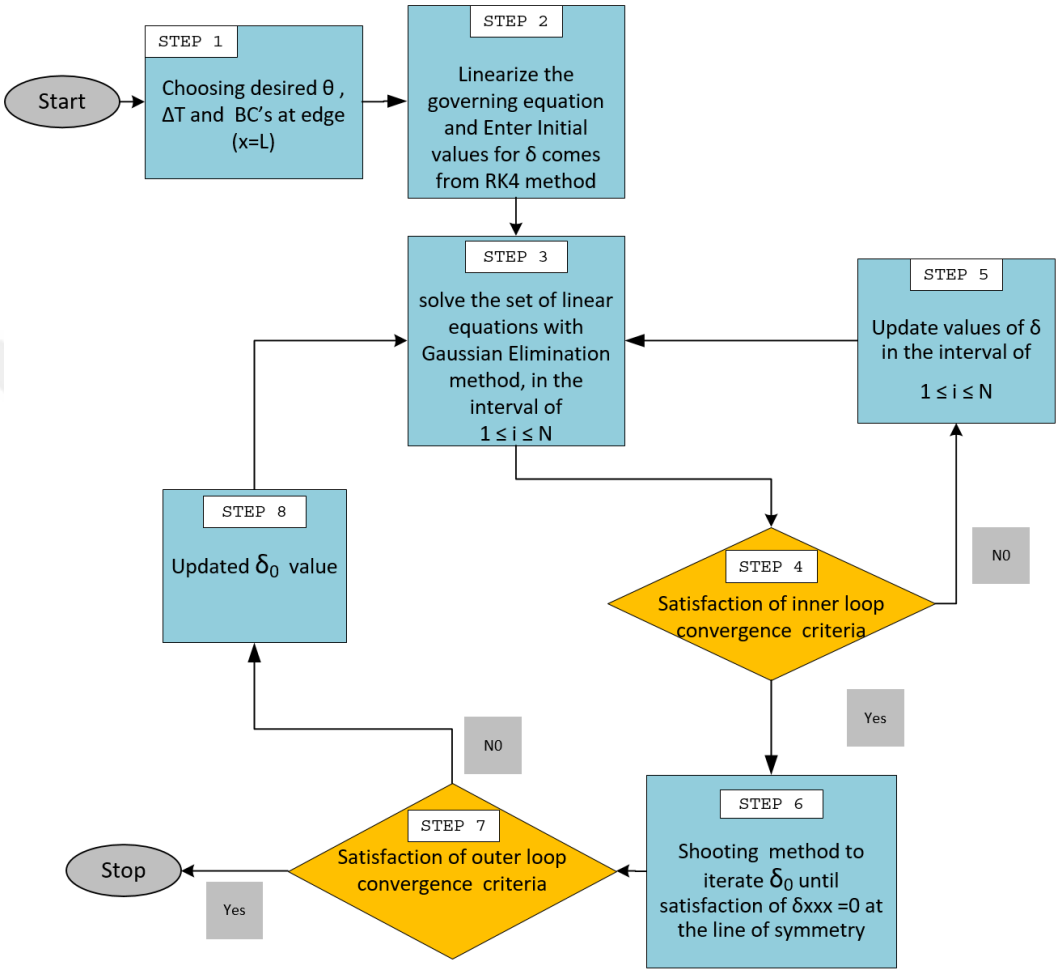


Figure 4.3: Flowchart of FD method

As can be seen from the flowchart in Fig. 4.3, there are two loops in the procedure, the inner loop and the outer loop. In the inner loop, a system of linear equations in the interval of $(1 \leq i \leq N)$ should converge to criteria value. The relative convergence criteria for the inner loop is assumed to be $10^{-12}$ in current modeling. After convergence, in the outer loop, the value of film thickness at the line of symmetry should satisfy the $\delta_0''' = 0$ with a shooting method in conjunction with secant method, otherwise utilizing updated $\delta$ at $i = 0$, the first loop has to be iterated again, until

the satisfaction of convergence criteria of the outer loop. The relative convergence criteria for the outer loop is $10^{-8}$. It has to be mentioned that the inner loop has to converge with a higher precision than the outer loop.

## 4.3 Validation of one-dimensional FD formulation with RK4 method

Since the accuracy of the FD method is lower than the RK method, the solution range for the FD method will be limited, but FD method can be applied to solve the two-dimensional flow model. For higher edge angles with greater temperate differences, this restriction cannot significantly affect the solution domain, but for lower edge angles and small temperature differences, due to the considerable variation in film profile and their corresponding higher derivatives, it will be difficult for the FD method to capture a proper solution. Because of this limitation, adding or neglecting the disjoining pressure will not make a substantial difference in the solution. In this section, the solution for various slopes and temperature differences is found, and the effect of the number of nodes is investigated in Section 4.3.1. Moreover, by comparing the results with the RK4 method, the validity of this method can be explored.

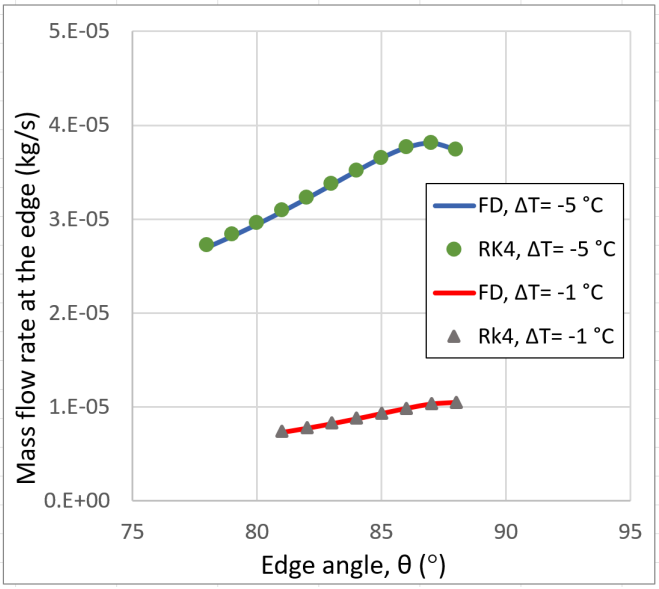


Figure 4.4: Mass flow rate comparison between RK4 and FD method, for various edge angles $\theta$ and temperature differences $\Delta T$

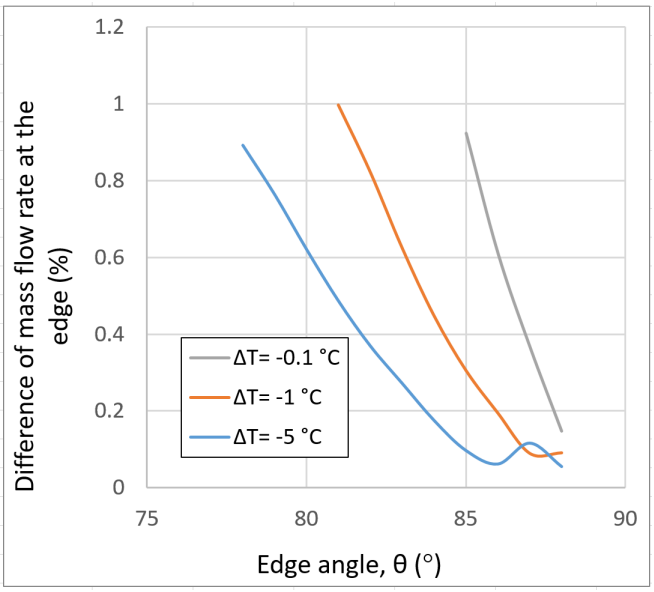


Figure 4.5: Mass flow rate difference in percentage between RK4 and FD method, for various edge angles $\theta$ and temperature differences $\Delta T$

The number of nodes along the fin top for the FD method is taken as $500$, and the first set of boundary conditions is used for validation. Fig. 4.4 shows mass flow rate entering the groove along the axial direction for both methods with different temperature differences. It can be seen that the FD method can approximately capture the same solution as the RK4 method for a particular range of edge angles. Since the values are so close to each other, it's better to plot the mass flow rate difference in percentage. This difference can be seen in Fig. 4.5.

As it can be seen from Fig. 4.4, each temperature difference has its own limited solution range. For instance, for $\Delta T = -5$℃, the FD method cannot find valid solution for the edge angles lower than $\theta = 78°$. This limitation comes from the mesh size, which makes it difficult for the FD solver to calculate the derivatives more precisely, and it results in capturing an incorrect solution. Fig. 4.6 shows this limitation for $\theta = 77°$, and it turns out that the mass flow rate decrease near the edge, which violates the mass balance.

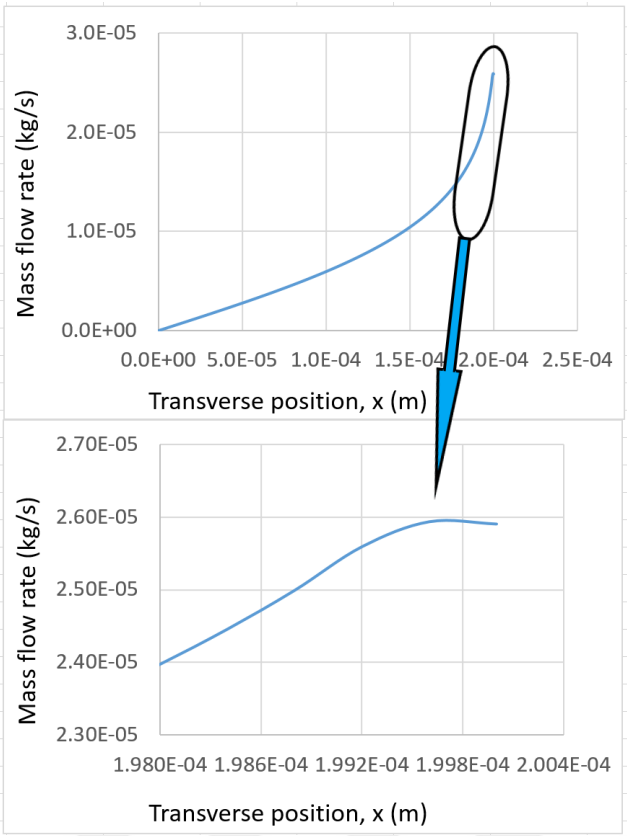


Figure 4.6: Mass flow rate along the fin solved by the FD method for $\theta = 77°$, $\Delta T = -5℃$ and utilizing first set of boundary conditions

### 4.3.1 Mesh sensitivity of one-dimensional FD formulation

In order to find the effect of mesh size on the accuracy of FD method, the mass flow rate at the edge is calculated for the Model 1 with two different numbers of nodes for various temperature differences, and the numerical results are compared with the RK4 method, which has the higher accuracy in comparison with FD method. It can be seen from the Fig. 4.7 that the model with $500$ nodes is able to find the proper solution for a wider range of edge angles. For instance, the model with $100$ number of nodes and $\Delta T = -1℃$, can obtain the valid solution from $\theta = 88°$ to $\theta = 84°$. However, the model with $500$ nodes and the same temperature difference can find the correct solution from $\theta = 88°$ to $\theta = 81°$. Moreover, it has to be mentioned that by assuming a large number of nodes in the FD method, the problem can be solved for a broader range of edge angles, but on the other hand, increasing the number of nodes

results in an enormous CPU time.

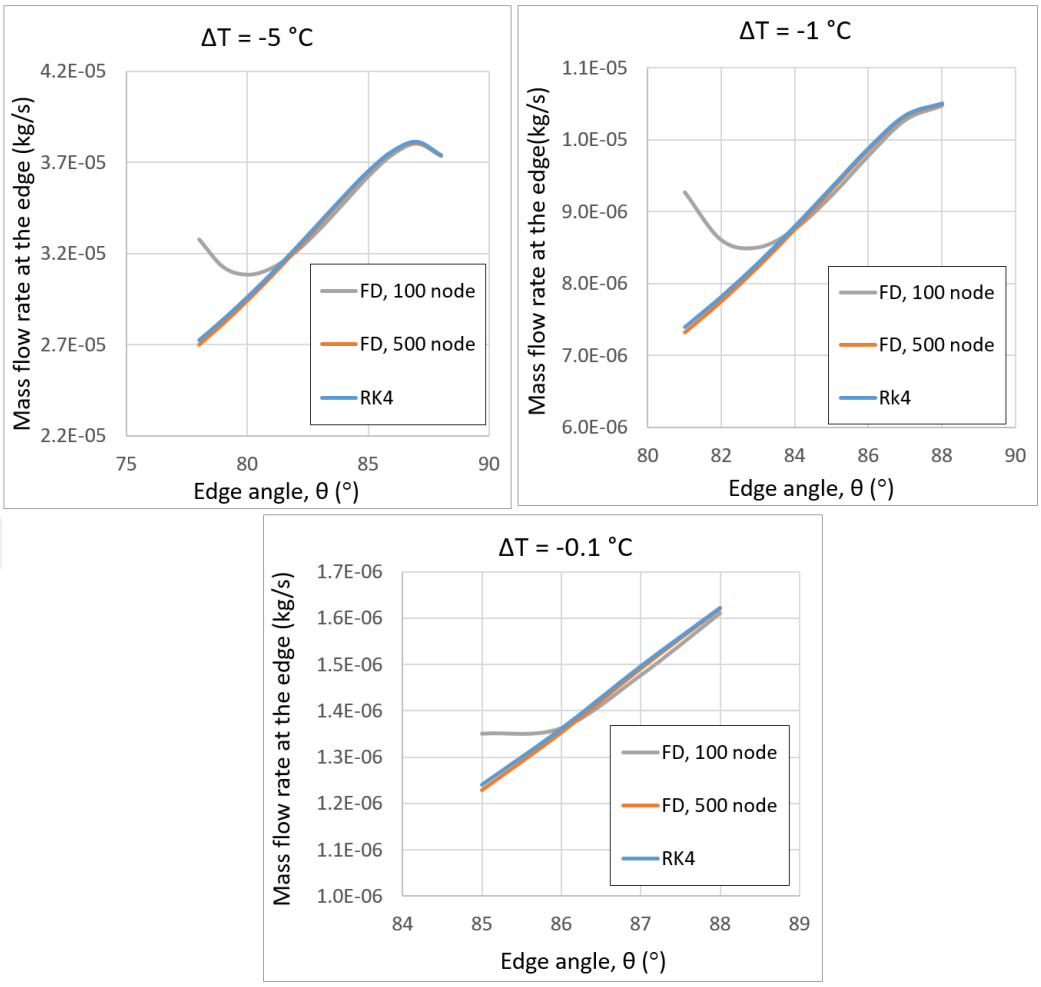


Figure 4.7: Comparison of mass flow rate at the edge along axial direction for FD method with different mesh size

## 4.4 FD formulation of the two-dimensional flow/condensation problem

In this section, first, the solution domain for the two-dimensional model is introduced, and the corresponding boundary conditions in both lateral and axial directions for the problem are defined. In the end, a novel numerical approach is presented to solve the governing two-dimensional partial differential equation given in Eq. (4.10).

### 4.4.1 Solution domain

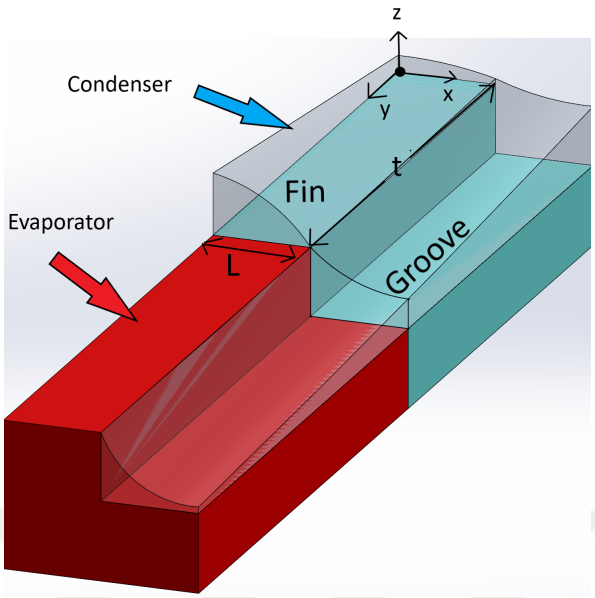


Figure 4.8: Geometry of the two-dimensional fin top flow domain

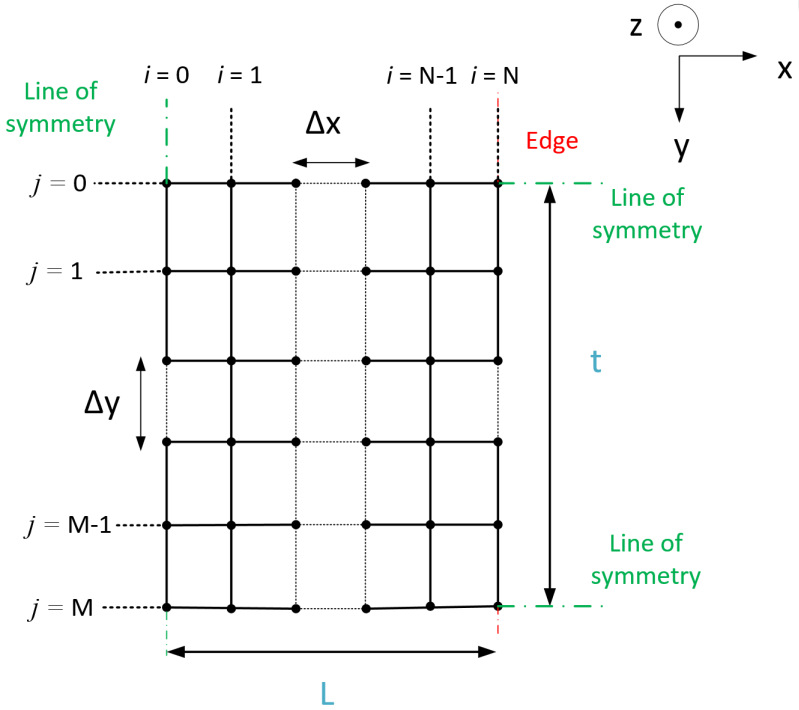


Figure 4.9: Two dimensional solution domain and the coordinate system used in the formulation

The problem domain in the lateral $(x)$ direction is in the interval of $[0, L]$, and, in the axial $(y)$ direction, it is in the interval of $[0, t]$. In lateral direction the interval is divided into $N$ equal sub-interval $(0 \leq i \leq N)$, and in the axial direction it is divided into $M$ equal sub-interval $(0 \leq j \leq M)$, which can be seen in the Fig. 4.9.

### 4.4.2 Boundary conditions

Boundary conditions in the $x$- direction are the same as the one-dimensional flow in Section 2.5.3. The first set of boundary conditions is utilized in the lateral direction for the two-dimensional model. In the $y$-directions, boundary conditions are assumed to satisfy the symmetry condition, which means that at the $y = 0$ and $y = t$ mass flow rate in the axial direction should be zero. The boundary conditions in the $y$-direction can be written as follows:

$$\begin{aligned} \text{At} \quad y = 0 \ : \qquad & \frac{\partial \delta}{\partial y} = 0 \quad \text{and} \quad \frac{\partial^3 \delta}{\partial y^3} = 0 \\ \text{At} \quad y = t \ : \qquad & \frac{\partial \delta}{\partial y} = 0 \quad \text{and} \quad \frac{\partial^3 \delta}{\partial y^3} = 0 \end{aligned} \tag{4.20}$$

where $t$ is the extent of the fluid film along the axial direction.

### 4.4.3 Numerical formulation and solution

The two-dimensional governing equation Eq. (4.10) is solved numerically using finite difference method. In the lateral direction, the same one-dimensional model formulae are used. Central difference formulae of order $\mathcal{O}(h^2)$ given below are used for the internal nodes in the axial direction.

$$\begin{aligned} \left(\delta_y\right)_{i,j} &= \frac{\delta_{i,j+1} - \delta_{i,j-1}}{2\,\Delta y} \\ \left(\delta_{yy}\right)_{i,j} &= \frac{\delta_{i,j+1} - 2\,\delta_{i,j} + \delta_{i,j-1}}{\Delta y^2} \\ \left(\delta_{yyy}\right)_{i,j} &= \frac{\delta_{i,j+2} - 2\,\delta_{i,j+1} + 2\,\delta_{i,j-1} - \delta_{i,j-2}}{2\,\Delta y^3} \\ \left(\delta_{yyyy}\right)_{i,j} &= \frac{\delta_{i,j+2} - 4\,\delta_{i,j+1} + 6\,\delta_{i,j} - 4\,\delta_{i,j-1} + \delta_{i,j-2}}{\Delta y^4} \end{aligned} \tag{4.21}$$

At the boundary nodes, by assuming ghost-cells, the symmetry conditions should be embedded in the $\delta_{yyy}$ and $\delta_{yyyy}$ formulae:

$$\begin{aligned}
&\text{At} \quad j=0 \quad ; \quad \frac{\partial \delta}{\partial y}=0 \quad \rightarrow \quad \delta_{i,-1}=\delta_{i,1} \\
&\text{At} \quad j=0 \quad ; \quad \frac{\partial^3 \delta}{\partial y^3}=0 \quad \rightarrow \quad \delta_{i,-2}=\delta_{i,2} \\
&\text{At} \quad j=M \quad ; \quad \frac{\partial \delta}{\partial y}=0 \quad \rightarrow \quad \delta_{i,M+1}=\delta_{i,M-1} \\
&\text{At} \quad j=M \quad ; \quad \frac{\partial^3 \delta}{\partial y^3}=0 \quad \rightarrow \quad \delta_{i,M+2}=\delta_{i,M-2}
\end{aligned} \tag{4.22}$$

These conditions result in the following finite difference formulae at the boundary nodes:

$$\begin{aligned}
\left(\delta_{yyy}\right)_{i,1} &= \frac{\delta_{i,3}-2\,\delta_{i,2}+2\,\delta_{i,0}-\delta_{i,1}}{2\,\Delta y^3} \\
\left(\delta_{yyy}\right)_{i,M-1} &= \frac{\delta_{i,M-1}-2\,\delta_{i,M}+2\,\delta_{i,M-2}-\delta_{i,M-3}}{2\,\Delta y^3} \\
\left(\delta_{yyyy}\right)_{i,0} &= \frac{2\,\delta_{i,2}-8\,\delta_{i,1}+6\,\delta_{i,0}}{\Delta y^4} \\
\left(\delta_{yyyy}\right)_{i,1} &= \frac{\delta_{i,3}-4\,\delta_{i,2}+7\,\delta_{i,1}-4\,\delta_{i,0}}{\Delta y^4} \\
\left(\delta_{yyyy}\right)_{i,M-1} &= \frac{-4\,\delta_{i,M}+7\,\delta_{i,M-1}-4\,\delta_{i,M-2}+\delta_{i,M-3}}{\Delta y^4} \\
\left(\delta_{yyyy}\right)_{i,M} &= \frac{2\,\delta_{i,M-2}-8\,\delta_{i,M-1}+6\,\delta_{i,M}}{\Delta y^4}
\end{aligned} \tag{4.23}$$

The two-dimensional governing equation is nonlinear, and nonlinearities must first be dealt with to implement the finite difference method. The iterative successive substitution method used for the one-dimensional test case is also applied here to linearize the equation, which is explained in Section 4.2. The linearized form of governing equation can be written as:

$$
\begin{aligned}
{}_{k+1}\delta_{xxxx} = &- {}_{k}\delta_{yyyy} - \frac{3\ {}_{k}\delta_{x}\ {}_{k}\delta_{xxx}}{{}_{k}\delta} - \frac{3\ {}_{k}\delta_{y}\ {}_{k}\delta_{yyy}}{{}_{k}\delta} \\
&- \frac{3\ {}_{k}\delta_{x}\ {}_{k}\delta_{xyy}}{{}_{k}\delta} - \frac{3\ {}_{k}\delta_{y}\ {}_{k}\delta_{yxx}}{{}_{k}\delta} \\
&- 2\ {}_{k}\delta_{xxyy} - \frac{3\,\nu}{\sigma\ {}_{k}\delta^{3}}\left[\frac{a\,(T_w - T_v) - b\,(P_c + P_d)}{1 + a\ {}_{k}\delta\,h_{lv}/k_l}\right]
\end{aligned}
\tag{4.24}
$$

To start the iterative process, the initial liquid film profile must be obtained from a one-dimensional model solved by the RK4 method for different edge angles along the $y$-direction. At first, the linearized Eq. (4.24) is solve with Gauss Elimination method for the film thickness $(\delta)$ in the interval of $(1 \leq i \leq N)$ for $j = 0$ cross-section. Then in the symmetry line, $\delta_{0,j}$ is calculated by the shooting method in conjunction with a secant root finder to satisfy Eq. (4.24). This part contains two loops, just like the one-dimensional model. This procedure is repeated for the other cross-sections $(1 \leq j \leq M)$ in the axial direction. After obtaining the film thickness values for all cross-sections in the $y$-direction, it should be a third loop to compare the initial values of $\delta$ in the $j = 0$ cross-section with the updated value. It has to be mentioned that after each loop convergence, the values of $\delta$ will be updated with proper damping in order to calculate the right-hand side of the Eq. (4.24). The right-hand side terms in the main equation are calculated numerically with the finite difference formulae. The complete numerical process algorithm for the two-dimensional model can be seen in Fig. 4.10.

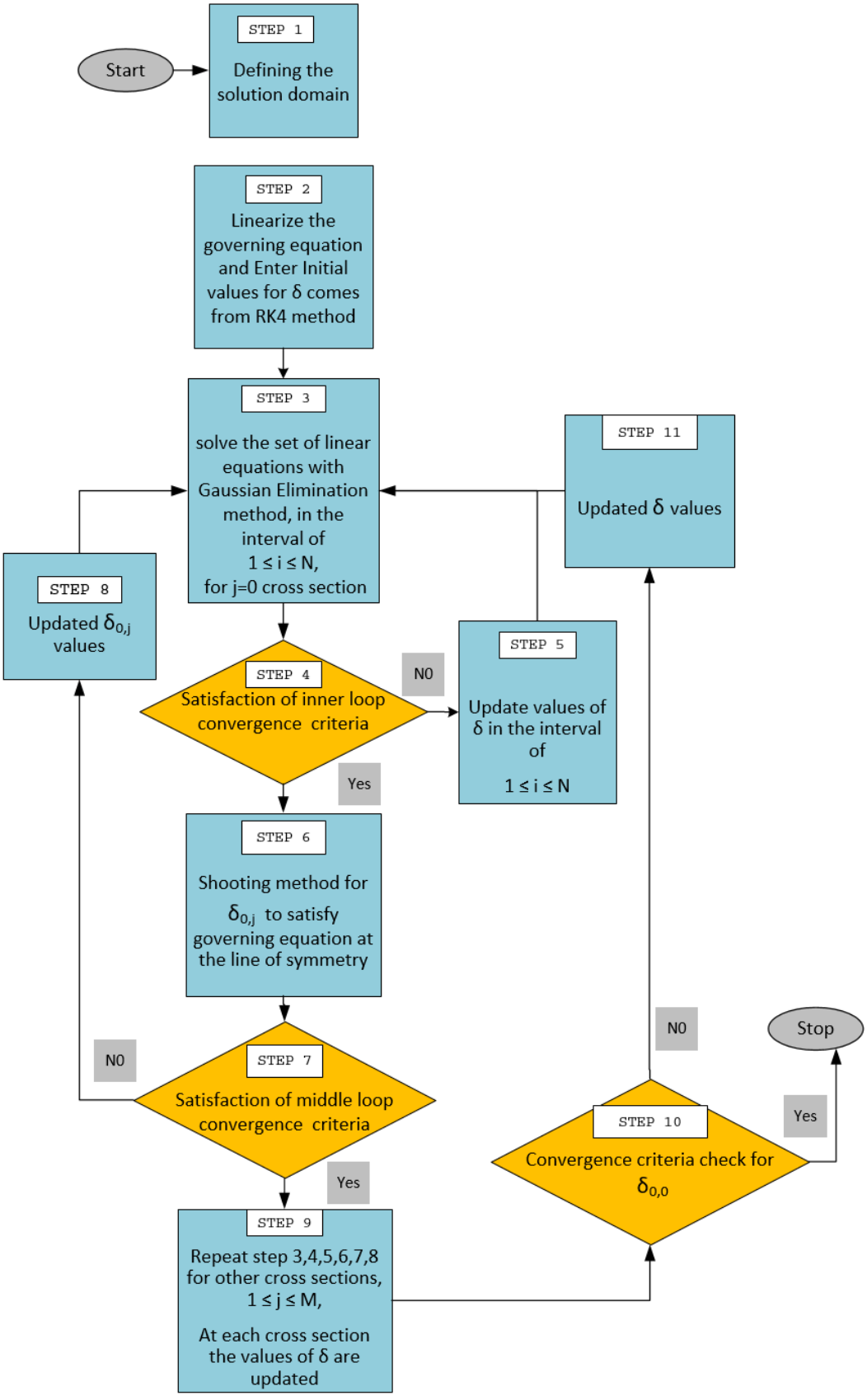


Figure 4.10: Flowchart of two-dimensional flow model

## 4.5 Preliminary findings

The preliminary numerical findings for the two-dimensional flow are presented in this section. The operating fluid is water, and the length of the fin top and the condenser are $200\ \mu m$ and $2\ cm$, respectively. The physical properties for the two-dimensional model are the same as the one-dimensional model, given in Table 3.1. The solution domain starts from $\theta = 88°$ ($y = 0$) and ends at $\theta = 83°$ ($y = t$). Also, the temperature difference between the vapor and liquid stays in a constant value of $\Delta T = -5℃$ along the solution domain. In $x$ and $y$ directions, the number of nodes are taken as $50$ and $400$, respectively. Using an the Intel(R) Core(TM) i7-7700HQ CPU @ 2.80GHz 2.81 GHz processor, the CPU time for the model with this number of nodes is approximately $22$ hours. The variation of film profile is found and plotted in Fig. 4.11. Note that Fig. 4.11 is not plotted to scale, and the condenser length ($t$) is $100$ times larger than the fin length ($L$).

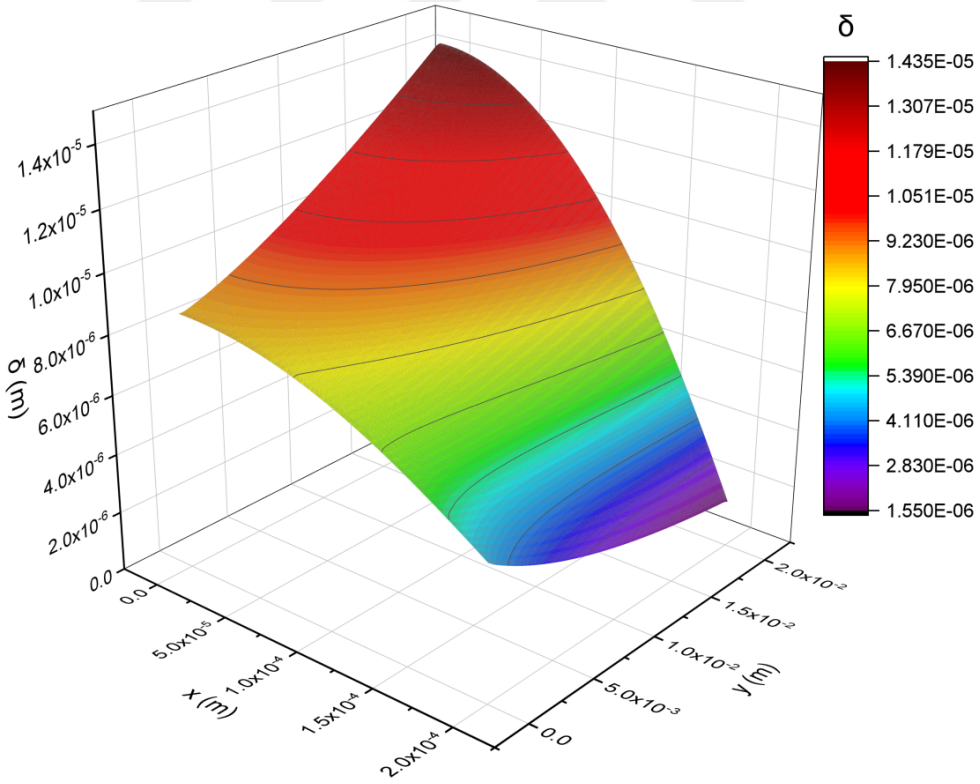


Figure 4.11: Variation of profile film between $\theta = 88°$ to $\theta = 83°$ edge angle and with a constant temperature difference of $\Delta T = -5℃$

### 4.5.1 The comparison of axial and lateral flows

The variation of the axial mass flow rate can be shown in Fig. 4.12, which demonstrates that the considerable axial flow takes place near the symmetry line ($x = 0$), and it is in the opposite direction. Moreover, the maximum axial mass flow rate occurs in the proximity of $\theta = 83°$ edge angle.

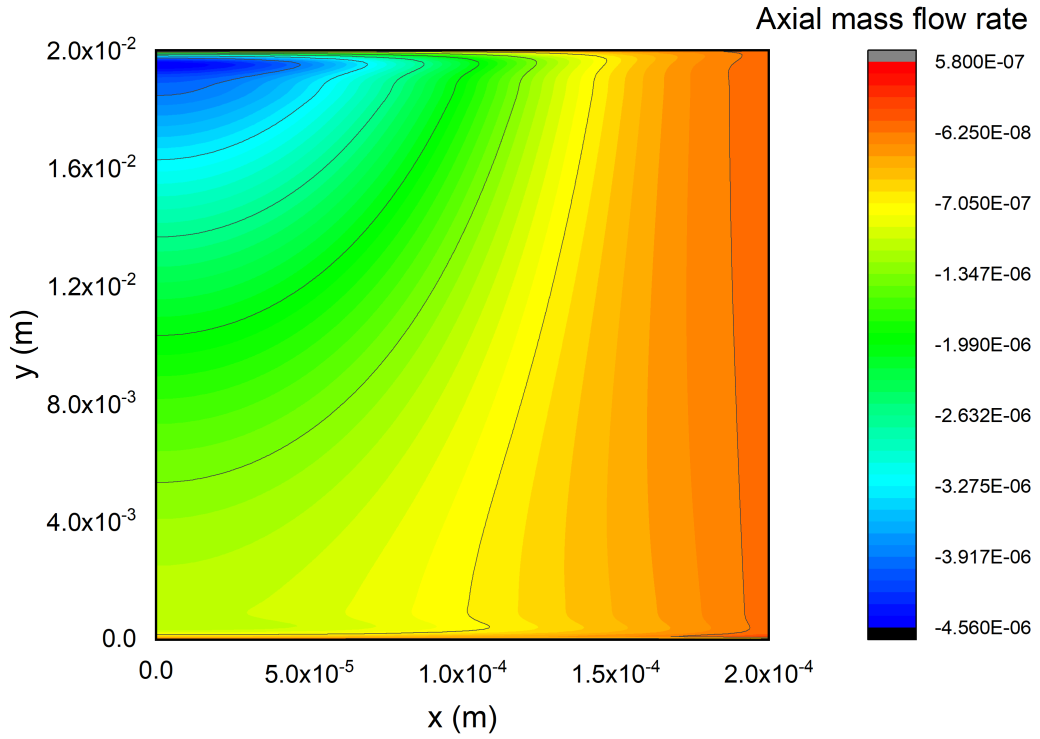


Figure 4.12: Axial mass flow rate between $\theta = 88°$ to $\theta = 83°$ edge angle and with a constant temperature difference of $\Delta T = -5℃$

The ratio of axial flow over the lateral flow is presented in Fig. 4.13. Obviously, the axial flow is negligible compared to lateral flow on the fin top except for a small zone near the symmetry line.

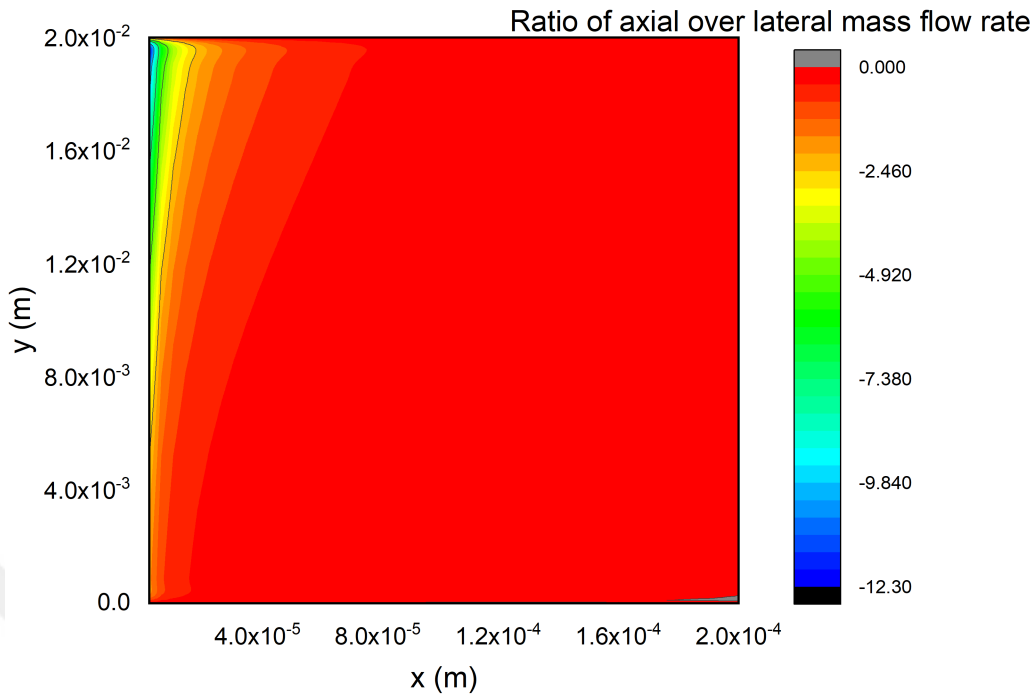


Figure 4.13: The ratio of axial mass flow rate over lateral mass flow rate for $\theta = 88°$ to $\theta = 83°$ range of edge angles and with the constant temperature difference of $\Delta T = -5°\mathrm{C}$

### 4.5.2 The effect of mesh size

The FD method allows to solve two-dimensional flow on the fin top, but it has a drawback related to its computational time. It takes excessively long computational times for a large number of nodes to solve the problem. Therefore, the mesh size in both $x$ and $y$ directions has to be chosen wisely in order to find a proper solution and minimize the CPU time. By considering the ratio of fin top length to the condenser length, it can be concluded that the number of nodes in $y$-direction should be greater than the number of nodes in $x$-direction. In the lateral direction, $50$ nodes are assumed, and for the axial direction, the problem is solved for both $100$ and $400$ nodes in order to observe the mesh size effect on the solution. After solving the problem, the first derivative of film thickness with respect to $y$ is calculated numerically at $j = 0$ and $j = M$ to ensure that the boundary condition effect is properly embedded in the so-

lution. In Fig. 4.14, it can be seen that by assuming $400$ nodes in the axial direction, the solution is more likely to satisfy the boundary conditions rather than $100$ nodes.

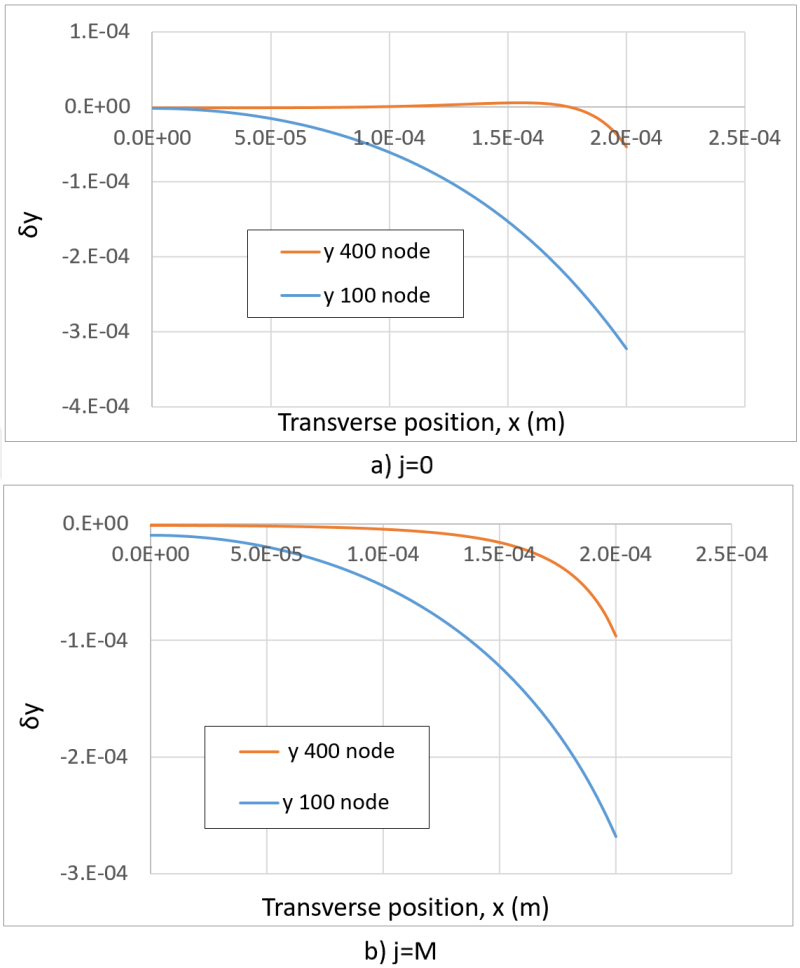


Figure 4.14: Comparison of first derivative of liquid film thickness with respect to $y$ for different number of nodes in $y$-direction along $x$ for the cross sections of a) $j = 0$ and b) $j = M$

Moreover, according to the boundary conditions in the $y$-direction, the net axial mass flow rate should be zero at the $j = 0$ and $j = M$. After finding the solution for both the number of nodes in $y$-direction, the net axial mass flow rate is numerically calculated and plotted in Fig. 4.15 for both cases. It can be understood that the number of nodes is vital in obtaining a correct solution.

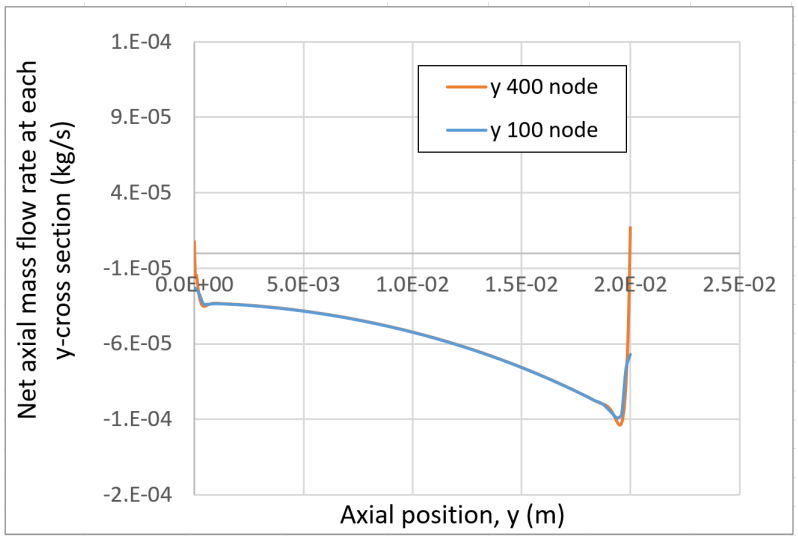


Figure 4.15: Comparison of net axial mass flow at each cross section in $y$-direction, for different number of node in $y$-direction

# CHAPTER 5

# CONCLUSION AND SUGGESTIONS FOR FUTURE WORK

## 5.1 Conclusion

A mathematical model of condensation film on the fin top of grooved heat pipe is presented in this study, and different numerical approaches are used to solve the governing $4^{th}$ order nonlinear differential equation. The effect of different sets of boundary conditions and disjoining pressure on the condensation behavior and solution domain is explored and discussed. Neglecting the disjoining pressure results in thicker film profiles and solution domain for a broader range of edge angles. However, including the effect of disjoining pressure into the governing equation renders the model more realistic and limits the solution range. This limitation is caused by the discontinuity of the third derivative of film thickness at the fin edge.

Moreover, according to the validation in Section 3.2, it can be seen that for the smaller edge angles with small temperature differences Model 1 matches reference model [39] well. However, for higher edge angles with high-temperature differences, the results of the Model 2 have a better agreement with the results of the reference model [39].

Furthermore, the results obtained in Chapter 4 reveal that Model 2 results in thinner film profile on the fin top compared to Model 1, and as a result, due to the lower thermal resistance, the condensation mass flux will be more significant for Model 2.

Finally, the preliminary findings for the two-dimensional flow model suggest that the axial mass flow rate is negligible compared to lateral flow in most regions on the fin top. However, for the small area near the line of symmetry, the axial mass flow rate is

non-negligible and even dominant compared to the lateral mass flow rate.

## 5.2 Possible future work

The current study has investigated the flow on the fin top in the condensation section. A future work can be conducted to explore the flow model in the transition region from the condenser to evaporator section on the fin top. The possible flows in the transition region are shown in Fig. 5.1

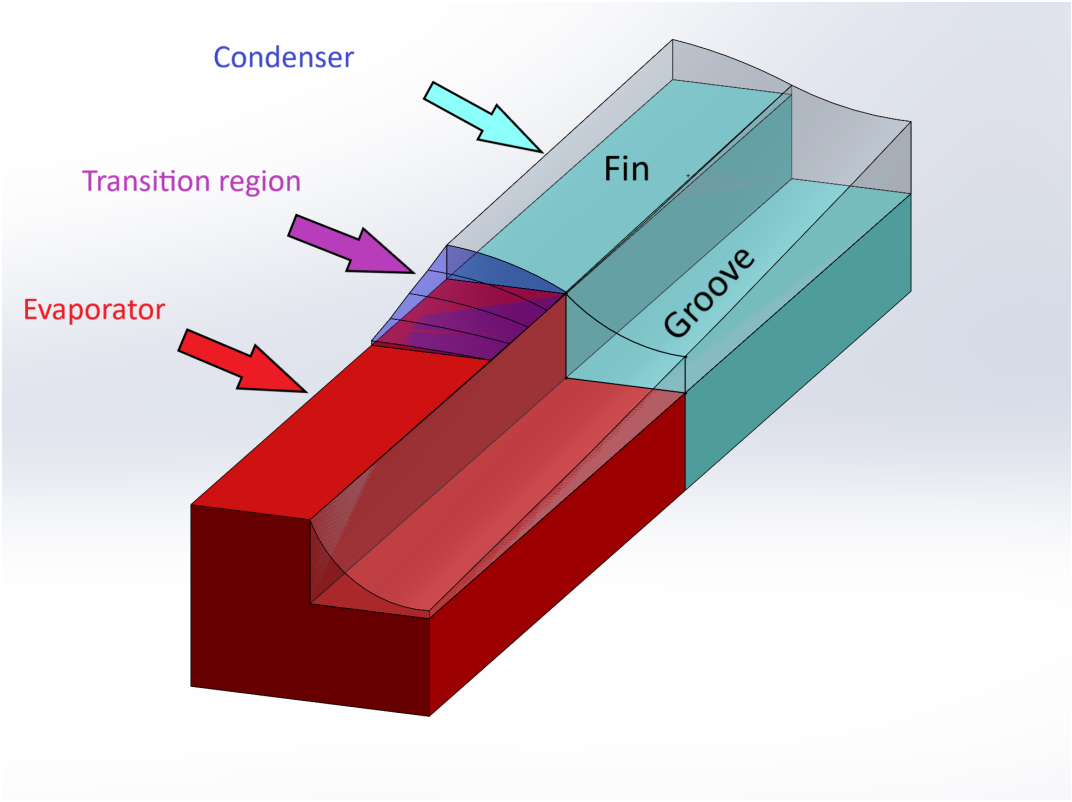


Figure 5.1: A possible flow in transition region from the condensation to evaporation section

Combining the current two-dimensional model with the transition region model helps to find a unique solution of the liquid-vapor interface shape on the fin top of the grooved heat pipe.

# REFERENCES


[1] S. Rashidi, H. Shamsabadi, J. A. Esfahani, and S. Harmand, "A review on potentials of coupling pcm storage modules to heat pipes and heat pumps," *Journal of Thermal Analysis and Calorimetry*, vol. 140, no. 4, pp. 1655–1713, 2020.

[2] R. K. Bumataria, N. Chavda, and H. Panchal, "Current research aspects in mono and hybrid nanofluid based heat pipe technologies," *Heliyon*, vol. 5, no. 5, p. e01627, 2019.

[3] A. Faghri, "Heat pipes: review, opportunities and challenges," *Frontiers in Heat Pipes (FHP)*, vol. 5, no. 1, 2014.

[4] Y. F. Maydanik, "Loop heat pipes," *Applied thermal engineering*, vol. 25, no. 5-6, pp. 635–657, 2005.

[5] M. Zaghdoudi, S. Maalej, J. Mansouri, and M. Sassi, "Flat miniature heat pipes for electronics cooling: state of the art, experimental and theoretical analysis," *International Journal of Mechanical and Mechatronics Engineering*, vol. 5, no. 3, pp. 714–737, 2011.

[6] H. Alijani, B. Çetin, Y. Akkuş, and Z. Dursunkaya, "Effect of design and operating parameters on the thermal performance of aluminum flat grooved heat pipes," *Applied Thermal Engineering*, vol. 132, pp. 174–187, 2018.

[7] G. Odabaşı, "Modeling of multidimensional heat transfer in a rectangular grooved heat pipe," 2014.

[8] M. Potash Jr and P. Wayner Jr, "Evaporation from a two-dimensional extended meniscus," *International Journal of Heat and Mass Transfer*, vol. 15, no. 10, pp. 1851–1863, 1972.

[9] S. Moosman and G. Homsy, "Evaporating menisci of wetting fluids," *Journal of Colloid and Interface Science*, vol. 73, no. 1, pp. 212–223, 1980.

[10] S. DasGupta, J. A. Schonberg, I. Y. Kim, and P. C. Wayner Jr, "Use of the augmented young-laplace equation to model equilibrium and evaporating extended menisci," *Journal of Colloid and Interface Science*, vol. 157, no. 2, pp. 332–342, 1993.

[11] P. Stephan and C. Busse, "Analysis of the heat transfer coefficient of grooved heat pipe evaporator walls," *International Journal of heat and mass transfer*, vol. 35, no. 2, pp. 383–391, 1992.

[12] A. Mirzamoghadam and I. Catton, "A physical model of the evaporating meniscus," 1988.

[13] Y. Akkuş and Z. Dursunkaya, "A new approach to thin film evaporation modeling," *International Journal of Heat and Mass Transfer*, vol. 101, pp. 742–748, 2016.

[14] F. Holm and S. Goplen, "Heat transfer in the meniscus thin-film transition region," 1979.

[15] A. Jiao, R. Riegler, H. Ma, and G. Peterson, "Thin film evaporation effect on heat transport capability in a grooved heat pipe," *Microfluidics and Nanofluidics*, vol. 1, no. 3, pp. 227–233, 2005.

[16] P. Sosnowski, A. Petronio, and V. Armenio, "Numerical model for thin liquid film with evaporation and condensation on solid surfaces in systems with conjugated heat transfer," *International Journal of Heat and Mass Transfer*, vol. 66, pp. 382–395, 2013.

[17] N. Laaroussi, G. Lauriat, and G. Desrayaud, "Effects of variable density for film evaporation on laminar mixed convection in a vertical channel," *International Journal of Heat and Mass Transfer*, vol. 52, no. 1-2, pp. 151–164, 2009.

[18] B. Xiao and A. Faghri, "A three-dimensional thermal-fluid analysis of flat heat pipes," *International Journal of Heat and Mass Transfer*, vol. 51, no. 11-12, pp. 3113–3126, 2008.

[19] R. Ranjan, J. Y. Murthy, S. V. Garimella, and U. Vadakkan, "A numerical model for transport in flat heat pipes considering wick microstructure effects," *International Journal of Heat and Mass Transfer*, vol. 54, no. 1-3, pp. 153–168, 2011.

[20] Y. Li, H.-f. He, and Z.-x. Zeng, "Evaporation and condensation heat transfer in a heat pipe with a sintered-grooved composite wick," *Applied Thermal Engineering*, vol. 50, no. 1, pp. 342–351, 2013.

[21] Y. Li, W. Zhou, J. He, Y. Yan, B. Li, and Z. Zeng, "Thermal performance of ultra-thin flattened heat pipes with composite wick structure," *Applied Thermal Engineering*, vol. 102, pp. 487–499, 2016.

[22] S. Movaghgharnezhad and J. Darabi, "Advanced micro-/nanostructured wicks for passive phase-change cooling systems," *Nanoscale and Microscale Thermophysical Engineering*, vol. 25, no. 2, pp. 116–135, 2021.

[23] S. Pandey, "Dropwise and filmwise condensation," *International Journal of Scientific  Engineering Research*, vol. Volume 3, no. Issue 4, pp. 2–6, 2012.

[24] F. P. Incropera, D. P. DeWitt, T. L. Bergman, A. S. Lavine, *et al.*, *Fundamentals of heat and mass transfer*, vol. 6. Wiley New York, 1996.

[25] B. El Fil, G. Kini, and S. Garimella, "A review of dropwise condensation: Theory, modeling, experiments, and applications," *International Journal of Heat and Mass Transfer*, vol. 160, p. 120172, 2020.

[26] A. Goswami, S. C. Pillai, and G. McGranaghan, "Surface modifications to enhance dropwise condensation," *Surfaces and Interfaces*, vol. 25, p. 101143, 2021.

[27] S. Lee, K. Cheng, V. Palmre, M. M. H. Bhuiya, K. J. Kim, B. J. Zhang, and H. Yoon, "Heat transfer measurement during dropwise condensation using micro/nano-scale porous surface," *International Journal of Heat and Mass Transfer*, vol. 65, pp. 619–626, 2013.

[28] L. Zheng, Y.-X. Wang, J. L. Plawsky, and P. C. Wayner, "Effect of curvature, contact angle, and interfacial subcooling on contact line spreading in a microdrop in dropwise condensation," *Langmuir*, vol. 18, no. 13, pp. 5170–5177, 2002.

[29] A. Faghri, Yuwen Zhang, "Numerical simulation of condensation on a capillary grooved structure," *Numerical Heat Transfer:  Part A: Applications*, vol. 39, no. 3, pp. 227–243, 2001.

[30] Y. Kamotani, "Analysis of axially grooved heat pipe condensers," in *14th Aerospace Sciences Meeting*, p. 147, 1976.

[31] K. H. Do, S. J. Kim, and S. V. Garimella, "A mathematical model for analyzing the thermal characteristics of a flat micro heat pipe with a grooved wick," *International Journal of Heat and Mass Transfer*, vol. 51, no. 19-20, pp. 4637–4650, 2008.

[32] K. H. Do and S. P. Jang, "Effect of nanofluids on the thermal performance of a flat micro heat pipe with a rectangular grooved wick," *International Journal of Heat and Mass Transfer*, vol. 53, no. 9-10, pp. 2183–2192, 2010.

[33] S. Launay, V. Sartre, and M. Lallemand, "Hydrodynamic and thermal study of a water-filled micro-heat-pipe array," *Journal of thermophysics and heat transfer*, vol. 18, no. 3, pp. 358–363, 2004.

[34] F. Lefèvre, R. Rullière, G. Pandraud, and M. Lallemand, "Prediction of the temperature field in flat plate heat pipes with micro-grooves–experimental validation," *International Journal of Heat and Mass Transfer*, vol. 51, no. 15-16, pp. 4083–4094, 2008.

[35] S. Lips, J. Bonjour, and F. Lefèvre, "Investigation of evaporation and condensation processes specific to grooved flat heat pipes," *Frontiers in heat pipes*, vol. 1, no. 2, pp. 023001–1, 2010.

[36] M. Alipour and Z. Dursunkaya, "Limitations of matching condensing film profile on a micro fin with the groove: critical effect of disjoining pressure," *Nanoscale and Microscale Thermophysical Engineering*, vol. 23, no. 4, pp. 289–303, 2019.

[37] M. Alipour, "Modeling of fluid -vapor interface in the condensation zone of a grooved heat pipe," Master's thesis, Middle East Technical University, 2017.

[38] O. Akdag, Y. Akkus, and Z. Dursunkaya, "The effect of disjoining pressure on the shape of condensing films in a fin-groove corner," *International Journal of Thermal Sciences*, vol. 142, pp. 357–365, 2019.

[39] O. Akdag. personal communication.

[40] R. Hornbeck, *Numerical Methods: With Numerous Examples and Solved Illustrative Problems*. QPI series, Quantum Publishers, 1975.

# APPENDIX A

# MODIFIED FINITE DIFFERENCE FORMULAE

## A.1 Modified finite difference formulae for the fourth derivative

In order to include the effect of boundary condition on the finite difference formulation, new formulae are derived from the Taylor series expansion.

**For $i = N$, the node at the edge of the groove:**

Taylor series expansion of $\delta_{N-1}$, $\delta_{N-2}$ and $\delta_{N-3}$ around $x = N$ can be written as follows:

$$a\left[\delta_{N-1} = \delta_N - \delta'_N\,\Delta x + \delta''_N\,\frac{\Delta x^2}{2!} - \delta'''_N\,\frac{\Delta x^3}{3!} + \delta''''_N\,\frac{\Delta x^4}{4!} - \delta^V_N\,\frac{\Delta x^5}{5!}\right] \tag{A.1}$$

$$b\left[\delta_{N-2} = \delta_N - \delta'_N\,2\Delta x + \delta''_N\,\frac{4\Delta x^2}{2!} - \delta'''_N\,\frac{8\Delta x^3}{3!} + \delta''''_N\,\frac{16\Delta x^4}{4!} - \delta^V_N\,\frac{32\Delta x^5}{5!}\right] \tag{A.2}$$

$$c\left[\delta_{N-3} = \delta_N - \delta'_N\,3\Delta x + \delta''_N\,\frac{9\Delta x^2}{2!} - \delta'''_N\,\frac{27\Delta x^3}{3!} + \delta''''_N\,\frac{81\Delta x^4}{4!} - \delta^V_N\,\frac{243\Delta x^5}{5!}\right] \tag{A.3}$$

Since the effect of $\delta'_N$ and $\delta''_N$ should be implemented in the formula, the sum of coefficients of the $\delta'''$ and $\delta^V$ should be zero. This restriction gives:

$$-a - 8b - 27c = 0 \tag{A.4a}$$

$$-a - 32b - 243c = 0 \tag{A.4b}$$

Because there are three unknowns and two equations, for solving the above system, the value of $a$ can be arbitrarily set, and then the values of $b$ and $c$ can be calculated:

$$\text{Assuming } a = 45 \longrightarrow b = -9 \text{ and } \mathrm{c} = 1 \tag{A.5}$$

After substituting Eq. (A.5) in Eq. (A.1), Eq. (A.2) and Eq. (A.3) and summing up, the following finite difference formula is obtained:

$$\delta'''' _N = \frac{148\,\delta_N - 180\,\delta_{N-1} + 36\,\delta_{N-2} - 4\,\delta_{N-3} - 120\,\delta'_N\,\Delta x + 36\,\delta''_N\,\Delta x^2}{3\,\Delta x^4} \tag{A.6}$$

**For $i = N - 1$, the first node before the groove's edge:**

Taylor series expansion of $\delta_N$, $\delta_{N-2}$, $\delta_{N-3}$ and $\delta_{N-4}$ around $x = N-1$ can be written as follows:

$$\begin{aligned}\delta_N = \delta_{N-1} + \underbrace{\delta'_{N-1}}_{*}\,\Delta x + \underbrace{\delta''_{N-1}}_{*}\,\frac{\Delta x^2}{2!} + \delta'''_{N-1}\,\frac{\Delta x^3}{3!} + \delta''''_{N-1}\,\frac{\Delta x^4}{4!} \\ + \delta^{V}_{N-1}\,\frac{\Delta x^5}{5!} + \delta^{VI}_{N-1}\,\frac{\Delta x^6}{6!}\end{aligned} \tag{A.7}$$

$$\begin{aligned}\delta_{N-2} = \delta_{N-1} - \underbrace{\delta'_{N-1}}_{*}\,\Delta x + \underbrace{\delta''_{N-1}}_{*}\,\frac{\Delta x^2}{2!} - \delta'''_{N-1}\,\frac{\Delta x^3}{3!} + \delta''''_{N-1}\,\frac{\Delta x^4}{4!} \\ - \delta^{V}_{N-1}\,\frac{\Delta x^5}{5!} + \delta^{VI}_{N-1}\,\frac{\Delta x^6}{6!}\end{aligned} \tag{A.8}$$

$$\begin{aligned}\delta_{N-3} = \delta_{N-1} - \underbrace{\delta'_{N-1}}_{*}\,2\Delta x + \underbrace{\delta''_{N-1}}_{*}\,\frac{4\Delta x^2}{2!} - \delta'''_{N-1}\,\frac{8\Delta x^3}{3!} + \delta''''_{N-1}\,\frac{16\Delta x^4}{4!} \\ - \delta^{V}_{N-1}\,\frac{32\Delta x^5}{5!} + \delta^{VI}_{N-1}\,\frac{64\Delta x^6}{6!}\end{aligned} \tag{A.9}$$

$$\begin{aligned}\delta_{N-4} = \delta_{N-1} - \underbrace{\delta'_{N-1}}_{*}\,3\Delta x + \underbrace{\delta''_{N-1}}_{*}\,\frac{9\Delta x^2}{2!} - \delta'''_{N-1}\,\frac{27\Delta x^3}{3!} + \delta''''_{N-1}\,\frac{81\Delta x^4}{4!} \\ - \delta^{V}_{N-1}\,\frac{243\Delta x^5}{5!} + \delta^{VI}_{N-1}\,\frac{729\Delta x^6}{6!}\end{aligned} \tag{A.10}$$

Since the effect of boundary conditions should be included in the formulae, the (*'s) could be written as a function of $\delta'_N$ and $\delta''_N$, the conditions gives at the groove's edge.

Taylor series expansion of $\delta''_N$ around $x = N-1$:

$$\delta''_N = \delta''_{N-1} + \delta'''_{N-1}\,\Delta x + \delta''''_{N-1}\,\frac{\Delta x^2}{2!} + \delta^V_{N-1}\frac{\Delta x^3}{3!} + \delta^{VI}_{N-1}\,\frac{\Delta x^4}{4!} \tag{A.11}$$

Therefore, $\delta''_{N-1}$ can be written as a function of $\delta''_N$ as follows:

$$\delta''_{N-1} = \delta''_N - \delta'''_{N-1}\,\Delta x - \delta''''_{N-1}\,\frac{\Delta x^2}{2!} - \delta^V_{N-1} - \delta^{VI}_{N-1}\,\frac{\Delta x^4}{4!} \tag{A.12}$$

The same approach is used for $\delta'_{N-1}$. Taylor series expansion of $\delta'_N$ around $x = N-1$:

$$\delta'_N = \delta'_{N-1} + \underbrace{\delta''_{N-1}}_{*}\,\Delta x + \delta'''_{N-1}\,\frac{\Delta x^2}{2!} + \delta''''_{N-1}\,\frac{\Delta x^3}{3!} + \delta^V_{N-1}\,\frac{\Delta x^4}{4!} + \delta^{VI}_{N-1}\,\frac{\Delta x^5}{5!} \tag{A.13}$$

Therefore, by substituting Eq. (A.12) in (*), $\delta'_{N-1}$ can be written as a function of $\delta'_N$ and $\delta''_N$, the conditions gives at the groove's edge:

$$\delta'_{N-1} = \delta'_N - \delta''_N\,\Delta x + \delta'''_{N-1}\,\frac{\Delta x^2}{2} - \delta''''_{N-1}\,\frac{\Delta x^3}{3} - \delta^V_{N-1}\,\frac{\Delta x^4}{8} - \delta^{VI}_{N-1}\,\frac{\Delta x^5}{30} \tag{A.14}$$

After substituting Eq. (A.14) and Eq. (A.12) in (*'s) of Eq. (A.7), Eq. (A.8), Eq. (A.9) and Eq. (A.10), Taylor series expansion of $\delta_N$, $\delta_{N-2}$, $\delta_{N-3}$ and $\delta_{N-4}$ around $x = N-1$ can be written in form, which includes the effect of boundary conditions:

$$a\left[\delta_N = \delta_{N-1} + \delta'_N\,\Delta x - \delta''_N\,\frac{\Delta x^2}{2} + \delta'''_{N-1}\,\frac{\Delta x^3}{6} + \delta''''_{N-1}\,\frac{\Delta x^4}{8} + \delta^V_{N-1}\,\frac{\Delta x^5}{20} + \delta^{VI}_{N-1}\,\frac{\Delta x^6}{72}\right] \tag{A.15}$$

$$b\Bigg[\delta_{N-2} = \delta_{N-1} - \delta'_N\,\Delta x + \delta''_N\,\frac{3\Delta x^2}{2} - \delta'''_{N-1}\,\frac{7\Delta x^3}{6} - \delta''''_{N-1}\,\frac{13\Delta x^4}{24} - \delta^V_{N-1}\,\frac{13\Delta x^5}{60} - \delta^{VI}_{N-1}\,\frac{19\Delta x^6}{360}\Bigg] \tag{A.16}$$

$$c\Bigg[\delta_{N-3} = \delta_{N-1} - \delta'_N\,2\Delta x + \delta''_N\,4\Delta x^2 - \delta'''_{N-1}\,\frac{13\Delta x^3}{3} - \delta''''_{N-1}\,\Delta x^4 - \delta^V_{N-1}\,\frac{17\Delta x^5}{20} - \delta^{VI}_{N-1}\,\frac{11\Delta x^6}{180}\Bigg] \tag{A.17}$$

$$d\Bigg[\delta_{N-4} = \delta_{N-1} - \delta'_N\,3\Delta x + \delta''_N\,\frac{15\Delta x^2}{2} - \delta'''_{N-1}\,\frac{21\Delta x^3}{2} + \delta''''_{N-1}\,\frac{\Delta x^4}{8} - \delta^V_{N-1}\,\frac{63\Delta x^5}{20} + \delta^{VI}_{N-1}\,\frac{29\Delta x^6}{40}\Bigg] \tag{A.18}$$

$\delta'_N$ and $\delta''_N$ should be implemented in the formula; hence, the sum of coefficients of the $\delta'''$, $\delta^V$ and $\delta^{VI}$ should be zero. This restriction gives:

$$\begin{aligned} \frac{a}{6} - \frac{7b}{6} - \frac{13c}{3} - \frac{21d}{2} &= 0 \\ \frac{a}{20} - \frac{13b}{60} - \frac{17c}{20} - \frac{63d}{20} &= 0 \\ \frac{a}{72} - \frac{19b}{360} - \frac{11c}{180} + \frac{29d}{40} &= 0 \end{aligned} \tag{A.19}$$

Because there are four unknowns and three equations, for solving the above system, the value of $a$ can be arbitrarily set, and then the values of $b$, $c$ and $d$ can be calculated:

$$\text{Assuming } a = 113 \longrightarrow b = 108\ ,\ c = -32 \text{ and } d = 3 \tag{A.20}$$

After substituting Eq. (A.20) in Eq. (A.15), Eq. (A.16), Eq. (A.17) and Eq. (A.18) and summing up, the following finite difference formula is obtained:

$$\delta''''_{N-1} = \frac{-113\,\delta_N + 192\,\delta_{N-1} - 108\,\delta_{N-2} + 32\,\delta_{N-3} - 4\,\delta_{N-4} + 60\,\delta'_N\,\Delta x}{12\,\Delta x^4} \tag{A.21}$$

## A.2 Modified finite difference formulae for the third derivative

**For $i = N$, the node at the edge of the groove:**

Taylor series expansion of $\delta_{N-1}$, $\delta_{N-2}$ and $\delta_{N-3}$ around $x = N$ can be written as follows:

$$a\left[\delta_{N-1} = \delta_N - \delta'_N\,\Delta x + \delta''_N\,\frac{\Delta x^2}{2!} - \delta'''_N\,\frac{\Delta x^3}{3!} + \delta''''_N\,\frac{\Delta x^4}{4!}\right] \tag{A.22}$$

$$b\left[\delta_{N-2} = \delta_N - \delta'_N\,2\Delta x + \delta''_N\,\frac{4\Delta x^2}{2!} - \delta'''_N\,\frac{8\Delta x^3}{3!} + \delta''''_N\,\frac{16\Delta x^4}{4!}\right] \tag{A.23}$$

Since the effect of $\delta'_N$ and $\delta''_N$ should be implemented in the formula, the sum of coefficients of the $\delta''''$ should be zero. This restriction gives:

$$\frac{a}{24} + \frac{16b}{24} = 0 \tag{A.24}$$

Because there are two unknowns and one equation, for solving the above equation, the value of $a$ can be arbitrarily set, and then the value of $b$ can be calculated:

$$\text{Assuming } a = 16 \longrightarrow b = -1 \tag{A.25}$$

After substituting Eq. (A.25) in Eq. (A.22) and Eq. (A.23) and summing up, the following finite difference formula is obtained:

$$\delta'''_N = \frac{45\,\delta_N - 48\,\delta_{N-1} + 3\,\delta_{N-2} - 42\,\delta'_N\,\Delta x + 18\,\delta''_N\,\Delta x^2}{4\,\Delta x^3} \tag{A.26}$$

**For $i = N - 1$, the first node before the groove's edge:**

Taylor series expansion of $\delta_N$ and $\delta_{N-2}$ around $x = N - 1$ can be written as follows:

$$\delta_N = \delta_{N-1} + \underbrace{\delta'_{N-1}}_{*} \Delta x + \underbrace{\delta''_{N-1}}_{*} \frac{\Delta x^2}{2!} + \delta'''_{N-1} \frac{\Delta x^3}{3!} + \delta''''_{N-1} \frac{\Delta x^4}{4!} \tag{A.27}$$

$$\delta_{N-2} = \delta_{N-1} - \underbrace{\delta'_{N-1}}_{*} \Delta x + \underbrace{\delta''_{N-1}}_{*} \frac{\Delta x^2}{2!} - \delta'''_{N-1} \frac{\Delta x^3}{3!} + \delta''''_{N-1} \frac{\Delta x^4}{4!} \tag{A.28}$$

Since the effect of boundary conditions should be included in the formulae, the (*'s) could be written as a function of $\delta'_N$ and $\delta''_N$, the conditions gives at the groove's edge.

Taylor series expansion of $\delta''_N$ around $x = N - 1$:

$$\delta''_N = \delta''_{N-1} + \delta'''_{N-1} \Delta x + \delta''''_{N-1} \frac{\Delta x^2}{2!} \tag{A.29}$$

Therefore, $\delta''_{N-1}$ can be written as a function of $\delta''_N$ as follows:

$$\delta''_{N-1} = \delta''_N - \delta'''_{N-1} \Delta x - \delta''''_{N-1} \frac{\Delta x^2}{2!} \tag{A.30}$$

The same approach is used for $\delta'_{N-1}$. Taylor series expansion of $\delta'_N$ around $x = N-1$:

$$\delta'_N = \delta'_{N-1} + \underbrace{\delta''_{N-1}}_{*} \Delta x + \delta'''_{N-1} \frac{\Delta x^2}{2!} + \delta''''_{N-1} \frac{\Delta x^3}{3!} \tag{A.31}$$

Therefore, by substituting Eq. (A.30) in (*), $\delta'_{N-1}$ can be written as a function of $\delta'_N$ and $\delta''_N$, the conditions gives at the groove's edge.

$$\delta'_{N-1} = \delta'_N - \delta''_N \Delta x + \delta'''_{N-1} \frac{\Delta x^2}{2} - \delta''''_{N-1} \frac{\Delta x^3}{3} \tag{A.32}$$

After substituting Eq. (A.30) and Eq. (A.32) in (*'s) of Eq. (A.27) and Eq. (A.28), Taylor series expansion of $\delta_N$ and $\delta_{N-2}$ around $x = N - 1$ can be written in form, which includes the effect of boundary conditions:

$$a\left[\delta_N = \delta_{N-1} + \delta'_N\,\Delta x - \delta''_N\,\frac{\Delta x^2}{2} + \delta'''_{N-1}\,\frac{\Delta x^3}{6} + \delta''''_{N-1}\,\frac{\Delta x^4}{8}\right] \tag{A.33}$$

$$b\left[\delta_{N-2} = \delta_{N-1} - \delta'_N\,\Delta x + \delta''_N\,\frac{3\Delta x^2}{2} - \delta'''_{N-1}\,\frac{7\Delta x^3}{6} - \delta''''_{N-1}\,\frac{13\Delta x^4}{24}\right] \tag{A.34}$$

$\delta'_N$ and $\delta''_N$ should be implemented in the formula; hence, the sum of coefficients of the $\delta''''$ should be zero. This restriction gives:

$$\frac{a}{8} - \frac{13b}{24} = 0 \tag{A.35}$$

Because there are two unknowns and one equation, for solving the above equation, the value of $a$ can be arbitrarily set, and then the value of $b$ can be calculated:

$$\text{Assuming } a = 13 \longrightarrow b = 3 \tag{A.36}$$

After substituting Eq. (A.36) in Eq. (A.33) and Eq. (A.34) and summing up, the following finite difference formula is obtained:

$$\delta'''_{N-1} = \frac{-39\,\delta_N + 48\,\delta_{N-1} - 9\delta_{N-2} + 30\,\delta'_N\,\Delta x - 6\,\delta''_N\,\Delta x^2}{4\,\Delta x^3} \tag{A.37}$$